



**THE EFFECTS OF TEMPERATURE AND ELECTRON RADIATION ON THE
ELECTRICAL PROPERTIES OF AlGaN/GaN HETEROSTRUCTURE FIELD
EFFECT TRANSISTORS**

THESIS

Jeffrey T. Moran, Major, USA

AFIT/GNE/ENP/09-M04

**DEPARTMENT OF THE AIR FORCE
AIR UNIVERSITY**
AIR FORCE INSTITUTE OF TECHNOLOGY

Wright-Patterson Air Force Base, Ohio

APPROVED FOR PUBLIC RELEASE; DISTRIBUTION UNLIMITED

The views expressed in this thesis are those of the author and do not reflect the official policy or position of the United States Air Force, United States Army, Department of Defense, or the United States Government.

THE EFFECTS OF TEMPERATURE AND ELECTRON RADIATION ON THE
ELECTRICAL PROPERTIES OF AlGaN/GaN HETEROSTRUCTURE FIELD
EFFECT TRANSISTORS

THESIS

Presented to the Faculty
Department of Engineering Physics
Graduate School of Engineering and Management
Air Force Institute of Technology
Air University
Air Education and Training Command
In Partial Fulfillment of the Requirements for the
Degree of Master of Science in Nuclear Engineering

Jeffrey T. Moran, BS

Major, USA

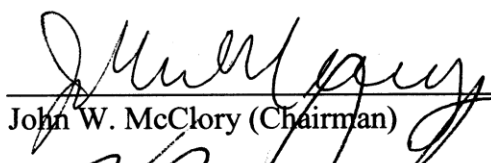
March 2009

APPROVED FOR PUBLIC RELEASE; DISTRIBUTION UNLIMITED

THE EFFECTS OF TEMPERATURE AND ELECTRON RADIATION ON THE
ELECTRICAL PROPERTIES OF AlGaN/GaN HETEROSTRUCTURE FIELD
EFFECT TRANSISTORS

Jeffrey T. Moran, BS
Major, USA

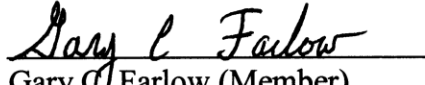
Approved:


John W. McClory (Chairman)

13 MAR 09
Date


James C. Petrosky (Member)

13 MAR 09
Date


Gary C. Farlow (Member)

12 March 09
Date

Abstract

$\text{Al}_x\text{Ga}_{1-x}\text{N}/\text{GaN}$ Heterostructure Field Effect Transistors (HFETs) have come under increased study, in recent years, owing to their highly desirable material and electrical properties, ruggedness, and survivability even during and after exposure to extreme temperature and radiation environments. These devices or similar devices constructed of AlGaN and/or GaN materials are being researched for their potential applications in many military and space-based systems.

In this study, unpassivated and Si_3N_4 -passivated $\text{Al}_{0.27}\text{Ga}_{0.73}\text{N}/\text{GaN}$ HFETs were subjected to electron radiation at incident energies of 0.5 MeV or 1.0 MeV and fluences from 5×10^{14} to 5×10^{15} [e-/cm²] while maintained in a 10^{-6} Torr or lower vacuum at liquid nitrogen temperature (LNT). Primary focus was on the effects of electron irradiation and temperature on drain current, gate leakage current, threshold voltage shifts, and gate-channel capacitance. Measurements were taken of transistor current and gate-channel capacitance at LNT and room temperature (RT) and gate leakage current vs. gate bias at 4 K temperature intervals beginning at LNT through RT. The resulting gate leakage currents were fitted to a Trap-Assisted Tunneling model and transistor currents were compared to a Charge Control model to evaluate post-irradiation change mechanisms affecting the HFET gate and drain currents respectively.

All HFETs tested survived the irradiations, temperature extremes, and numerous measurements while maintaining transistor operation, albeit with the following post-irradiation changes noted. Post-irradiation drain currents increased for all devices, with a

consistently lower percentage increase observed for passivated devices. Most post-irradiation increases returned to nearly pre-irradiation levels after a RT anneal. Threshold voltage shifts averaged -0.5 V for unpassivated and -0.2 V for passivated HFETs, showed negligible temperature dependence, and returned to almost to pre-irradiation values after RT anneal periods. Gate-channel capacitance levels showed little post-irradiation change and negligible temperature dependence. However, a negative whole-curve shift along the x-axis (gate bias) closely matched the threshold voltage shift in each device. Gate leakage currents showed higher pre-irradiation levels in passivated devices as well as a positive temperature dependency and post-irradiation increases for all devices. Post-irradiation gate leakage current increases approached normal levels after RT anneal periods for unpassivated HFETs and showed little recovery in passivated HFETs.

Fitting experimental data to the trap-assisted tunneling model indicated the dominant mechanism supporting the post-irradiation increase in gate leakage current was increased trap density for unpassivated devices and increased donor concentration for passivated devices. Post-irradiation changes in carrier concentration, obtained from observed drain current increases and calculated with the charge control model using observed threshold voltage shifts, were attributed to trapped, positive charges in the AlGaN layer. These trapped, positive charges resulted from electron-hole pairs created by electron radiation-induced ionizations.

Acknowledgements

To those who came before (and I referenced) I humbly salute you!

To the guys in the AFIT machine and fabrication shop; Jan, Jason, and Danny, goes a hearty “Job well done!” for turning basically a napkin drawing into an awesome stainless-steel cold-head with high-tech electrical pass-throughs.

To Mr. Larry Callahan of the AFRL SNDD, many thanks for the rapid turn-around packaging of the HFETs used in this study. Your assistance was invaluable.

To Mr. Eric Taylor, who made my research gadgetry and daily automation operations a success, I truly appreciate all your assistance.

To Dr. James Petrosky and Dr. Gary C. Farlow, thank you for the academic background that made this research successful. Additionally, Dr. Farlow’s tireless efforts kept the Wright State Van de Graaf generator operating during my research.

To my advisor, LTC John McClory, no words can adequately express my appreciation for the support and guidance you provided throughout my AFIT experience, especially during this research effort. Your inexhaustible patience, extensive knowledge of the subject matter, and complete lack of arrogance or selfishness with which you dispense that knowledge has been invaluable to me.

To my family, you all are the most important part of my life. I promise to make up for the long hours I spent away from you during my studies at AFIT (just as soon as I get back from ILE!). I love you all and look forward to many evenings, weekends, and vacations doing family stuff together.

Table of Contents

	Page
Abstract	iv
Acknowledgements	vi
Table of Contents	vii
List of Figures	ix
List of Tables	xiii
List of Abbreviations	xiv
I. Introduction	1
Problem Statement.....	6
Background.....	7
Thesis Organization.....	9
II. Previous Research/Current Technology.....	11
AFIT AlGaN/GaN HFET Research	11
Other Research into Radiation Effects on AlGaN, GaN, and HFETs	14
III. Theory and Modeling.....	19
Al _x Ga _{1-x} N/GaN Device Physics	19
Theory of Radiation Effects	22
Effects of Si ₃ N ₄ Passivation on AlGaN/GaN HFETs.....	30
Modeling.....	31
Trap Assisted Tunneling (TAT) Model.....	31
Transistor Current Model	34
IV. Experimental Procedures	37
AlGaN HFET Production, Preparation, and Pre-Characterization.....	37
Pre-Irradiation Characterization	43
Experimental Apparatus	49
Data Collection	53
Electrical Measurements Taken	56
Temperature Control and Monitoring During Data Collection	58
V. Experimental Results and Discussion	61
Transistor Drain Current (I _{ds} vs. V _{ds}) and Transistor Current Model Results	61
Results for I _{ds} vs. V _{gs} Measurements	68
Comparison of Carrier Concentration Change Indicators	70

	Page
Results for C_{gs} vs. V_{gs} Measurements	73
Results for I_{gs} vs. V_{gs} at Varying Temperatures	78
Results for Trap Assisted Tunneling (TAT) Model	81
Comparison of Electron and Neutron Radiation Effects	87
VI. Conclusions and Recommendations	93
Conclusions	93
Recommended Future Efforts in AlGaN/GaN Research.....	97
Bibliography	99

List of Figures

Figure	Page
1. Comparison of carrier concentration of GaN to that of other popular semiconductor materials [4].....	4
2. Layer view of AlGaN/AlN/GaN HEMTs studied by Hu, et al, using 1.8 MeV proton radiation [16].....	17
3. Comparison of TOP and SIDE Views of $\text{Al}_x\text{Ga}_{1-x}\text{N}/\text{GaN}$ HFET, along with Energy Band Diagram Showing Quantum Well and 2DEG Channel [10].....	21
4. XGEN plot of collisional vs. radiative stopping power in AlGaN and GaN material, taken from Sattler[4].	27
5. XGEN plot of electron range vs. electron energy in AlGaN and GaN materials, taken from Sattler[4].	28
6. TIGER code graph showing expected dose deposited vs. depth in the HFET's gate region by a total fluence of $1 \times 10^{14} \text{ e-}/\text{cm}^2$ at 0.45 MeV energy, taken from Sattler [4].	28
7. TIGER code graph showing expected dose deposited vs. depth in the HFET's gate region by a total fluence of $1 \times 10^{14} \text{ e-}/\text{cm}^2$ at 1.2 MeV energy, taken from Sattler [4].	29
8. Composition side view of AlGaN/GaN HFETs used [5].....	38
9. FatFET layout, as constructed on the reticle, showing package leads connected to Shottky gate contact and ohmic drain and source contacts. The FatFET is the HFET actually used in this research [4].....	39
10. Packaged Reticle with FatFET highlighted. Note: Only the 3 upper right leads, of the 10 installed leads are used.....	40
11. (Upper Left) Packaged HFETs positioned on Cold-Finger. (Lower Right) ZIF-switch test block with packaged reticle for initial device operational check.	41
12. HFET thermal break-in I_{gs} vs. T curves (Left) and average values of these curves plotted with one SD error bars (Right) [5].	42

Figure	Page
13. Plot of pre-irradiation averaged drain to source currents for eight unpassivated and four passivated HFETs tested at LNT and RT at $V_{gs} = -2$ V	44
14. Highlighting linear region in I_{ds} vs. V_{gs} curves for U01.....	46
15. Linear extrapolation method applied to linear regions of four unpassivated HFET curves. Temperature made little difference in V_{th} . Passivation added an average -0.6 V to unpassivated V_{th} values of -4 V to -4.3 V. The R^2 values for the isolated portions shown in this figure are better than 0.999.....	46
16. Comparisons of averaged pre-irradiation gate capacitance vs. gate voltage for unpassivated and passivated HFETs at both LNT and RT. Arrows indicate approximate threshold voltage values.	47
17. Plot of averaged pre-irradiation gate leakage current vs. temperature at $V_{gs} = -4$ V and showing one sigma error bars. The highest gate leakage current value is 0.33mA for the unpassivated, and roughly half that, at 0.15mA for the passivated HFETs.....	48
18. Switching Control Test Box. Shown with cold-head leads, two SMUs, and CVA connected.	49
19. HFET Device Switching Control Test Box (SCTB) wiring schematic.	50
20. Cold-Head (pre-welding), showing the sample stage's hollow chamber, the flanged electrical pass-throughs, and the LN supply/return pipes.....	52
21. HFET devices mounted on cold-head sample stage. Shown are the electrical connectors and the pass-thru vacuum side wiring harness.....	55
22. Test and measurement equipment setups: (Left) Wright State VDG lab and (Right) AFIT bldg 470 lab.	56
23. Liquid Nitrogen cooling system for Van de Graff operations.	59
24. Large Dewar in Bldg 470 lab with cold-finger suspended inside. Connectivity for HFETs and RTD is shown.....	60
25. Pre- and Post-Irradiation curves for U01, after 0.5 MeV electron fluence of 5×10^{14} e-/cm ² , at LNT before any RT anneal periods.	62

Figure	Page
26. Pre- and Post-Irradiation curves for U03, after a 1.0 MeV electron fluence of 5×10^{14} e-/cm ² , at LNT before any RT anneal periods.	63
27. Average drain current values at $V_{gs} = -2$ V; pre-irradiation, post-irradiation, and post RT anneal showing LNT curves in (a) and RT curves in (b) with the average of the unpassivated HFETs on the left and passivated HFETs on the right.	64
28. Plot of pre- and post-irradiation data for passivated HFET P01, after a 0.5 MeV electron fluence of 5×10^{14} e-/cm ² , at LNT before any RT anneal periods.	65
29. Drain current vs. drain voltage at LNT and $V_{gs} = -2$ V for U10; irradiated to 1×10^{15} e-/cm ² @ 0.5 MeV.	66
30. Drain current vs. drain-to-source voltage at RT and $V_{gs} = -2$ V for U10; irradiated to 1×10^{15} e-/cm ² @ 0.5 MeV.	67
31. Plot of drain current vs. gate voltage, for U01, highlighting the linear extrapolation method for determining the post-irradiation threshold voltage shift [40]. Note, the complete recovery post 48-day RT anneal.	69
32. Plot of drain current vs. gate voltage, for passivated HFET P01, highlighting the linear extrapolation method for determining the post-irradiation threshold voltage shift. Note, the slight super recovery post 48-day RT anneal.	70
33. Gate capacitance vs. gate voltage curves for unpassivated HFET at LNT. The post-irradiation V_{th} shift (arrow #2) and the slight super-recovery (arrow #3) toward pre-irradiation values (arrow #1) are clearly visible. Curves are vertically normalized for comparison.	74
34. C_{gs} vs. V_{gs} at LNT, for passivated device P04. Note the negligible post-irradiation shift in V_{th} . Curves are vertically normalized for comparison.	75
35. The effects of interface trap formation is seen in the slope-flattening from LNT to RT on the post-irradiation capacitance curves for (a) an unpassivated HFET and (b) a passivated HFET.	76
36. Gate leakage current vs. gate voltage for unpassivated device U01 at 100 K and 212K. Note the higher values at higher temperature.	78

Figure	Page
37. Gate leakage current vs. temperature at $V_{gs} = -4$ V, for an unpassivated HFET.....	79
38. Gate leakage current vs. temperature curves for a passivated HFET at $V_{gs} = -4$ V. Passivated devices showed little recovery after RT anneal.	80
39. Averaged gate leakage current curves for unpassivated (left) and passivated (right) HFETs. Post RT anneal recovery is apparent for the unpassivated devices while passivated HFETs show no tendency to recover after RT anneal.....	80
40. Pre-irradiation, TAT model fit to unpassivated HFET. Using the R-RMSE compared to averaged I_{gs} data resulted in $\pm 2.24\%$ error for fit.....	83
41. Post-irradiation TAT Model fit to unpassivated HFET. Using the R-RMSE compared to averaged I_{gs} data resulted in $\pm 2.24\%$ error for fit.....	84
42. Pre-irradiation TAT model fit to passivated HFET. The typically higher gate leakage current levels for passivated devices is apparent, as well as the 7.77% R-RMSE to averaged current comparison. Error bars on left plot appear larger due to scale of the gate leakage current axis.....	84
43. Post-irradiation TAT model fit to passivated HFET.....	85
44. Pre- and post-irradiation (1×10^{15} e-/cm ² @ 0.5 MeV) curves for U10. Note the relatively close fit of the TAT model as indicated by the low percent errors.	86
45. Chart from [12] showing non-ionizing energy loss (NIEL) [keV-cm ⁻² -g ⁻¹] vs. energy in MeV for various types of radiation. Horizontal, right-pointing arrow (red) highlights equivalence of 1 MeV neutrons to 1 MeV electrons (~ 1:170).....	88
46. Ionizing energy loss and fluence-to-dose conversion factors in silicon for various radiations from [12].....	90

List of Tables

Table	Page
1. Properties of Competing Materials in Power Electronics [1].....	1
2. Desirable properties of advanced semiconductor devices [1].....	2
3. Material properties of GaN [32].	5
4. Table of some previous research into effects of particle irradiation of AlGaN/GaN HFETs. Protons, ions, gammas, and neutrons are listed. Most relevant research involving electrons has been done at AFIT [6].	15
5. Max Energy Transferred to Ga and N lattice atoms for specified electron energies.	25
6. Results from repetitive measurements to determine percent error in observed changes in electrical properties of HFETs in this study.	43
7. SCTB Toggle Switch positions for each of the 4 measurements taken; same at LNT or RT.	51
8. SCTB 3-way rotary switch positions for each of the 4 measurements taken; same at LNT or RT.	51
9. Inventory of devices, fluences, electron energies, and measurements taken.	54
10. Results of calculating carrier concentration changes by drain current model using threshold voltage shift and by I_{ds} changes pre- to post-irradiation.	71
11. Qualitative summary of interface trap concentrations.	77
12. Results for Trap Assisted Tunneling Model. Upper section is Pre- and Post-Irradiation values and the lower section is the absolute and percent changes.	82
13. Results from each HFET irradiation cycle. Values are percent change from original pre-irradiation values. In the third column, the ' I_{gs} vs. Temp @ V_{gs} ' percent changes were determined from the $V_{gs} = -4$ V curves by comparing the gate current values at the $T = 200$ K for each curve.	87

List of Abbreviations

<u>Abbreviation</u>	<u>Description</u>
2DEG	Two-Dimensional Electron Gas
AFRL	Air Force Research Laboratory
AlGaN	Aluminum Gallium Nitride alloy
Al _x Ga _{1-x} N	Same as above, except highlights Al molar fraction (x) in material
AlGaN /GaN	Aluminum Gallium Nitride/Gallium Nitride layering
CVA	Capacitance Voltage Analyzer (Keithley Model 590)
CI	Confidence Interval (statistical terminology)
FET	Field Effect Transistor
GPIB	National Instruments/Hewlett-Packard General Purpose Interface Bus
HFET	Heterostructure Field Effect Transistor
IEL	Ionizing Energy Loss (i.e. electron-hole pair production)
LED	Light Emitting Diode
LN	Liquid Nitrogen
LNT	Liquid Nitrogen Temperature (~85 K)
MCNP	Monte Carlo Neutral Particle Transport Code
MeV	Mega Electron Volt [10^6 eV]
MOSFET	Metal Oxide Semiconductor Field Effect Transistor
NIEL	Non Ionizing Energy Loss (i.e. defects, interstitials, vacancies)
P01	First Passivated HFET Irradiated

P04	Fourth Passivated HFET Irradiated
RT	Room Temperature (~300 K)
SC	Semiconductor
SCTB	Switching and Control Test Box
SMU	High Voltage Source Measurement Unit (Keithley Model 237)
SNDD	Sensors Directorate Aerospace Components and Subsystems Technology Electron Devices Branch
TAT or (T.A.T.)	Trap-Assisted Tunneling
U01	First Unpassivated HFET Irradiated
U05	Fifth Unpassivated HFET Irradiated
ZIF	Zero Insertion Force

THE EFFECTS OF TEMPERATURE AND ELECTRON RADIATION ON THE ELECTRICAL PROPERTIES OF AlGaN/GaN HETEROSTRUCTURE FIELD EFFECT TRANSISTORS

I. Introduction

There exists an ever-increasing need for semiconductor (SC) devices that can withstand extremes of temperature, power, frequency, and radiation. Currently, the most common SC materials in use are silicon (Si) and gallium arsenide (GaAs). The demand for gallium nitride (GaN)-based devices, with their superior operation in extreme conditions, is expected to increase as capabilities become available [1]. Table 1 and Table 2 provide ample justification for increased utilization of GaN devices.

Table 1. Properties of Competing Materials in Power Electronics [1].

Material	μ [cm ² /V-s]	ϵ [ϵ_s / ϵ_0]	E_g [eV]	T_{max} [°K]
Si	1300	11.4	1.1	573
GaAs	5000	13.1	1.4	573
SiC	260	9.7	2.9	873
GaN	1500	9.5	3.4	973

GaN and its alloys with indium nitride (InN) and aluminum nitride (AlN) are currently the focus of much semiconductor research. GaN alloyed materials have moved

to the forefront of modern semiconductor device technology owing to their ability to emit and detect yellow, green, blue, and ultraviolet light [25]. Additionally, wide band-gap semiconductors such as GaN are gaining importance in the field of power electronics applications from power conditioning to microwave transmitters for communications and radar in order to meet the operational requirements of the Department of Defense (DOD), the Department of Homeland Security (DHS), and the civilian technology sector. Many military and national security applications as well as all space applications require operation in harsh environments. Specifically, sensors and satellite electronics are needed that can withstand radiation and temperature extremes while maintaining reliable operation for many years.

Table 2. Desirable properties of advanced semiconductor devices [1].

Need	Enabling Feature	Performance Advantage
High Power/Unit Width	Wide Bandgap, High Field	Compact, Ease of Matching
High Voltage Operation	High Breakdown Field	Eliminate/Reduce Step Down
High Linearity	HEMT Topology	Optimum Band Allocation
High Frequency	High Electron Velocity	Bandwidth, μ -Wave/mm-Wave
High Efficiency	High Operating Voltage	Power Saving, Reduced Cooling
Low Noise	High Gain, High Velocity	High Dynamic Range Receivers
High Temperature Operation	Wide Bandgap	Rugged, Reliable, Reduced Cooling
Thermal Management	SiC Substrate	High Power Densities with Reduced Cooling Needs
Technology Leverage	Direct Bandgap Allows for Lighting	Driving Force for Technology; Low Cost

The wide (3.4 eV), direct band-gap of GaN allows for photoemission and photo-absorption which occur at shorter wavelengths (near ultraviolet spectrum) than in other

common SC materials due to the size of the band-gap [26]. The large band-gap minimizes the unwanted effects of optical or thermal charge carrier generation, which can result from large temperature variations as well as specific types of radiation exposures. In addition, the strong chemical bonds between the gallium and nitrogen (and aluminum and nitrogen) atoms widen the forbidden gap in the electronic density of states, and contribute other favorable mechanical, thermal, and chemical properties [27].

$\text{Al}_x\text{Ga}_{1-x}\text{N}/\text{GaN}$ heterostructure field effect transistors (HFETs) are promising examples of the materials and devices under evaluation [1]. The properties of various materials, relevant to high power, high frequency, and high temperature applications, are shown in Table 1 [1]. GaN exceeds the capabilities of the other materials in all categories, except by comparison to GaAs with respect to carrier mobility. Despite this, the high temperature performance and large band-gap of GaN materials outweigh the higher mobility of GaAs. The large band-gap enables GaN devices to operate at higher temperatures, without changes in performance characteristics owing to the elevation of electrons from the valence band to the conduction band by thermal energy (phonons). Furthermore, GaN has a higher thermal conductivity than silicon and GaAs, which enables more rapid heat transfer to the device substrate and out via a heat sink.

Gallium nitride (GaN) based materials have characteristics making them better suited for many defense and security applications, when compared to competing materials. The technology behind GaN-based materials and devices has been refined and expanded over the last several years and, despite greater production costs than silicon and gallium arsenide, has come to the forefront in terms of research and development efforts. Table 2 provides an overview of the semiconductor industry's desired properties in

materials and devices and briefly states the advantages of GaN-based materials in meeting these requirements.

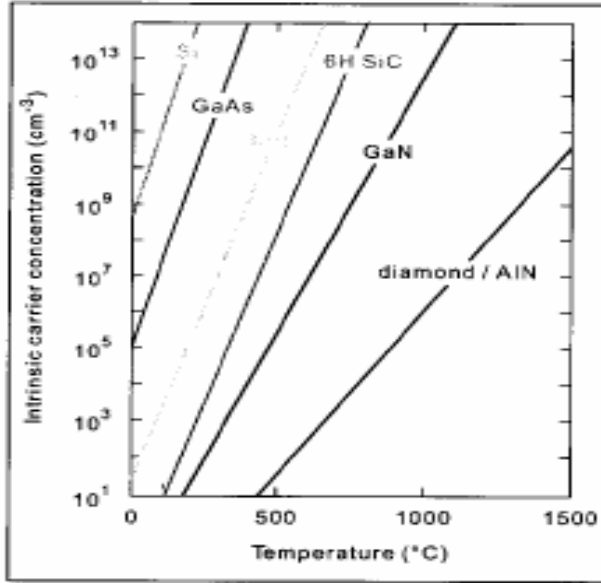


Figure 1. Comparison of carrier concentration of GaN to that of other popular semiconductor materials [4].

Another characteristic making GaN-based devices more attractive than their more commonly found competitors (Si and GaAs) is its lower intrinsic carrier concentrations at high temperatures resulting in a larger temperature range of operation or wider extrinsic region. Figure 1 compares the temperature dependence of carrier concentrations of GaN to other popular semiconductors. It highlights the lower intrinsic carrier concentration vs. temperature for GaN compared to other SC materials. Table 3 highlights material properties of GaN.

Table 3. Material properties of GaN [32].

Property (units)	Symbol	Value
Molecular Weight (g/mol)	W	83.728
Density (g/cm ³)	ρ	6.15
Thermal Conductivity (W/cm·K)	κ	1.3
Specific Heat (cal/mol·K)	C_p	$9.1 + (2.15 \cdot 10^{-3} T)$
Static Dielectric Constant	ϵ_p	9.0
High Frequency Dielectric Constant	ϵ_∞	5.35
Electron Mobility, Bulk (cm ² /V·sec)	μ_e	1000
Hole Mobility, Bulk (cm ² /V·sec)	μ_h	300
Debye Length @ 300K, $N_d=10^{18}$ cm ⁻³ (nm)	λ_D	3.586
Index of Refraction @ 1μm	n	2.35
Electron Affinity (eV)	χ	4.1

One important intended use for GaN devices is in the circuitry comprising satellite-based electronic systems. These systems are required to operate at temperature extremes from just above 3 K due to the microwave background radiation on the dark side of the moon or earth to 600 to 700 K in direct sun-lit areas of its orbit. Additionally, satellites may be subjected to relatively high fluence levels of electrons, protons, alpha particles, and heavy ions as they operate in the near earth radiation environment. A detailed description of the near-Earth radiation environment is available in the introduction section of Sattler [4], in Adams et al [12], and from MIL-STD-1809 [34].

Additionally, some SC device applications requiring long operational lifetimes and durability, without necessarily having to withstand great extremes in temperature, frequency, and radiation, are being filled with GaN-based devices. One such application is in the field of light emitting diodes (LEDs). Until recently, LEDs were limited in usefulness by their inability to produce intense light as well as their limited range of wavelengths or colors. However, newer, GaN-based LEDs are emitting wavelengths and intensities that were previously unattainable. These new GaN-based blue and green LEDs

exhibit intensity levels and long operational lifetimes that meet and exceed the requirements for many outdoor applications [25]. Now, full color spectrum, all SC LED displays are being produced in which previously available red LEDs are combined with new blue and green LEDs. When these new GaN-based LEDs are used in place of incandescent light bulbs, they consume 80-90% less power and provide lifetimes over 10 times longer than incandescent light bulbs. In fact, there is a federal energy-saving initiative to have cities in the United States replace their old, inefficient, incandescent traffic lights with LED systems [25].

Bottom line; with the multitude of potential applications related to national defense and conservation of natural resources, it is imperative that meaningful research into understanding and improving GaN-based SC device technology be undertaken. The potential military applications in space-based systems alone justified this research.

Problem Statement

The effects of electron radiation and temperature on the electrical properties of these AlGaN/GaN HFETs (described in chapter 4) are addressed in this study. The basic knowledge gaps or areas of interest, outlined below, summarize the questions posed to this study:

- 1) What are the effects of electron irradiation at energies of 500 keV and 1.0 MeV, fluence magnitudes of 10^{14} to 10^{16} [e-/cm⁻²], and temperatures in the liquid nitrogen (LN) through room temperature (RT) range, on:
 - a) Gate leakage currents
 - b) Source to drain currents

- c) Threshold voltage shifts
- d) Gate to channel capacitance

2) To what mechanisms can the electron radiation induced effects on the previously listed HFET electrical properties be attributed?

3) Can the Trap-Assisted Tunneling (TAT) model be used to identify the source of electron radiation induced changes to gate leakage currents in AlGaN/GaN HFETs?

4) Are post-irradiation, electrical effects temperature-dependent?

5) Can the material and device damage resulting from electron radiation be correlated to that damage caused by 1 MeV (eq) reactor spectrum neutrons?

Background

This research was suggested [5] as follow-on to previous studies of the effects of electron and neutron radiations on AlGaN /GaN HFETs. The concept was to conduct a more comprehensive series of electron irradiations and measurements over the temperature range 80 to 300 K and compare the results with previous electron and neutron irradiation research. Irradiating to fluences comparable to those found in the near-Earth space environment [34], especially in geosynchronous orbits, using 0.5 MeV or 1.0 MeV electrons may provide a comparison of the experimental results with results in [5], and reinforce experimental results obtained by Sattler [4] and Jarzen [13]. Variations in fluence levels could be used to establish minimum electron fluences that result in the onset of device degradation or failure. Higher fluence levels might provide insight as to the maximum electron irradiation the devices can withstand at low temperature without catastrophic or permanent failure. Finally, a greater understanding

of radiation effects on AlGaN devices could lead to better techniques for hardening devices and to improvements in material growth techniques, device construction geometries, and to the enhancement of desirable device characteristics [5].

This research adds to the results of Sattler [4], Jarzen [13], Gray [10], and McClory [5]. Sattler and Jarzen explored the low (LNT) temperature I-V and C-V response of electron-irradiated AlGaN/GaN HFETs. Gray explored the temperature and voltage dependence of the gate leakage current in AlGaN/GaN HFETs exposed to 1 MeV (eq) reactor neutron fluxes. McClory studied the temperature dependence of drain current, gate leakage current, capacitance, and conductance of reactor neutron irradiated AlGaN/GaN HFETs.

Further, Gray and McClory also employed a physics-based model to assist in analysis of the radiation induced changes to gate leakage and drain-to-source currents. Analysis using the model led to increased understanding of the electron-irradiation-induced mechanisms in both the devices and their constituent materials. Beyond providing a basis for comparison with previous research, this research reinforces the existing body of knowledge pertaining to AlGaN/GaN HFETs and furthers the understanding of radiation degradation caused by low energy electrons.

The primary means for studying the effects of low energy electron radiation on AlGaN/GaN HFETs used in this study, is the drain-to-source current (I_{ds}) and the gate-to-source/drain leakage current (I_{gs}). I_{ds} vs. gate bias voltage (V_{gs}) measurements were also used to provide an indication of the threshold voltage (V_{th}) shift post-irradiation. Additionally, gate-to-source/drain capacitance, (C_{gs}) (capacitance across the AlGaN layer separating the gate contact and the source-drain contacts), was measured and analyzed for

electron irradiation induced changes. The irradiations were performed in a vacuum at LNT with measurements taken at LNT and at predetermined temperature increments from LNT to RT and after varying lengths of post-irradiation RT anneal periods.

Thesis Organization

Chapter 1, Introduction, contains background data on AlGaN/GaN HFETs. It highlights the many applications for these types of devices in industry, defense, and space. In addition, in this section, the motivation behind this research, the expectations and objectives guiding it, and justification for doing it are discussed.

Chapter 2, Previous Research/Current Technology, details the literature review that was undertaken prior to and during the project. The importance of AlGaN/GaN heterostructures as a growing field of study is further described. Additionally, this section gives an overview of previous research efforts at AFIT and elsewhere, in which these or similar devices were subjected to irradiation with various types of radiation and the results studied and published.

Chapter 3, Theory and Modeling, discusses the physics behind the behavior and operation of these AlGaN/GaN heterostructures. Additionally, the theoretical aspects of radiation and passivation on these devices are addressed here. Further, two models are discussed that were used in analyzing the radiation-induced changes in device operation. These models, the Trap Assisted Tunneling (TAT) model and the Transistor Current model, were crucial in correlating the measured post-irradiation changes in device characteristics with physical mechanisms in the HFET layers.

Chapter 4, Experimental Procedures, details the actual steps and processes involved in the irradiation and measurement of the HFETs in this study. This includes the descriptions of the test equipment fabrication, HFET device preparation, pre-irradiation processes, and post irradiation activities necessary to provide the data and results contained in Chapter 5. Numerous photos, illustrations, and tables are included to support the descriptions.

Chapter 5, Experimental Results and Discussion, contains the collected data, descriptions of the radiation-induced changes, and results of analysis of the changes and behaviors observed. In this section, results from each of the four primary electrical measurements are shown and explained. Results and analysis from the application of the two models are included. Averages and/or representative behaviors from multiple irradiation and measurement cycles are the focus in this section. An attempt is made to explain the mechanisms at play in the devices pre- and post-irradiation and after RT annealing periods of various lengths of time. Finally, comparisons are made between the results of this research and those from other researchers.

Chapter 6, Conclusions and Recommendations, contains a short summary of the results from this research and the author's own suggestions and thoughts. Also contained in this section can be found the author's vision of follow-on research that may expand and support his own findings or clear up unanswered questions relating to this project. Following this section is the Bibliography.

II. Previous Research/Current Technology

This literature review includes previous and on-going research into radiation effects on AlGaN/GaN HFET devices and materials. Of particular interest, are the research results from recent AFIT efforts that analyzed the results of electron and neutron irradiation of HFETs. From this literature review, it was determined that:

- Further research into AlGaN/GaN HFETs is justified by still incomplete understanding of both the effect of radiation and the mechanisms involved.
- This research is not a replication of previous research.

AFIT AlGaN/GaN HFET Research

In 2004, Sattler [4] conducted research into the effects of 0.45 –1.2 MeV electron irradiations on AlGaN/GaN HFETs at LNT and using fluences up to 6×10^{16} e-/cm². During this research, it was discovered that electron radiation induced increased gate and drain currents. Also, it was observed that these increased currents were only maintained at low temperatures (well below room temperature or 300 K). The research attributed the increase in gate leakage current to an increase in the electron trap concentration in the AlGaN layer. This increase in trap concentration directly increased the trap-assisted tunneling current resulting in the observed increase in gate current. The mechanism(s) causing the increase in drain current was (were) not determined, however, several theories explaining this increase were presented as potential, future research projects. Sattler's research was the first experiment conducted at AFIT involving electron radiation of AlGaN/GaN devices [4].

Following Sattler, in 2005, Jarzen [13], irradiated AlGaN/GaN HEMTs at low temperature (around 80 K) with 0.45 to 0.8 MeV electrons and fluences of up to 1×10^{15} e-/cm² [13]. LNT capacitance-voltage (C-V) measurements produced fluence dependent changes. Post-irradiation, LNT C-V measurements were taken at intervals up to 72 hours post-irradiation at RT in order to investigate RT annealing effects on the devices. The researcher found that the C-V measurements indicated lower energy (0.45 MeV) electron irradiation resulted in an increase in the carrier concentration of the two dimensional electron gas (2DEG). He also observed that higher (0.8 MeV) electron energies resulted in a decrease in the carrier concentration of the 2DEG. Jarzen attributed the increase in drain current, observed by Sattler, to an increase in the carrier concentration in the 2DEG, as indicated by his C-V measurements. The increase in carrier concentration was explained as donor electrons from a nitrogen vacancy in the GaN layer at lower electron radiation energies, while the decrease in carrier concentration was explained as gallium vacancies acting as acceptors after higher energy electron radiation. In this research the devices failed to anneal immediately and showed incomplete recovery after a RT anneal [13].

In 2007, Gray[10] investigated gate leakage current (I_{gate}) of $\text{Al}_{0.27}\text{Ga}_{0.73}\text{N}/\text{GaN}$ HFETs. He used I-V and current-temperature (I-T) measurements after high energy (>0.5 MeV: Cd shielded) neutron irradiation at fluences between 4×10^{10} and 1.2×10^{12} n/cm² through a temperature range from LNT to RT. Gray noted an increase in gate leakage current with fluence. Further, he attributed the leakage current increase to trap assisted tunneling (TAT), and a close fit was achieved between experimental data and a thermionic trap assisted tunneling (TTT) model. A change in I-V characteristics,

interpreted as an increase in magnitude of threshold voltage, was also observed. Further, matching data with the TTT model led the researcher to surmise that increased trap density was responsible for increased I_{gate} at a fluence of $1.2 \times 10^{12} \text{ n/cm}^2$. However, this research did not yield sufficient results to conclude that either an increase in trap densities or an increase in donor defect densities was responsible for the increased I_{gate} after neutron irradiation [10].

In 2008, McClory [5] conducted testing of the AlGaN/GaN devices of interest in which the AlGaN/GaN HFETs were irradiated at low temperature and radiation-induced, temperature-dependent changes to drain current, gate current, capacitance, and gate conductance were measured. Results were evaluated with various models in order to determine the source of the radiation-induced changes in these properties. The HFETs studied in this research continued to function as transistors after 0.45 MeV electron irradiation, at fluences of up to $10^{14} \text{ electrons/cm}^2$ and $10^{14} \text{ neutrons/cm}^2$ of 1.0 MeV (eq) neutrons.

The research showed that AlGaN/GaN HFETs were susceptible to threshold voltage (V_{th}) shifts and changes to drain currents after irradiation. After electron and neutron irradiation at LNT and prior to warming to RT, drain currents (I_{ds}) increased up to a saturation level while the threshold voltage (V_{th}) increased after fluences of $10^{13} \text{ electrons/cm}^2$ or $10^{10} \text{ neutrons/cm}^2$. These post-irradiation changes were attributed to positive charges in the AlGaN layer which annealed via neutralization after warming to room temperature. Additionally, room temperature measurements after low-temperature irradiation indicated a decrease in drain-to-source current (I_{ds}). This was attributed to positive charges causing the low-temperature increase and becoming more mobile as the

temperature increases resulting in charged defects along the AlGaN/GaN heterojunction. These charged defects reduced the electron mobility in the 2DEG thereby reducing the current. The researcher further noted that these defects did not anneal at room temperature.

McClory further observed that AlGaN/GaN HFET gate leakage currents (I_{gs}) increased after LNT irradiations. Similar to I_{ds} , this elevated I_{gs} reached saturation as electron and neutron irradiation levels exceeded 10^{13} e-/cm² or 10^{10} neutrons/cm². This behavior was not observed at neutron fluences below 10^{10} n/cm². The increase in I_{gs} observed at temperatures from LNT to RT persisted after RT annealing and was attributed to Trap Assisted Tunneling (TAT). This saturation, after relatively low levels of irradiation, appeared to indicate that charged defects along the AlGaN/GaN heterojunction were formed when gallium, nitrogen, and/or aluminum combined with an impurity element in the AlGaN material. The relatively low level at which this impurity is present in the AlGaN appeared to limit the growth of additional defects. Based on material fabrication processes, oxygen was determined to be the most likely impurity contributing to this behavior. Fitting experimental data with the TAT model indicated that the increased I_{gs} was due to an increase in trap density (N_t) post irradiation [5]. A comparison of the neutron irradiation results from [5] with results using 0.5 to 1.0 MeV electrons in this research, provide insight as to the cause of various observed effects.

Other Research into Radiation Effects on AlGaN, GaN, and HFETs

Most of the previous research involving radiation effects on AlGaN/GaN devices, outside of AFIT, was conducted with protons or neutrons, with some ion irradiation and

the occasional gamma study. The following passages cite a few of the more recent publications documenting AlGaN/GaN heterostructure research by non-AFIT researchers up through the spring of 2008. Table 4 provides a quick overview of previous research into radiation effects on AlGaN/GaN HFETs or HEMTs.

Table 4. Table of some previous research into effects of particle irradiation of AlGaN/GaN HFETs. Protons, ions, gammas, and neutrons are listed. Most relevant research involving electrons has been done at AFIT [6].

RELEVANT RESULTS IN RADIATION EFFECTS ON AlGaN/GaN HFETS					
Reference	Radiation Type/ Temperature	Measurement/ Temperature	Observed Change After Irradiation	Fluence Level at Onset of Change	
White, <i>et al.</i> , 2002[14]	1.8 MeV protons @ RT	I_{ds} @ RT	Decrease	$1 \times 10^{11} p^+/\text{cm}^2$	
Luo, <i>et al.</i> , 2002[15]	40 MeV protons @ RT	I_{ds} @ RT	Decrease	$5 \times 10^9 p^+/\text{cm}^2$	
Hu, <i>et al.</i> , 2003[16]	1.8 MeV protons @ RT	I_{ds} @ RT	Decrease	$1 \times 10^{14} p^+/\text{cm}^2$	
White, <i>et al.</i> , 2003[17]	1.8 MeV protons @ RT	I_{ds} @ RT	Decrease	$1 \times 10^{13} p^+/\text{cm}^2$	
	Rev. and Fwd.		Decrease then increase	$1 \times 10^{12} p^+/\text{cm}^2$	
		I_{gs} @ RT			
Karmarkar, <i>et al.</i> , 2004[18]	1.8 MeV protons @ RT	I_{ds} @ RT	Decrease	$1 \times 10^{13} p^+/\text{cm}^2$	
		Forward I_{gs} @ RT	Decrease	$1 \times 10^{12} p^+/\text{cm}^2$	
Hu, <i>et al.</i> , 2004[19]	105 MeV protons @ RT	I_{ds} @ RT	Decrease	$1 \times 10^{13} p^+/\text{cm}^2$	
		Forward I_{gs} @ RT	No Change	Up to $1 \times 10^{13} p^+/\text{cm}^2$	
		Reverse I_{gs} @ RT	Decrease	$3 \times 10^{11} p^+/\text{cm}^2$	
	40-, 15 MeV protons @ RT	I_{ds} @ RT	No Change	Up to $1 \times 10^{11} p^+/\text{cm}^2$	
	1.8 MeV protons @ RT	I_{ds} @ RT	Decrease	$5 \times 10^{11} p^+/\text{cm}^2$	
Atkas, <i>et al.</i> , 2004[20]	^{60}Co gamma @ 343 K	I_{ds} @ RT	Increase	300 MRad	
Sattler, 2004[4]	0.45-1.2 MeV electrons @ LNT	I_{ds} I_{gs} @ LNT & RT	Increase @ LNT Increase @ LNT Recovery @ RT	$\leq 6 \times 10^{16} e^-/\text{cm}^2$	
Jarzen, 2005[13]	0.45-0.8 MeV electrons @ LNT	C_{gs} -V @ LNT C_{gs} -V @ LNT post RT anneal	Increase Recovery (some)	$\leq 1 \times 10^{15} e^-/\text{cm}^2$	
Uhlman, 2005[41]	1.0 MeV(eq) Rx spectrum neutrons @ LNT & RT	I_{ds} @ LNT I_{ds} @ RT I_{gs} @ LNT & I_{gs} @ RT	Inc. w/RT recovery No Change Inc. w/RT recovery No Change	$\leq 1.2 \times 10^{16} n/\text{cm}^2$	
Sonia, <i>et al.</i> , 2006 [21][28]	68 MeV p^+ and ions @ RT	I_{ds} @ RT	No Change	Up to $1 \times 10^{13} p^+/\text{cm}^2$ Up to 1×10^{11} ions/ cm^2	
	2 MeV protons @ RT	I_{ds} @ RT	No Change	Up to $1 \times 10^{13} p^+/\text{cm}^2$	
	2 MeV ions @ RT	I_{ds} @ RT	Decrease	$5 \times 10^{10} p^+/\text{cm}^2$	
McClory, 2008[5]	1.0 MeV neutrons @ 84 K	I_{ds} @ 80 K Rev. I_{gs} vs. T @ 82-294 K I_{ds} @ RT I_{ds} @ 80 K after Anneal I_{ds} @ 294 K after Anneal Rev. I_{gs} vs. T @ 82-294 K after Anneal	Increase Increase Decrease Recovery No Recovery No Recovery	$3 \times 10^{10} n/\text{cm}^2$ $3 \times 10^{10} n/\text{cm}^2$ $6 \times 10^{12} n/\text{cm}^2$ $6 \times 10^{12} n/\text{cm}^2$ $6 \times 10^{12} n/\text{cm}^2$ $6 \times 10^{12} n/\text{cm}^2$	

Sonia, et al, [28] determined that with increasing mass of ions used to irradiate AlGaN/GaN heterostructures came greater damage at lower fluences. Using protons and ions of iron, krypton, oxygen, and carbon, they were able determine fluence levels at which device performance began to degrade rapidly, and correlate these fluence levels inversely with increasing particle (ion) mass. They summarized their results by stating that AlGaN/GaN HFET operation is possible in space with appropriate shielding against heavy ions and even for a reasonable time without shielding against protons. The absence of electron irradiation in this research further emphasizes the need for the current research effort.

Donoval, et al, [29], studied the performance of AlGaN/GaN HFETs at temperatures ranging from 300 K to 700 K. The HFETs studied were comprised of a 28nm thick, undoped $\text{Al}_{0.23}\text{GaN}_{0.77}$ layer on top of a $1\mu\text{m}$ undoped GaN layer. Donoval saw an approximate 30% decrease in device saturation drain current and observed that this decline followed closely a $T^{-1.5}$ dependence, indicating the temperature dependence of the 2DEG channel electrons, due to phonon scattering, is the dominant effect during high temperature AlGaN/GaN HFET operation. While this research was conducted without irradiating the devices, it does add to the growing body of research on GaN-alloyed device performance.

Also, Vitusevich, et al, [30] using Cathodoluminescence (CL) spectroscopy was able to confirm improvement in the AlGaN/GaN heterostructures' operational properties after gamma irradiation doses up to 10^6 rad. The researchers attributed the observed mobility improvements (up to 10%) to a dominant process of decreasing density of fast non-radiative centers under gamma irradiation. Further, the relaxation of native defects

(Ga, N, and O) lead to improvement in mobility. The CL was conducted with a scanning electron microscope with electron beam energies of 3, 5, and 20 keV.

Look, Farlow, et al, in 2003 [48], irradiated GaN with 0.42 MeV electrons and observed that at this electron energy only nitrogen displacements within the sub-lattice structure were being produced. Additionally, they were able to conclude that this N displacement was a 70 eV donor. This donor, appearing after low energy electron irradiation of GaN, may be providing additional carriers to the 2DEG formed in the GaN at the AlGaN/GaN interface in our devices.

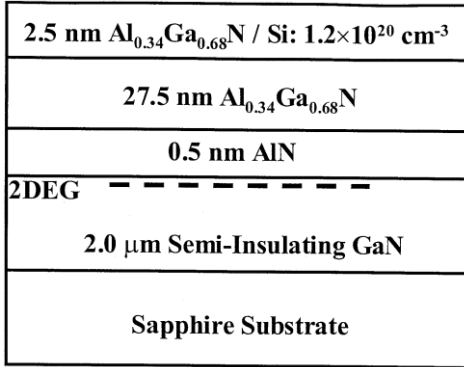


Figure 2. Layer view of AlGaN/AlN/GaN HEMTs studied by Hu, et al, using 1.8 MeV proton radiation [16].

In 2003, Hu, Karmarkar, et al [16], irradiated AlGaN/AlN/GaN high electron mobility transistors (HEMTs), constructed as shown in Figure 2, with 1.8 MeV protons at RT and at fluences up to $3 \times 10^{15} \text{ n/cm}^2$. Figure 2 highlights the differences between Hu's HEMTs and this study's HFETs. Major differences are the 2DEG formation at an AlN-to-GaN interface and the multiple AlGaN layers differentiated by doping. Hu, et al. observed degradation in the form of increased threshold voltage (more positive shift), a

decrease in drain-to-source current, and a decrease in maximum transconductance levels. They attributed the degradations in transistor current to increased carrier scattering and decreased carrier density owing to charged displacement damage/defect centers both inside and outside the 2DEG. However, owing to the infinitesimal thickness of the 2DEG, most charged defect centers are expected to exist outside the 2DEG. These charged defects outside the 2DEG reduce carrier mobility in the 2DEG through Coulombic interactions. The charged defects formed inside the 2DEG are suspected of trapping carriers [16]. A similar process of defect formation in or near the 2DEG could be the mechanism behind observed super recovery (i.e. less than pre-irradiation values) in some devices irradiated with the higher energy electrons (1.0 MeV) in the current study.

In 2002, White, Bataiev, et al [14] used 1.8 MeV protons at RT to study the effects on electrical properties of modulation doped AlGaN/GaN FETs (MODFETs). They observed changes in the electronic properties of the device layers (i.e. lessening in the piezoelectric polarization of the AlGaN and GaN layers) and formation of charged defects in the layers near the channel using low-energy electron-excited nanoscale luminescence (LEEN). Both contributed to an overall reduction in MODFET transistor current and decreased transconductance [14].

Despite the wide range of research documentation available on GaN-based materials and devices, there are few recent articles documenting recent or on-going research into electron irradiation effects and none, except [7] as noted previously, on electron irradiation and the temperature dependent behavior of AlGaN/GaN HFETs specifically. This further underscored the critical need for this research.

III. Theory and Modeling

Al_xGa_{1-x}N/GaN Device Physics

The devices studied during this research were heterostructure field effect transistors (HFETs) based on Al_xGa_{1-x}N/GaN construction. The percentages of Al and Ga in the AlGaN layer for the devices studied were 27 percent aluminum and 73 percent Ga or Al_{0.27}Ga_{0.73}N [5].

Al_xGa_{1-x}N/GaN HFETs are created by growing a thin layer of Al_xGa_{1-x}N on a base of GaN, forming a heterojunction between the layers. GaN is a column III-V (Periodic Table) material, which forms a wurtzite crystalline structure with unequal sharing of electrons in the covalent bonds. This unequal sharing and the non-centrosymmetry of the wurtzite structure results in a piezoelectric polarization in the crystal. Substituting aluminum atoms in place of a pre-determined percentage of gallium atoms creates the Al_xGa_{1-x}N alloy (AlN and GaN), which also has a piezoelectric polarization. The band-gap for AlN is 6.1 eV compared to the GaN band-gap of 3.4 eV. This leads to an intermediate band-gap value for Al_xGa_{1-x}N material based on the percentage of aluminum atoms. For the aluminum mole fraction in these devices, $x = 0.27$, the band-gap is approximately 4.1 eV [5].

The change in polarization at the Al_xGa_{1-x}N/GaN interface results in a net negative charge layer. The Al_xGa_{1-x}N crystalline structure has slightly smaller cellular dimensions than does the GaN crystal (Al_xGa_{1-x}N has a smaller lattice constant) owing to the smaller radii aluminum atoms. This size mismatch requires the Al_xGa_{1-x}N crystal to stretch when matching bonds with the GaN, changing the charge distribution in the

$\text{Al}_x\text{Ga}_{1-x}\text{N}$ and giving rise to this spontaneous polarization pointing in the same direction as the piezoelectric polarization of the GaN and AlGaN layers [2]. Owing to the thicker GaN layer (2 μm), compared to the AlGaN layer (25nm), the AlGaN layer is held under tensile stress after crystalline bonding with the GaN layer. This tensile stressing of the AlGaN layer results in a larger piezoelectric polarization for the AlGaN layer and subsequent increased spontaneous polarization [2]. This spontaneous polarization can cause electric fields of up to 3 MV/cm in group-III-nitride crystals, and strain in some $\text{Al}_x\text{Ga}_{1-x}\text{N}$ /GaN heterostructures can cause an additional piezoelectric field of about 2 MV/cm [2].

These high polarizations and resulting electric fields produce high interface charge densities and spatial separation of the hole and electron wave functions in GaN-based quantum well structures. Additionally, the net polarization in the AlGaN layer, manifested as an electric field oriented perpendicular to the AlGaN/GaN boundary, results in a positive charge collection in the AlGaN layer along the AlGaN/GaN heterojunction [4]. This positive charge at the AlGaN/GaN heterojunction attracts electrons from the GaN into the quantum well at the interface.

Figure 3 contains an inset photo (top view) of one of the HFET devices in the upper left of the figure. Also shown is a side view representation of the HFET and an energy band diagram showing the quantum well as the portion of the E_C (conduction band edge) that dips below the E_F (Fermi energy) level. It is in this region where radiation-induced effects can have significant impact on device operation. Depicted in the upper left corner of Figure 3 are the three leads connected to the drain, source, and gate contacts.

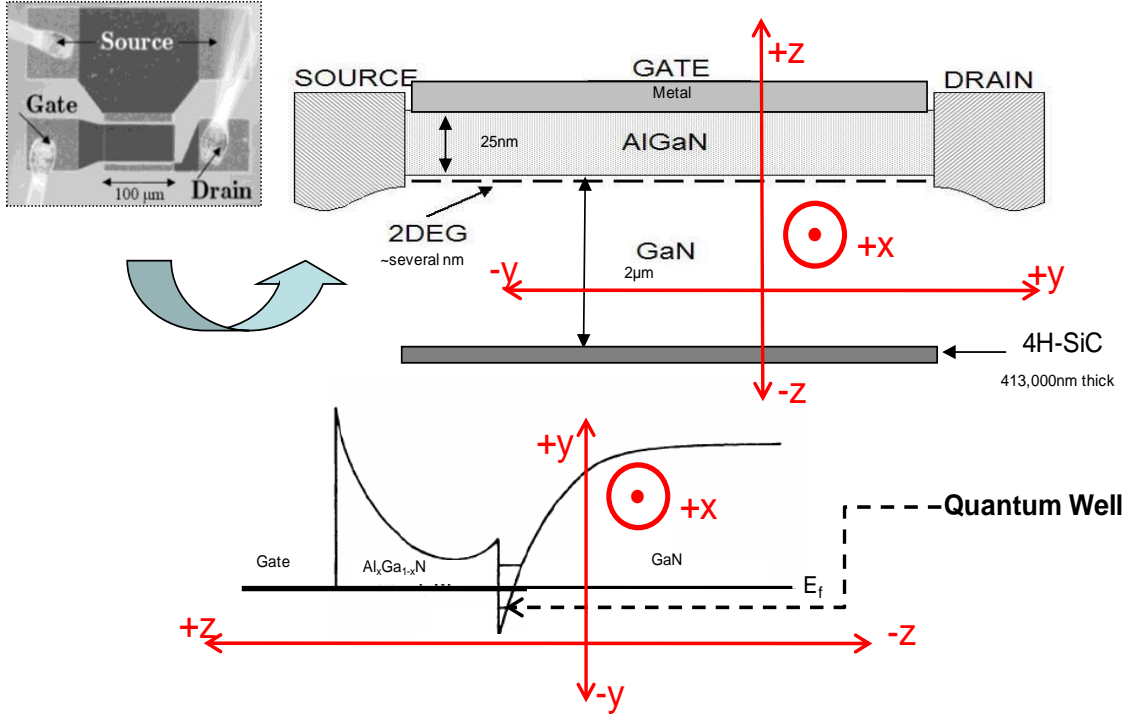


Figure 3. Comparison of TOP and SIDE Views of $\text{Al}_x\text{Ga}_{1-x}\text{N}/\text{GaN}$ HFET, along with Energy Band Diagram Showing Quantum Well and 2DEG Channel [10].

The size of this quantum well is roughly equivalent to an electron's deBroglie wavelength in width. It allows electrons in the well to form a standing wave and move easily in the plane of the interface or heterojunction. These electrons form what is known as a two-dimension electron gas (2DEG) [3]. This 2DEG and the effects of electron irradiation on its magnitude and the mobility of the carriers within are of great interest to this research.

In a study of AlGaN/GaN HFETs grown on 6H-SiC, Gaska, Yang, et al. [56] were able to determine that the mobility of electrons in the 2DEG at LNT was much higher than the $1000 \text{ cm}^2/\text{V}\cdot\text{sec}$ value accepted for bulk GaN. Using Hall measurements at LNT, Gaska and Yang were able to show mobilities ranging from 4000 to 5600

$\text{cm}^2/\text{V}\cdot\text{sec}$ for electrons in the 2DEG formed at the AlGaN/GaN interface in these HFETs with a SiC substrate. The devices used in this study have similar construction [56].

The electrons, collectively referred to as the 2DEG, are contained in the quantum well in the energy levels defined by the well annotated in Figure 3. These electrons enjoy unrestricted movement in the x- and y-plane. Their movements along the z-axis are restricted by the well's energy levels. The 2DEG concentration is approximately 10^{13} electrons/ cm^2 for aluminum molar fractions of approximately 0.30. The 2DEG concentration depends on the AlGaN layer thickness, the Al concentration in the $\text{Al}_x\text{Ga}_{1-x}\text{N}$ layer, and the applied gate voltage that acts to change the depth of the quantum well and hence the degeneracy of the well states that are populated. The well can be collapsed by lowering the potential energy at the gate through application of a negative gate voltage (V_{gs}), with respect to the drain and source ohmic contacts. The negative potential on the gate raises the conduction band edge to the Fermi energy in the 2DEG effectively turning off the device. In these devices, cycling the gate bias can be done very rapidly and accounts for the excellent high-speed performance of $\text{Al}_x\text{Ga}_{1-x}\text{N}/\text{GaN}$ HFETs and their importance to applications that operate at high frequencies [1]. This excellent high frequency performance further highlights the importance of this research in electron-radiation-induced damage mechanisms, their temperature dependence, and their effects on the performance characteristics of GaN based devices.

Theory of Radiation Effects

Electron irradiation of semiconductor material has three potential results. First, the bombarding electrons may pass through the material with no energy loss. Second, the

negatively charged particles may lose their energy through ionizations. Third, the electrons may lose energy through non-ionizing interactions. The ionization energy loss (IEL) is dose rate dependent and transient in duration, while the non-ionizing loss is total dose dependent and can persist for some time post-irradiation. The primary NIEL effect is displacement of constituent atoms leading to vacancies, interstitials, and the formation of defect complexes. This research was particularly interested in the non-ionizing energy losses (NIEL) of the electrons in the GaN and AlGaN materials [5].

NIEL measures the energy transferred to the atoms in the semiconductor lattice during irradiation. The effect of the electrons on the atoms of the material differs depending on the atomic species, binding energy, and electron energies. Expected effects based on energy of the incident electrons can be determined by analyzing the possible energy transfer to the lattice atoms. In order to determine the NIEL in a particular material, a calculation of the radiation dose for the energy level of the impinging particles is required.

The rates of displacement damage formation for the Ga, N, and Al sub-lattice structure depend on both the displacement energy and the maximum transferable energy per collision. The displacement energy depends on the energy binding the atom to the lattice and the angle of the displacement and the fraction of energy transferred depends on the mass of the nucleus and the impact parameter. In order to determine the threshold energy for damage to each sub-lattice, both factors must be taken into account [5].

As electrons enter the AlGaN and GaN layers of the HFETs, they are reduced in energy primarily via inelastic collisions with the atomic electrons. A small amount (less than 1%) is lost in collisions with lattice atoms (Ga, N, or Al). These latter collisions

may cause displacement damage in which lattice atoms are knocked out of their natural position in the lattice. The rates at which displacement damage occurs for Ga and N atoms are functions of both atomic binding energy and transferred energy via the collision. Atomic binding energies are generally intrinsic to a material, and research has shown that Ga atoms are bound less tightly than N atoms in GaN [32]. Energy transferred, during a collision, is heavily dependent on the lattice atom's mass. Therefore, more energy can be transferred to the less massive nitrogen atoms. Minimum displacement energies in GaN have been determined through theoretical calculations. From the data for all collision angles, Ga has a minimum, displacement energy of 22 ± 1 eV while N has a minimum, displacement energy of 25 ± 1 eV [32]; and Al has a minimum displacement energy of approximately 24 eV, based on a comparison of its mass to that of Ga. The maximum energy imparted to an atom in the lattice by an electron of energy E_{e^-} is described in [32], and expressed in Equation (1),

$$E_{trans}^{\max} = 2 \frac{(E_{e^-} + 2m_{e^-}c^2)}{m_{atom}c^2} E_{e^-}, \quad (1)$$

where E_{e^-} is the incident electron energy, m_{e^-} is the electron mass, m_{atom} is the mass of the target atom, and c is the speed of light. Using Equation (1), the maximum energy transferred to a lattice atom from an incident electron may be calculated. Results of this calculation for electron energies, relevant to this research, are shown in Table 5.

Table 5. Max Energy Transferred to Ga and N lattice atoms for specified electron energies.

Atom→ Ee- ↓ [MeV]	Max Energy Transferred[eV]			
	Ga	Si	Al	N
0.45	20.4	50.6	52.7	101.5
0.50	23.4	58.2	60.6	116.7
0.80	44.9	111.4	116.0	223.4
1.00	62.3	154.6	160.9	309.9
1.20	82.1	203.8	212.2	408.7

Of the five incident energies listed in Table 5, all should cause displacements in Al while only the 0.45 MeV electrons should not cause displacements of Ga atoms. The values in this table also indicate that fluences of higher energy electrons (around 1 MeV) may be able to displace atoms and impart enough energy to these displaced atoms to cause knock-on damage, resulting in linear defect patterns. However, results in [32] indicate that large damage cascades (line defects) will probably not result from the primary knock-on atoms because they are limited to approximately 290 eV for N atoms and 41 eV for Ga atoms [32].

When looking at the potential for electron radiation of various energies to cause defects or otherwise affect the properties and operation of the HFETs being evaluated, it is useful to have some idea of the percentage or amount of energy that may be deposited in the various constituent layers of the devices, relative to each other. If an electron is incident on an AlGaN/GaN HFET or onto AlGaN or GaN material layers, the effects of its passage on the material (i.e. defects, ionization, excitation, Frenkel defects, etc.) are dependent on the electron's energy, the thickness of the material it must traverse, and the materials stopping power. For an understanding of these effects, a discussion of stopping power is necessary. Stopping power is defined as the average energy loss per unit of path

length owing to either elastic collisions and/or inelastic Coulombic interactions of the incident electron with the material's bound atomic electrons or to Bremsstrahlung radiation emission in the atomic nucleus' or atomic electrons' electric fields. This lends to two classifications of stopping power; collisional or radiative [52]. Due to the small mass of the incident electrons, with respect to atoms in the material, most collisional stopping power is thought to be due to ionizations and excitations. The most notable difference, between electron energy loss due to collisional stopping power and that due to radiative stopping power, is that energy loss thru collisional stopping power manifests itself and its effects immediately along the electron's path through the material. The x-rays or Bremsstrahlung radiation (radiative stopping power) travels relatively long distances through the material and beyond before expending their total energy [52].

Two series of TIGER (a Monte Carlo Neutral Particle (MCNP) process type code) simulations, run by Sattler [4], provide a good understanding of the differences between collisional and radiative stopping power, as well as where the incident electrons have the highest probability of depositing their energy (dose) within the material layers of the HFETs tested. The first simulation series, Figure 4, produced by Sattler running the XGEN portion of the TIGER code [4], shows a comparison of the stopping powers of electrons in AlGaN and GaN material broken down by collisional and radiative. As a percentage, the amount of electron energy loss in both materials attributable to radiative stopping power is relatively small.

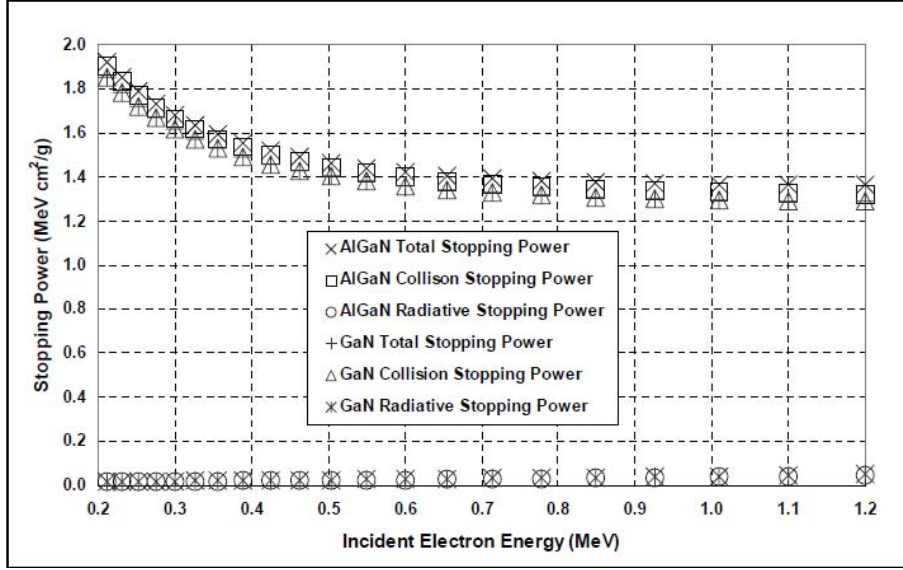


Figure 4. XGEN plot of collisional vs. radiative stopping power in AlGaN and GaN material, taken from Sattler[4].

A second product of Sattler's TIGER simulations, Figure 5, shows the relative differences in the range of electrons in AlGaN and GaN materials, based on their incident energies. This shows that at higher energies, electrons are more likely to penetrate further into the material or device prior to interacting or depositing some or all of its energy [4]. In addition, Figure 6 and Figure 7 are from the TIGER simulations [4]. They depict the expected dose distributions, from a specified fluence at energies of 0.45 MeV or 1.2 MeV electrons, through the gate area of the AlGaN/GaN HFETs tested.

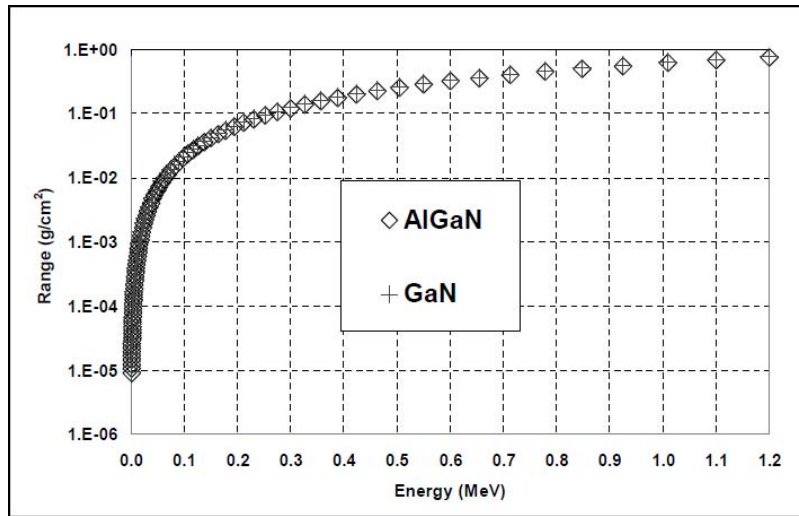


Figure 5. XGEN plot of electron range vs. electron energy in AlGaN and GaN materials, taken from Sattler[4].

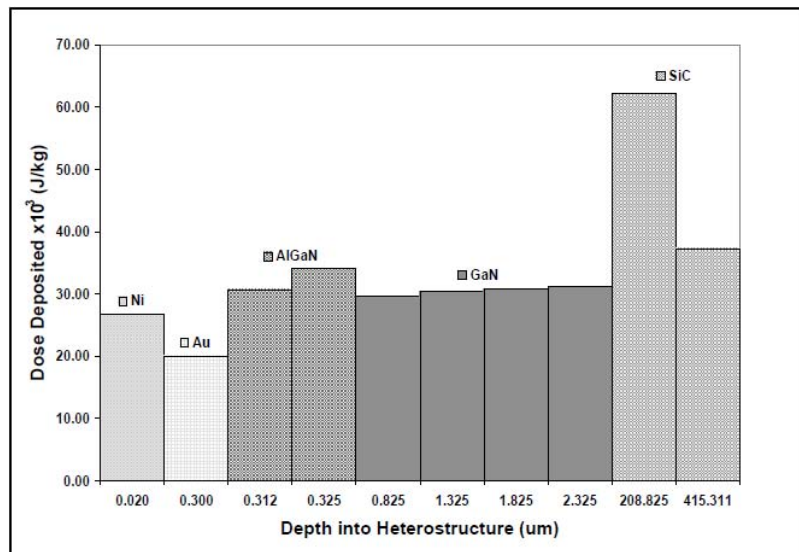


Figure 6. TIGER code graph showing expected dose deposited vs. depth in the HFET's gate region by a total fluence of 1×10^{14} e-/cm² at 0.45 MeV energy, taken from Sattler [4].

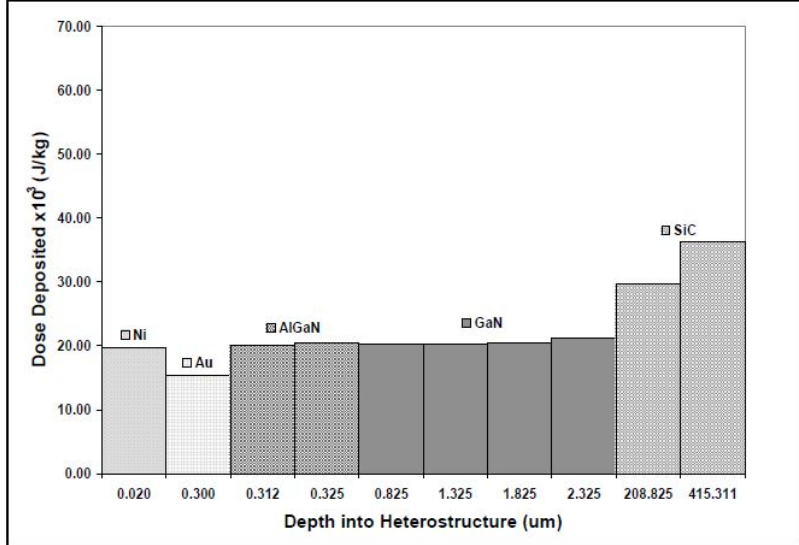


Figure 7. TIGER code graph showing expected dose deposited vs. depth in the HFET's gate region by a total fluence of 1×10^{14} e-/cm² at 1.2 MeV energy, taken from Sattler [4].

The most obvious import of this simulation is that higher energy electrons penetrate further into the device and deposit less of their energy in the relatively shallow gate metal and AlGaN layers; thus having less overall effect on the 2DEG and device operation. Based on these graphs, it is reasonable to suggest that the energy deposited by incident electron irradiation in the AlGaN and GaN layers in these HFETs could decrease by as much as 30 percent with an increase in electron energy from 0.5 MeV to 1.0 MeV at the same fluence.

Also of interest is the marked decrease in energy deposited in the SiC substrate. This would seem to indicate that as electron energy increases, more electrons transit completely through the devices while depositing less energy (dose).

Effects of Si_3N_4 Passivation on AlGaN/GaN HFETs

The effects of applying a silicon nitride (Si_3N_4) passivation layer on the radiation susceptibility of AlGaN/GaN heterostructures are not fully understood at this time. Observations from other research efforts indicate this application enhances the post-irradiation performance of the devices. Theory suggests the Si_3N_4 passivation layer may prevent the surface trapping of negative charges in the upper portions of the AlGaN layer exposed to the atmosphere. These trapped, negative surface charges would effectively reduce and potentially stop transistor current flow through the channel depending on the gate bias applied. The observed higher pre-irradiation transistor current levels for the passivated compared to the unpassivated HFETs studied supports this theory.

Post-irradiation, the effects of device passivation can be analyzed in terms of charge build-up in the Si_3N_4 layer and the effect of these charges on the 2DEG in the channel, at the AlGaN-GaN interface, a mere 25nm away. As the incident electrons pass through the Si_3N_4 passivation layer, they create e-hole pairs through ionization of the Si and N constituents that may then recombine, migrate, or result in immobile positive charges, depending on the applied bias and temperature [42].

Despite application of basic metal-oxide semiconductor (MOS) theory in analysis of radiation-induced effects in the Si_3N_4 passivation layer to some of the HFETs tested, the actual parameters that describe the material behavior are still unknown. This is highlighted in research conducted by Takahashi, et al. [43], in which they seek to better quantify Si_3N_4 parameters through comparisons to silicon dioxide (SiO_2). Observed behaviors of Si_3N_4 -passivated AlGaN/GaN HFETs include a lesser shift in threshold

voltage (V_{th}) and more rapid and complete recovery of drain current levels (I_{ds}) after irradiation [5].

Modeling

This research utilized two models each depicting a critical current parameter (I_{ds} or I_{gs}) for the AlGaN/GaN HFETs studied. Through qualitative and quantitative analysis, using these models the devices' operation and collected data was matched to the associated physics. Additionally, successful application of the selected gate-leakage current model would validate analysis conducted by Gray[10] and McClory[5][8]. It would also provide a potential starting point for determination of a constant or relationship correlating electron irradiation induced effects in these AlGaN/GaN HFETs to those effects observed by McClory[5] using 1 MeV (eq), reactor spectrum neutrons.

Trap Assisted Tunneling (TAT) Model

The first model, the Trap Assisted Tunneling (TTT in [36] or TAT in [5] & [8]) model, proposed in its early form in 2003 by Karmalkar and Sathaiya [35] and further refined by them in 2006 [36] is described by McClory in [5] and Petrosky, et al, in [8]. This model attempts to describe the process by which electrons in the gate metal, under the influence of a negative bias applied to the gate, are able to tunnel through the Schottky barrier to traps formed by defects/vacancies within the 25nm AlGaN material layer, and then tunnel from these traps into the conduction band of the AlGaN layer. Once in the AlGaN layer's conduction band, these electrons are able cross the AlGaN/GaN interface into the quantum well channel and are measured as an increase in the gate leakage current.

TAT is a physics-based model that allows comparison of parameters used to calculate the trap-assisted tunneling component of the gate current at various times (pre-irradiation, post-irradiation, etc.). The basics of this model rely on the fitting of four parameters; φ_B (Schottky barrier height or energy), φ_t (trap ionization energy), N_D (donor concentration in the AlGaN layer), and N_t (trap density in the AlGaN layer). The following provides a brief overview of the TAT model's formulation and application.

Equation (2) is the basic expression of the model and contains two of the four parameters of interest.

$$I_{TAT} = \frac{qA}{E} \int_{\varphi_t}^{\varphi_B + \varphi_F} R d\varphi \quad (2)$$

Here, q is the basic unit of electronic charge, A is the gate area, E is the electric field in the AlGaN layer and is considered constant [5]. Additionally, R represents the total rate at which electrons tunnel from the gate metal into the AlGaN layer and is cumulative of R_1 (tunneling rate into the barrier trap) and R_2 (tunneling rate out of barrier trap into the AlGaN) as defined by Equation(3).

$$(a) R_2 = C_t N_t P_{2_triangle} \quad \text{and} \quad (b) R_1 = C_i f_{FD} N_t P_1 \quad (3)$$

Total trap-assisted tunneling rate, R , is determined by the reciprocal summation of R_1 and R_2 using Equation(4).

$$\frac{1}{R} = \frac{1}{R_1} + \frac{1}{R_2} \quad (4)$$

After substitution of the expressions in Equations (3)(a) and (3)(b), for R_1 and R_2 , the expanded TAT current expression in Equation(5) contains three of these four parameters.

$$I_{TAT} = \frac{qAC_t N_t}{E} \int_{\varphi_t}^{\varphi_B + \varphi_F} \left(\frac{1}{f_{FD} P_1} + \frac{1}{P_{2_triangle}} \right)^{-1} d\varphi \quad (5)$$

In Equation (5), C_t is the material trap energy dependent rate constant [36], f_{FD} is the Fermi-Dirac function for probability of electron occupation of an energy state at a given φ in the metal, N_t is trap density, P_1 is the tunneling probability into the trap, and P_2 is the tunneling probability into the AlGaN from the barrier trap. The E still represents the electric field present in the AlGaN layer. Expressions for C_t , P_1 , P_2 , f_{FD} and α are as follows:

$$C_t = \left(\frac{m_M}{m_{AlGaN}} \right)^{\frac{5}{2}} \frac{16\pi q \varphi_1^{\frac{3}{2}}}{3h \sqrt{\varphi_t - \varphi_1}}, \quad (6)$$

$$(a) P_1 = e^{-\frac{\alpha}{E} \left(\varphi_t^{\frac{3}{2}} - \varphi_1^{\frac{3}{2}} \right)} \quad \text{and} \quad (b) P_{2_triangle} = e^{-\frac{\alpha}{E} \varphi_t^{\frac{3}{2}}}, \quad (7)$$

$$f_{FD} = \frac{1}{1 + e^{\left(\frac{q(\varphi_B - \varphi)}{kT} \right)}}, \quad (8)$$

$$\alpha = \frac{8\pi \sqrt{2m_{AlGaN}q}}{3h}. \quad (9)$$

The fourth parameter, N_D , is contained in the expression for the peak electric field at the gate junction term, E , as expanded and discussed in [36] by Sathaiya, et al.

After substitution of values for parameters that are either material-specific or user-provided, the four parameters mentioned above, φ_B , φ_t , N_D , and N_t , remain as the

unknowns. A MathCAD program of Sathaiya's [36] model was developed by [31] for running the aforementioned physics-based mathematical expressions in loops while the user changes the four parameters' input values sequentially. This program combined with rigorous user analysis provides a best fit curve with experimental data and produces a Relative-Root Mean Squared Error (R-RMSE)[5] value. The parameters are loop-calculated in parallel processes within the program to allow equal weighting of both I_{gs} vs. V_{gs} data taken as temperature is swept from LNT to RT and I_{gs} vs. T (K) at a specific V_{gs} . All experimental data is input from the same body of measurements [36][5][8]. For a more thorough treatment of the utilization of this model, refer to the Modeling Optimization Procedure and Modeling Results sections in [5], or to [8] and [36]. Using this model, [5], was able to obtain fits between experimental data and the model generated curves with R-RMSE values averaging 5×10^{-6} μA compared to I_{gs} current values ranging from $60\mu\text{A}$ to $400\mu\text{A}$. This indicates that the probable error between model and data, at optimized values of the four adjustable parameters, was generally within five percent.

Transistor Current Model

The other model considered in this research was the transistor current model. This is a physics-based, charge control model developed by Rashmi, et al [46]. It is used to analyze the change to the carrier concentration of the 2DEG that determines transistor current, I_{ds} , for the device. In Equation(10), the general expression for the drain current in a MOSFET is modified to account for the dimensional difference between concentration, N ($\#/m^3$), and sheet density, n_s ($\#/m^2$) [51].

$$I_{DS} = -\frac{Q_{inv}WL}{t_r} = -qn_sWv \quad (10)$$

Where q is the basic charge, n_s is the sheet charge density in the 2DEG, W is the width of the gate region, and v is the electron drift velocity. Defining the n_s term and simplifying it with the substitution of $V_{th}(m)$ yields Equation (11) [46];

$$n_s = \frac{\varepsilon(m)}{q(d_d + d_i)} \left(V_{gs} - V_{th}(m) - \frac{E_F}{q} \right), \quad (11)$$

where $\varepsilon(m)$ is the Al/Ga molar specific dielectric constant for the AlGaN layer, d_d is the doped AlGaN layer thickness, d_i is the undoped AlGaN spacer layer thickness, $V_{th}(m)$ is the polarization-dependent threshold voltage, and E_F is the Fermi energy. Using an undoped AlGaN layer, as in this study, d_d and d_i combine to just d , as seen in Equation (12). Using this expression from Rashmi, et al., McClory [5] examined the dependencies and produced a derivative equation relating the change in n_s with radiation-induced shifts in V_{th} as shown in Equation(12).

$$\Delta n_s = \frac{\varepsilon(x)}{qd} - \Delta V_{th} \quad (12)$$

Where $\varepsilon(x)$ is the dielectric constant of the AlGaN, q is the basic elemental charge, and d is the average thickness of the AlGaN layer mentioned above. Threshold voltage, V_{th} , is determined using a method listed in [40] in which an extrapolation of the linear region of I_{ds} vs. V_{gs} curves is used to determine the gate voltage intercept value (V_{gsi}); the point at which the linear extrapolation intersects the x-axis (V_{gs}) and the y-value (I_{ds}) is zero. The linear extrapolation relationship is presented in Equation (13) from [40].

$$V_{th} = V_{gsi} - \frac{V_{ds}}{2} \quad (13)$$

Here, V_{ds} was held at +1.0 V throughout the range of gate voltages examined. A plot of I_{ds} vs. V_{gs} in Figure 15 in the following chapter highlights the linear extrapolation process. By comparing values of V_{th} from pre- and post-irradiation plots of I_{ds} vs. V_{gs} , and using Equation(12), an estimate can be made of the electron radiation-induced contribution to sheet charge carrier density, n_s , in the 2DEG.

IV. Experimental Procedures

Prior to device preparation, test gear assembly, or any irradiations, it was necessary to develop a systematic process to take the research from the conceptual phase to the point at which collected data can be analyzed. Many steps were necessary prior to any electron irradiation of the HFETs, these included:

- packaging the fabricated AlGaN/GaN reticles
- attaching leads
- taking RT I-V curves to determine correct device operation
- conducting thermal break-in of the devices
- determining the measurements to be taken and how they would be taken
- designing a device test assembly and a test-control/connector box
- determining how the devices would be handled and stored during the entire research project to prevent effects due to prolonged exposure to incident light

The description and execution of each of these steps comprise this chapter.

AlGaN HFET Production, Preparation, and Pre-Characterization

The AlGaN/GaN HFETs used were constructed from AlGaN/GaN heterostructure wafers manufactured by Cree, Inc. The wafers were produced using the Metal-Organic Vapor-Phase Epitaxy (MOVPE) process with a 4H-SiC substrate, a nucleation and buffer layer of GaN, and an epilayer of $\text{Al}_{0.27}\text{Ga}_{0.73}\text{N}$ (0.27 mole fraction of AlN and 0.73 mole fraction of GaN). Once the three-quarter $\text{Al}_{0.27}\text{Ga}_{0.73}\text{N}$ /GaN wafers were procured, Sattler [4] conducted transistor fabrication with assistance and facilities provided by Air

Force Research Laboratory (AFRL) Sensors Directorate Aerospace Components and Subsystems Technology Electron Devices Branch (SNDD). For more details of HFET fabrication and packaging refer to Sattler [4]. Figure 8 shows the layering of a device after SNDD fabrication and addition of the metal gate, drain and source contacts.

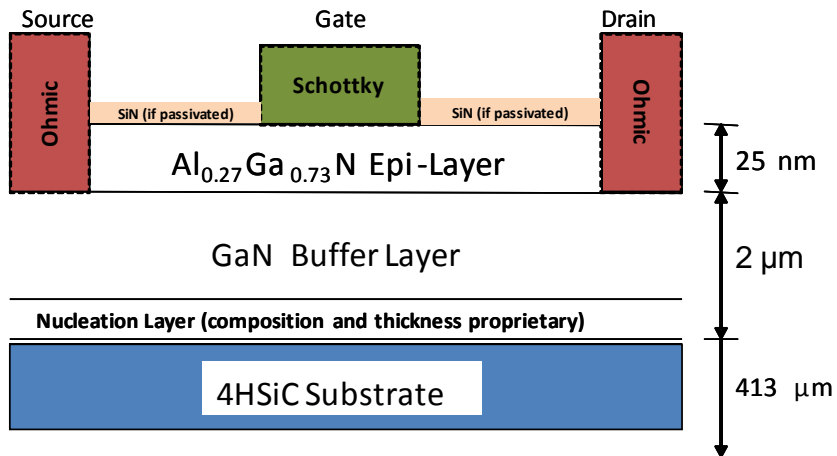


Figure 8. Composition side view of AlGaN/GaN HFETs used [5].

The GaN and AlGaN layers are nominally undoped with a room temperature channel carrier concentration of $1.3 \times 10^{13} \text{ cm}^{-2}$ and mobility of $1300 \text{ cm}^2/\text{V}\cdot\text{s}$ as measured by the manufacturer [4][5]. Figure 9 shows a diagram of the FatFET fabricated on a reticle made with the Cree wafer by AFRL SNDD. Note the FatFET has roughly 20 times the gate surface area or mesa area, $3.75 \times 10^{-5} \text{ cm}^2$, of the other FETs on the reticle. This difference makes the FatFET the preferred of all the FETs on the reticle for this irradiation study.

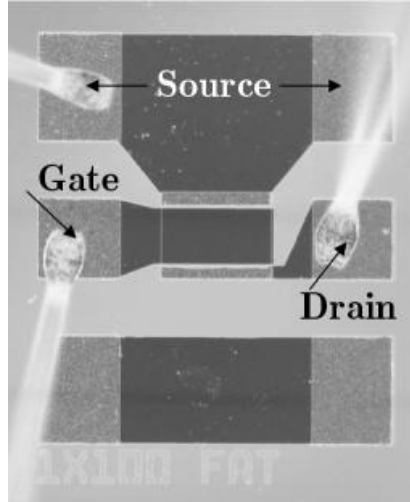


Figure 9. FatFET layout, as constructed on the reticle, showing package leads connected to Shottky gate contact and ohmic drain and source contacts. The FatFET is the HFET actually used in this research [4].

The finished product, measuring 1.7cm x 2.7cm after packaging for testing, is shown on the left side of Figure 10 [4]. Once the Cree wafer underwent device fabrication and the individual reticles were packaged it was necessary to select the most compatible devices for testing. The devices were of two types; unpassivated and Si_3N_4 -passivated. Eight unpassivated and four Si_3N_4 -passivated AlGaN/GaN HFETs were used as the primary research samples.

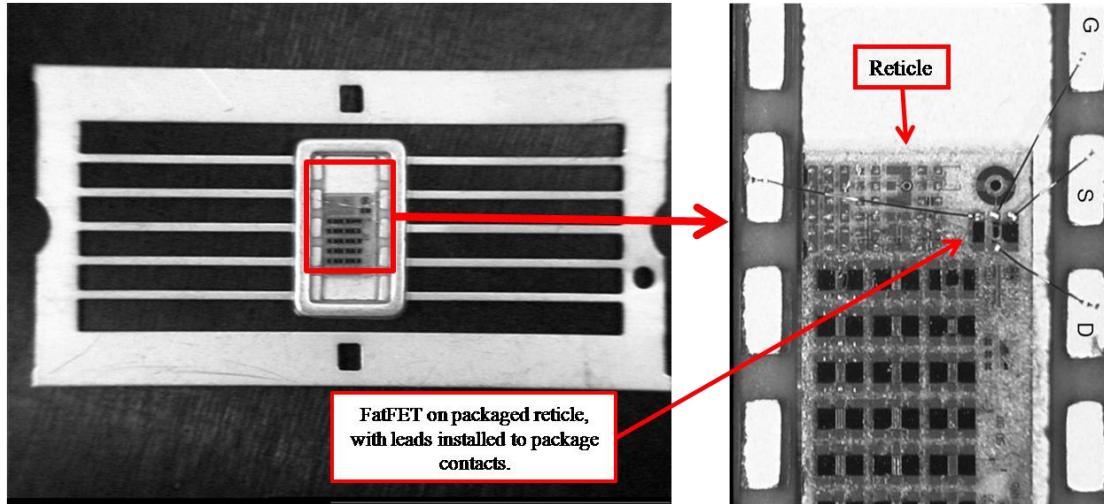


Figure 10. Packaged Reticle with FatFET highlighted. Note: Only the 3 upper right leads, of the 10 installed leads are used.

The package frames were tailored to provide access to the gate, drain, and source package leads to facilitate device operation verification using the ZIF test block as shown in the lower right portion of Figure 11. Once a packaged HFET was verified to be operating as expected based on response curves and data provided from previous AFIT AlGaN/GaN HFET research[4][5][10][13], 6-inch, #30 wire extensions were soldered onto the relatively short package leads for the gate (green), drain (blue), and source (yellow). Two HFETs with these leads installed are visible on the cold-finger in the upper middle of Figure 11.

The devices were subjected to repeated cycles of temperature variations from LNT (≈ 85 K) to RT (≈ 297 K). This repeated cycling or thermal break-in was necessary to reduce the variations in transistor or gate leakage currents based solely on repeated temperature changes instead of the desired electron radiation induced effects.

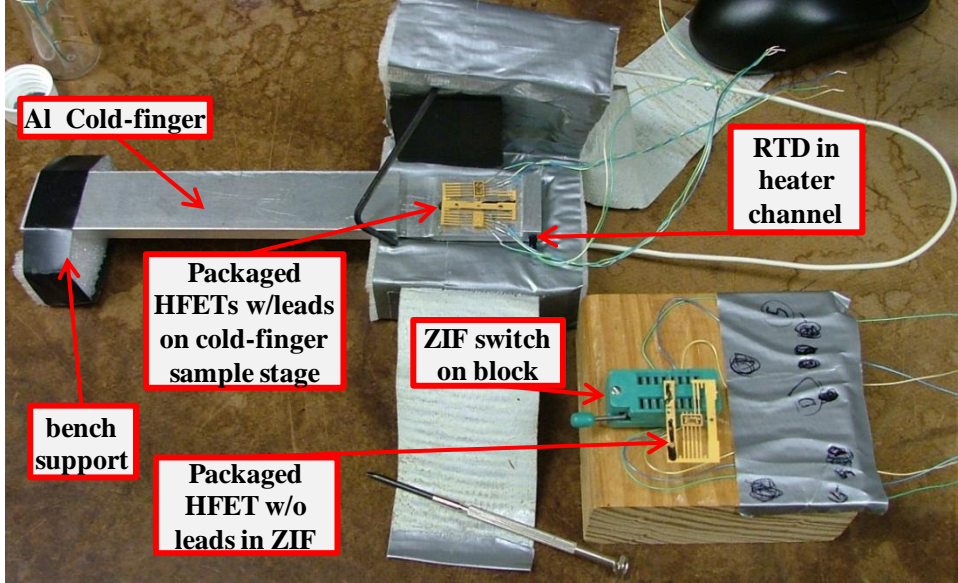


Figure 11. (Upper Left) Packaged HFETs positioned on Cold-Finger. (Lower Right) ZIF-switch test block with packaged reticle for initial device operational check.

In previous AlGaN/GaN HFET research at AFIT [5], a similar process was used. During that research, multiple alternating cycles from LNT to RT to LNT and back to RT were run in which I_{gs} vs. T curves, at $V_{gs} = -4$ V, were taken at temperature intervals of 2 degrees Kelvin. These curves were compared, averaged, and a plot with the standard deviation, for the average value at each temperature, plotted as error bars. The standard deviation was determined by taking the square root of the averaged I_{gs} value at each temperature increment. These plots from [5] are shown in Figure 12.

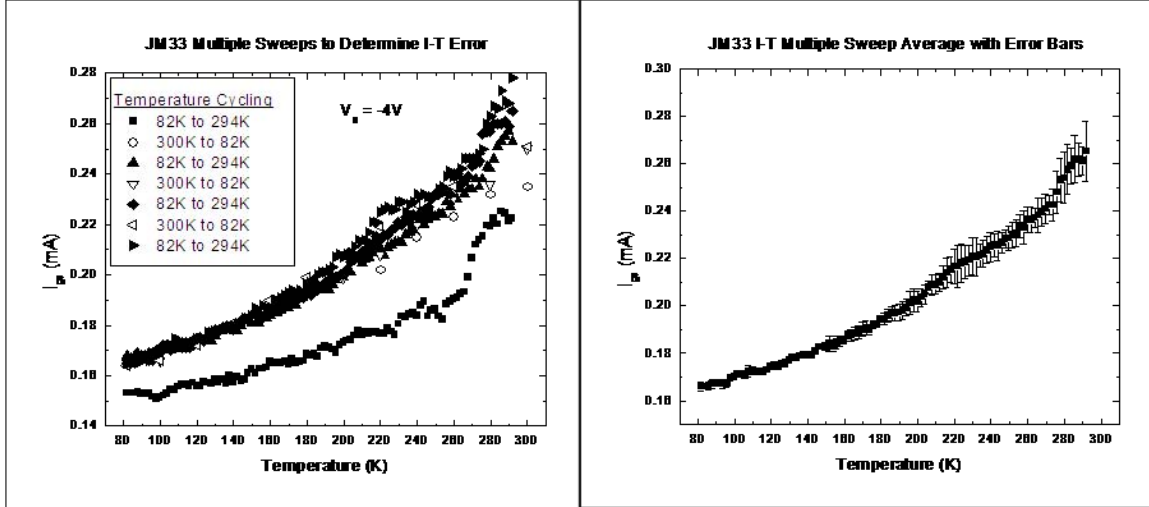


Figure 12. HFET thermal break-in I_{gs} vs. T curves (Left) and average values of these curves plotted with one SD error bars (Right) [5].

The left plot, in Figure 12, highlights the close overlay of the second through seventh I_{gs} vs. T curves. It further indicates that primary break-in occurred during the first cycle from RT to LNT to RT. Most temperature-dependent defects or material issues, affecting I_{gs} , were effectively resolved in the first temperature cycle sweep as temperature increased.

All devices used in this study were subjected to a minimum of seven (some received 10) temperature sweeps (RT to LNT to RT) between their initial device-testing I_{ds} vs. V_{ds} at RT and their initial full regimen of pre-characterization measurements. Starting at initial pre-characterization, each device underwent seven distinct measurements during every temperature cycle (RT-LNT-RT). These measurements are discussed in detail in the next section.

Error analysis for the current and capacitance measurements collected in this study were conducted to determine the percent error attributable to variations in repetitive

measurements of the same electrical property in a device. The results are presented in Table 6 and are applied to the summary of research results presented in Table 13. Ten measurements were taken of individual electrical parameters (i.e. current and capacitance) for several devices in the study. The repetitive measurements were taken at 5 to 8 minute intervals and at LNT and RT. Current or capacitance values for all ten iterations at each voltage increment were averaged and the standard deviation (sigma) at each voltage was taken. The standard deviation was divided by the average obtaining the relative values. The average maximum of these values is displayed in both absolute magnitude and percentage in Table 6.

Table 6. Results from repetitive measurements to determine percent error in observed changes in electrical properties of HFETs in this study.

	Actual and Percent Values for 1 Sigma vs. Averaged Measurements							
	LNT				RT			
	Current		Cap.		Current		Cap.	
	[mA]	[%]	[pF]	[%]	[mA]	[%]	[pF]	[%]
Unpassivated	2.21E-02	2.206%	2.52E-03	0.252%	4.90E-02	4.898%	1.08E-02	1.077%
Passivated	6.51E-03	0.651%	1.03E-02	1.030%	3.70E-03	0.370%	4.09E-03	0.409%

Applying these to post-irradiation changes in electrical parameters, the percentages in Table 6 are inserted with a (+/-) after each current or capacitance observed percentage change in Table 13.

Pre-Irradiation Characterization

After the thermal break-in was complete, all devices underwent pre-characterization measurements. The same four measurements with associated

temperatures and temperature sweeps conducted during the research were performed. The plots in this section highlight the similarities and differences in these pre-irradiation measurements between passivated vs. unpassivated devices and LNT vs. RT.

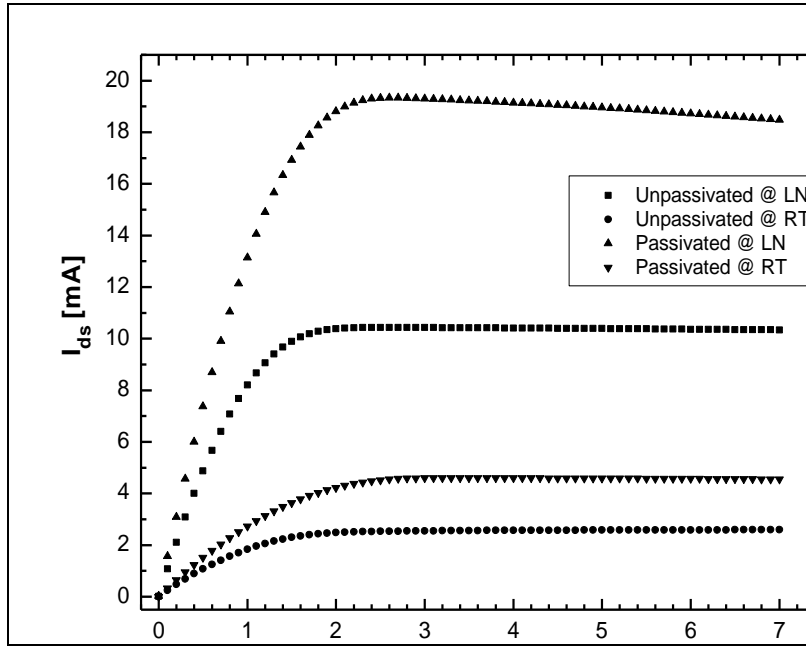


Figure 13. Plot of pre-irradiation averaged drain to source currents for eight unpassivated and four passivated HFETs tested at LNT and RT at $V_{gs} = -2$ V.

In Figure 13, pre-irradiation drain to source currents (I_{ds}) at liquid nitrogen temperature (LNT) in the unpassivated HFETs saturate between 8mA and 14mA, while those for the passivated HFETs saturate between 17mA and 21mA. The higher saturation levels for the passivated devices may result from the Si_3N_4 passivation layer preventing negative surface charge build-up. This build-up in the unpassivated devices may serve to enhance the effects of the negative gate bias (making it appear greater in magnitude), thereby decreasing the 2DEG in the channel region. Also of interest in the pre-irradiation measurements was the difference between drain currents at LNT and at RT also depicted

in Figure 13. On average, for both unpassivated and passivated HFETs studied here, the pre-irradiation drain currents were five times greater at LNT than at RT. This reduction in drain currents at RT is caused by increased lattice scattering of the carriers at higher temperatures. The temperature dependence of carrier mobility in GaN and some other common semiconductors is proportional to T^{-x} , where x for bulk GaN was determined to be 2.3 for electrons and 6.0 for holes [51][55]. The negative exponent values indicate the mobility, μ , decreases as temperature, T , goes up. This decrease in mobility as temperature increases coincides perfectly with the drain current behavior observed in the HFETs studied.

The linear extrapolation method for characterizing FET threshold voltages incorporating Equation (13) was used [40]. The intersection of the extrapolated linear regions and the x-axis yields the V_{gis} term. Figure 14 shows the region of the I_{ds} vs. V_{gs} curves analyzed in the linear extrapolation process using Equation (13). A comparison of pre-irradiation threshold voltage values, for unpassivated HFETs can be seen in Figure 15.

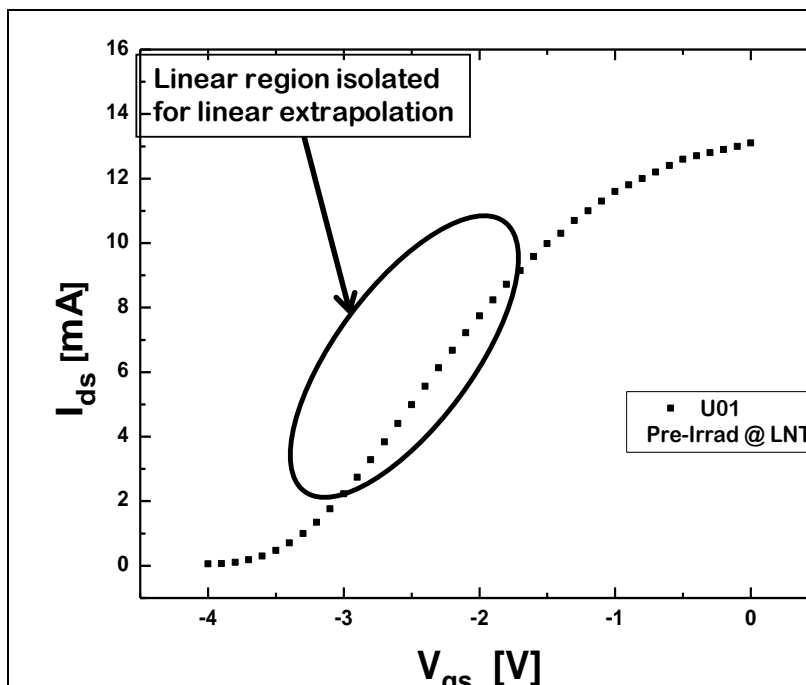


Figure 14. Highlighting linear region in I_{ds} vs. V_{gs} curves for U01.

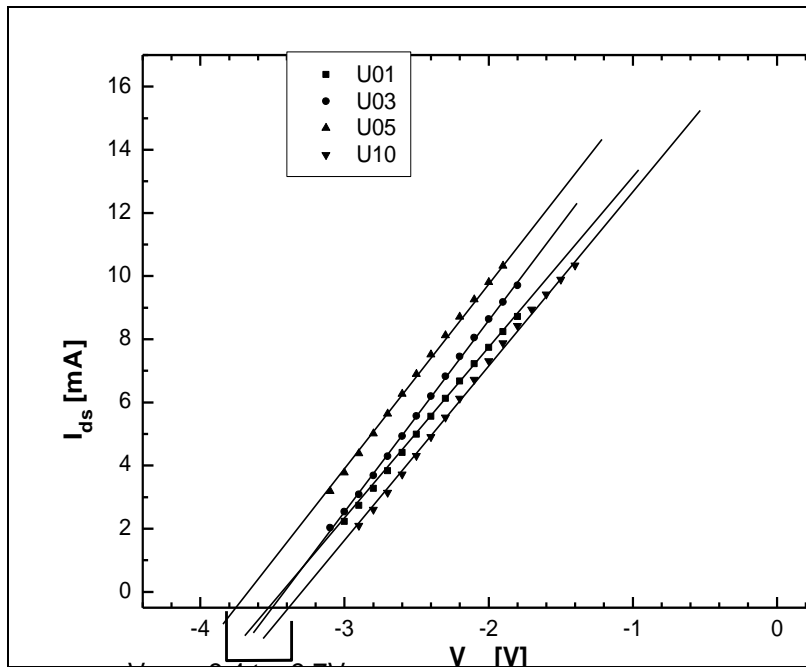


Figure 15. Linear extrapolation method applied to linear regions of four unpassivated HFET curves. Temperature made little difference in V_{th} . Passivation added an average -0.6 V to unpassivated V_{th} values of -4 V to -4.3 V. The R^2 values for the isolated portions shown in this figure are better than 0.999.

The pre-irradiation difference in threshold voltages between the passivated and unpassivated HFETs used in this study can also be seen in the gate to channel capacitance, C_{gs} , vs. gate voltage curves in Figure 16. In Figure 16, the vertical arrows were inserted to indicate the gate voltage values corresponding to the mid-points of the capacitance curves' linear (depletion) regions. Comparing these values to those obtained via linear extrapolation in conjunction with Figure 15 shows close agreement.

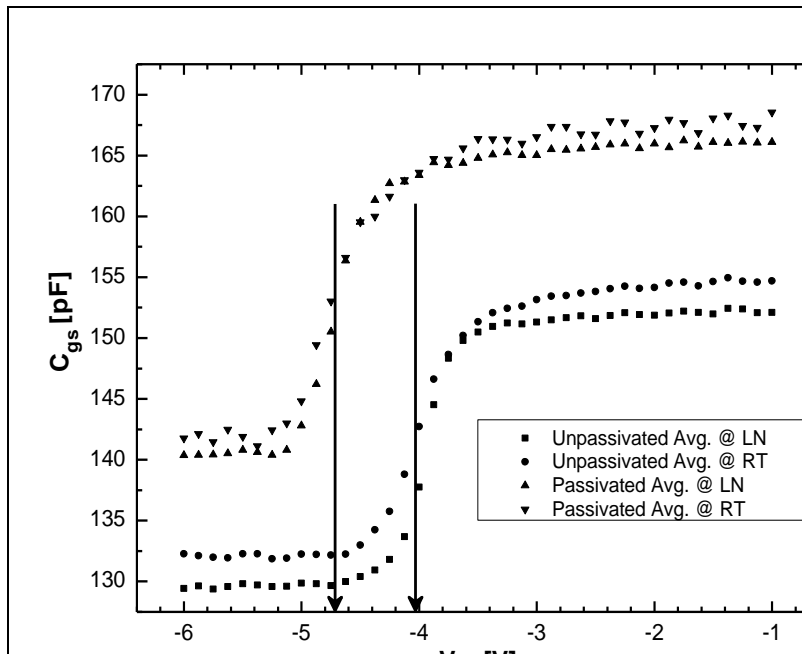


Figure 16. Comparisons of averaged pre-irradiation gate capacitance vs. gate voltage for unpassivated and passivated HFETs at both LNT and RT. Arrows indicate approximate threshold voltage values.

Results for the pre-irradiation characterization values of gate leakage current vs. temperature, where V_{gs} was held at -4 V and temperature was steadily increased from 96 K to 292 K, can be seen in Figure 17. These curves are the averaged unpassivated and passivated individual device data. Even pre-irradiation, some of the obvious benefits of

Si_3N_4 passivation are apparent. The maximum average value of gate leakage current for the passivated devices is roughly half that for the unpassivated HFETs. Further, the curves for the individual passivated devices were relatively smoother and more regular, even at the upper end of the temperature range, than were those for the unpassivated devices.

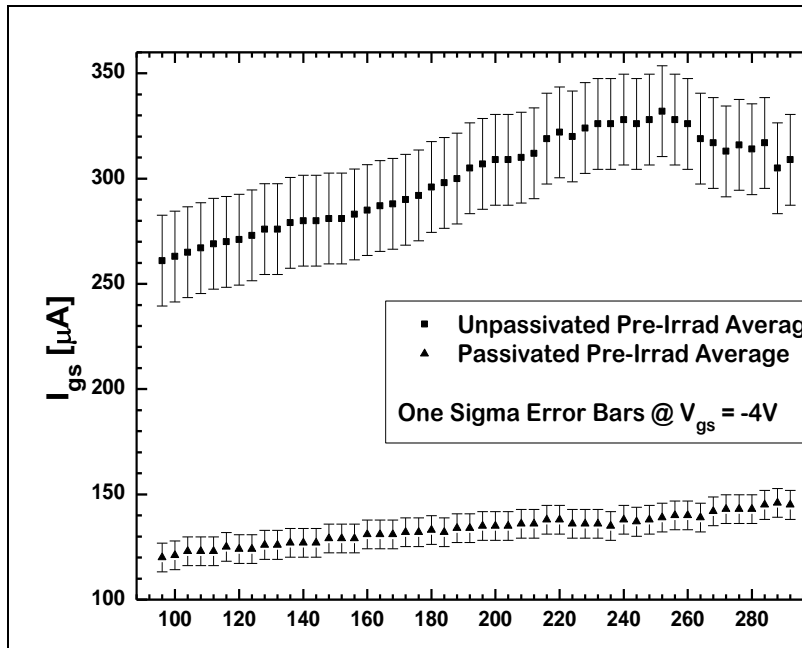


Figure 17. Plot of averaged pre-irradiation gate leakage current vs. temperature at $V_{\text{gs}} = -4$ V and showing one sigma error bars. The highest gate leakage current value is 0.33mA for the unpassivated, and roughly half that, at 0.15mA for the passivated HFETs.

Overall, the pre-irradiation characterization data seems to indicate there are benefits to adding the Si_3N_4 passivation layer to the exposed AlGaN surfaces between the gate and source and drain contacts. More discussion regarding the effects and the pros and cons of passivation will be provided in chapters 5 and 6.

Experimental Apparatus

In order to streamline the data collection process a switching and control test box (SCTB) pictured in Figure 18 with its wiring schematic in Figure 19 was designed and constructed. This test box allowed rapid realignment of the Keithley Source Measurement Units (SMU) and Capacitance Voltage Analyzer (CVA) leads as well as rapid switching between HFET devices. It improved the capability to collect full, accurate, and repeatable electrical measurements while varying or maintaining temperature at predetermined levels.

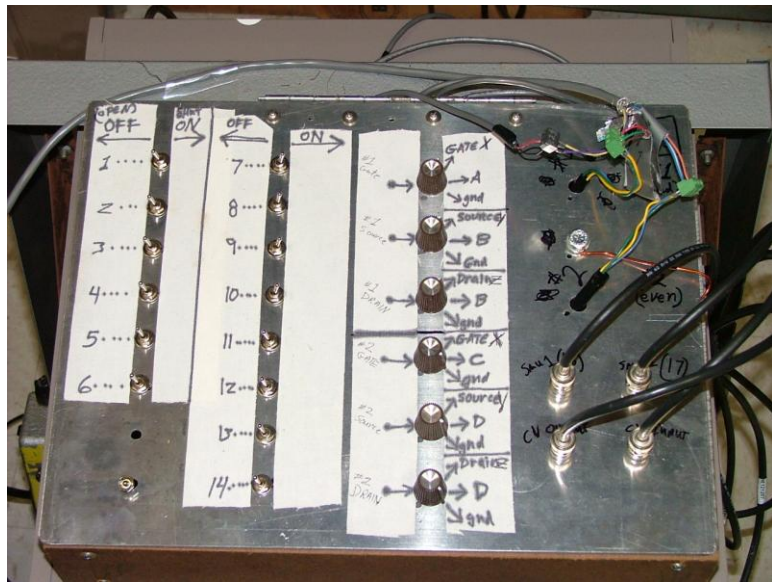


Figure 18. Switching Control Test Box. Shown with cold-head leads, two SMUs, and CVA connected.

Figure 19 depicts the two SMUs controllable by laptop #1 or #2, the CVA controlled by laptop #1, and dual HFET connectivity. This connectivity schematic was designed to allow rapid selection between the two devices mounted on the cold-head

sample stage inside the vacuum chamber or on the cold-finger suspended inside a LN₂-filled Dewar vessel during pre-characterizations or post-irradiation anneal checks. There are 14 double-pole, double-throw (dp-dt) toggle switches and six three-position, rotary knob switches on the SCTB.

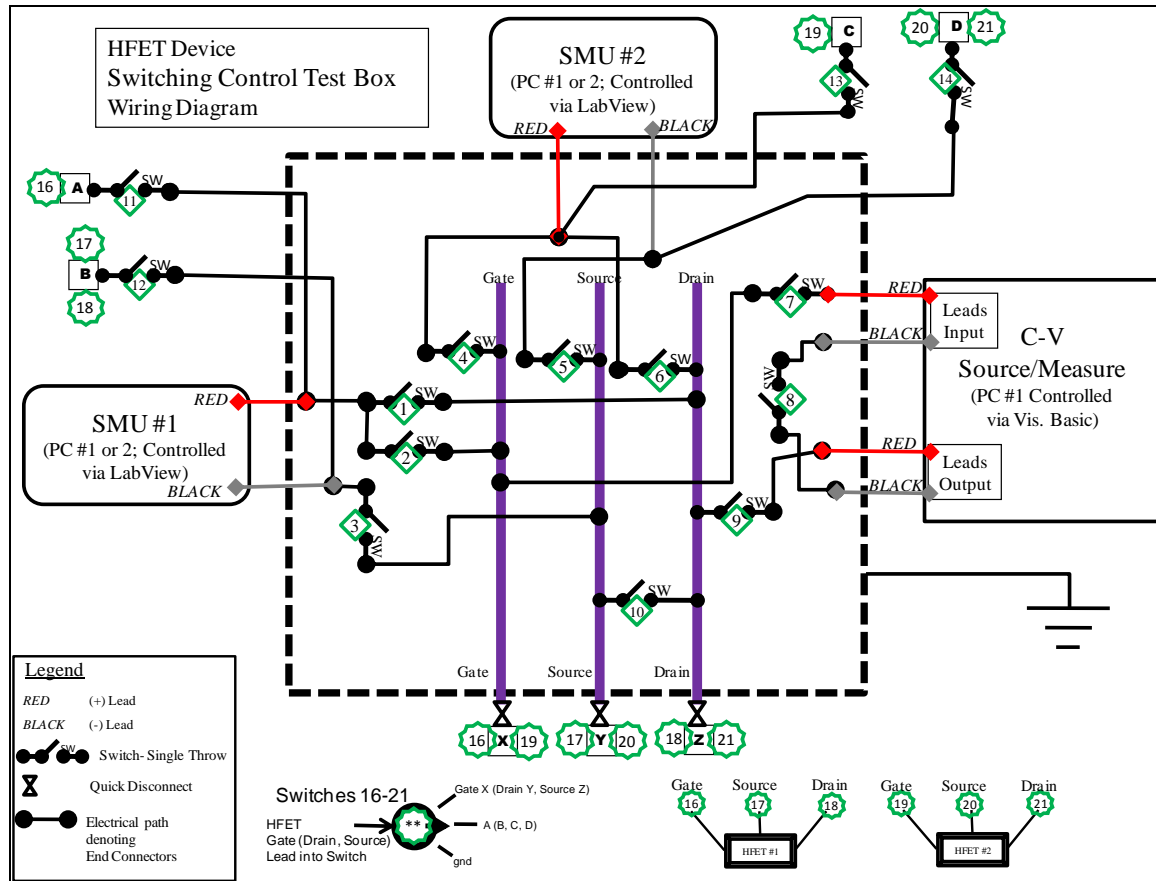


Figure 19. HFET Device Switching Control Test Box (SCTB) wiring schematic.

Table 7 and Table 8 provide the SCTB switch and knob positioning necessary to take the required electrical measurements.

Table 7. SCTB Toggle Switch positions for each of the 4 measurements taken; same at LNT or RT.

SWITCHING CONTROL TEST BOX Toggle Switch Position Guide														
Switch # →	1	2	3	4	5	6	7	8	9	10	11	12	13	14
Positions → / Meas. ↓	Open/ Closed													
Ids vs. Vds	open	closed	closed	open	closed	closed	open							
Ids vs. Vgs	open	closed	closed	open	closed	closed	open							
Cgs vs. Vgs	open	open	open	open	open	open	closed	closed	closed	closed	open	open	open	open
Igs vs. Vgs	open	closed	closed	closed	closed									
Key →	open means OFF				closed means ON									

Table 8. SCTB 3-way rotary switch positions for each of the 4 measurements taken; same at LNT or RT.

SWITCHING CONTROL TEST BOX Knob Switch Positions						
Knob Switch →	HFET Input #1			HFET Input #2		
	Gate #1	Source #1	Drain #1	Gate #2	Source #2	Drain #2
Positions → / Measure ↓	gate A gnd	source B gnd	drain B gnd	gate C gnd	source D gnd	drain D gnd
Ids vs. Vds *	gate	source	drain	gnd	gnd	gnd
Ids vs. Vgs *	gate	source	drain	gnd	gnd	gnd
Cgs vs. Vgs *	gate	source	drain	gnd	gnd	gnd
Igs vs. Vgs**	A	B	B	C	D	D
* Example for measuring #1 device #2 in Stby.						
** Here, both devices are measured simultaneously.						

After the SCTB was constructed, two HFETs were selected and prepared for use as system test devices. These devices were used to verify correct and repetitive operation of the test box, SMUs, CVA, Lakeshore 331 Temperature Monitor and Controller, National Instruments General Purpose Interface Buses (GPIBs), laptops, Visual Basic C_{gs} vs. V_{gs} program, and LabView I_{gs} vs. V_{gs} vs. T, and I_{ds} vs. V_{ds} or V_{gs} programs. Verification of proper system operation over the range of temperatures, voltages, and current required was achieved from a review of previous research [4][5][10][13] and published texts [12][51]. The full range of electrical property measurements was

performed on these devices; at RT, at LNT, during the temperature increase from LNT to RT, and again at RT.

The cold-head used during this research was designed by the author and constructed by the AFIT machine/fabrication shop. It was constructed of non-magnetic stainless steel and provides a 3-inch diameter sample stage for mounting devices undergoing electron irradiation in a cooled, vacuum environment. To achieve the low temperatures required for this research, liquid nitrogen was supplied to the cold-head's hollow, sample stage core to provide near 77 K cooling of the HFETs during irradiation. The two vacuum certified, electrical pass-thru flanges and their associated wiring harnesses were procured from the Lesker Co.

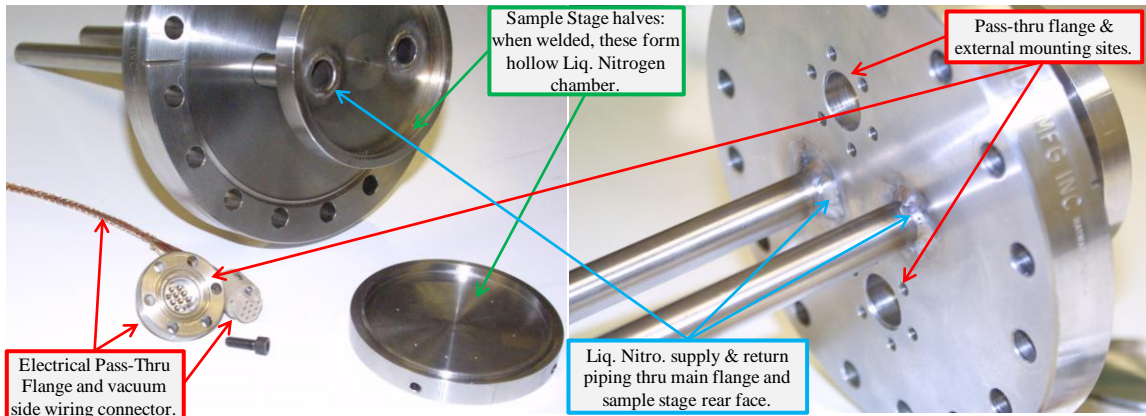


Figure 20. Cold-Head (pre-welding), showing the sample stage's hollow chamber, the flanged electrical pass-throughs, and the LN supply/return pipes.

Visible in Figure 20 are the components of the stainless cold-head prior to final assembly and welding. Note the two 0.125 inch diameter holes in the outer edge of the sample stage front section. These openings are the ends of an enclosed RTD or heater

channel. Two of these tubular channels were bored, parallel to and opposite each other, in the sample stage front section. These holes can be used to emplace 0.125 inch cylindrical ceramic heaters to control sample temperature or to house a resistance temperature detector (RTD). Either or both devices may be used with a Lakeshore 331 controller to either control or monitor (or both) device temperatures on the cold-head sample stage.

Data Collection

After the thermal break-in was complete, all devices underwent a pre-characterization. Matching pairs (pairs selected based on passivation status and comparison of initial test curves) were placed on the cold-finger, connected to the switching control test box, and cooled to LNT. They were subjected to the full range of electrical property measurements at LNT, gate current vs. gate voltage was collected as temperature increased to RT, and the full range of measurements were taken at RT. The same measurements were performed post-irradiation and after RT anneals of 12, 24, 36 and 48 days. Additionally, HFETs U01 and U02 were subjected to 60-day post-irradiation RT anneal measurements.

The HFETs were exposed to electron fluences in the range of 5×10^{14} to 5×10^{15} electrons/cm² using mono-energetic electrons with energies of 0.5 and 1.0 MeV from the Wright State University's Van de Graff generator (VDG). Throughout the irradiations phase of this project, the VDG typically provided an electron beam current of between 0.2 μ A and 0.6 μ A. Table 9 shows the devices, irradiations, fluences, energies, and

measurements taken during this research. In this table, the measurement blocks containing “N/A” indicates that these measurements were not performed.

Table 9. Inventory of devices, fluences, electron energies, and measurements taken.

Action Taken → / Device ↓	Pre-Irrad		Post-Irradiation						
	Pre-Rad Break-in	Data Taken @ LN & RT	Irrad Cycle # / Date	Fluence [e-/cm^2]	Post-Irrad Data Taken @ LN & RT	12day Anneal Data Taken @ LN & RT	24day Anneal Data Taken @ LN & RT	36day Anneal Data Taken @ LN & RT	48day Anneal Data Taken @ LN & RT
U01	10 cycles LN-RT	Ids v Vds Ids v Vgs Cgs v Vgs Igs v Vgs	1 / 20Oct08	5x10^14 @ 0.5MeV	Ids v Vds Ids v Vgs Cgs v Vgs Igs v Vgs	Ids v Vds Ids v Vgs Cgs v Vgs Igs v Vgs	Ids v Vds Ids v Vgs Cgs v Vgs Igs v Vgs	Ids v Vds Ids v Vgs Cgs v Vgs Igs v Vgs	Ids v Vds Ids v Vgs Cgs v Vgs Igs v Vgs
U02									
U03	10 cycles LN-RT	Ids v Vds Ids v Vgs Cgs v Vgs Igs v Vgs	1 / 29Oct08	5x10^14 @ 1.0MeV	Ids v Vds Ids v Vgs Cgs v Vgs Igs v Vgs	Ids v Vds Ids v Vgs Cgs v Vgs Igs v Vgs	Ids v Vds Ids v Vgs Cgs v Vgs Igs v Vgs	Ids v Vds Ids v Vgs Cgs v Vgs Igs v Vgs	Ids v Vds Ids v Vgs Cgs v Vgs Igs v Vgs
U04									
U05	7 cycles LN-RT	Ids v Vds Ids v Vgs Cgs v Vgs Igs v Vgs	1 / 3Nov08	5x10^15 @ 0.5MeV	Ids v Vds Ids v Vgs Cgs v Vgs Igs v Vgs	N/A	Ids v Vds Ids v Vgs Cgs v Vgs Igs v Vgs	Ids v Vds Ids v Vgs Cgs v Vgs Igs v Vgs	Ids v Vds Ids v Vgs Cgs v Vgs Igs v Vgs
U08			Bad LN [212°K]						
U09	7 cycles LN-RT	Ids v Vds Ids v Vgs Cgs v Vgs Igs v Vgs	1 / 5Nov08	1x10^15 @ 0.5MeV	Ids v Vds Ids v Vgs Cgs v Vgs Igs v Vgs	Ids v Vds Ids v Vgs Cgs v Vgs Igs v Vgs	Ids v Vds Ids v Vgs Cgs v Vgs Igs v Vgs	Ids v Vds Ids v Vgs Cgs v Vgs Igs v Vgs	Ids v Vds Ids v Vgs Cgs v Vgs Igs v Vgs
U10									
P01	10 cycles LN-RT	Ids v Vds Ids v Vgs Cgs v Vgs Igs v Vgs	1 / 30Oct08	5x10^14 @ 0.5MeV	Ids v Vds Ids v Vgs Cgs v Vgs Igs v Vgs	Ids v Vds Ids v Vgs Cgs v Vgs Igs v Vgs	Ids v Vds Ids v Vgs Cgs v Vgs Igs v Vgs	Ids v Vds Ids v Vgs Cgs v Vgs Igs v Vgs	Ids v Vds Ids v Vgs Cgs v Vgs Igs v Vgs
P02									
P03	7 cycles LN-RT	Ids v Vds Ids v Vgs Cgs v Vgs Igs v Vgs	1 / 7Nov08	2x10^15 @ 1.0MeV	Ids v Vds Ids v Vgs Cgs v Vgs Igs v Vgs	N/A	Ids v Vds Ids v Vgs Cgs v Vgs Igs v Vgs	Ids v Vds Ids v Vgs Cgs v Vgs Igs v Vgs	Ids v Vds Ids v Vgs Cgs v Vgs Igs v Vgs
P04									

Irradiations were conducted with two HFETs per cycle. The HFETs were mounted on the sample stage of the cold-head as shown in Figure 21, and the cold-head mounted on the end of the VDG beam tube. Once the cold-head was firmly in place, a vacuum was drawn on the entire VDG beam tube and equalized with the vacuum in the VDG. In order to achieve the desired 10^{-6} - 10^{-7} Torr, a roughing vacuum pump and a turbo vacuum pump were required. After achieving a suitable, vacuum condition, liquid nitrogen was applied to the cold-head and the sample stage was cooled to 82 - 87 K.

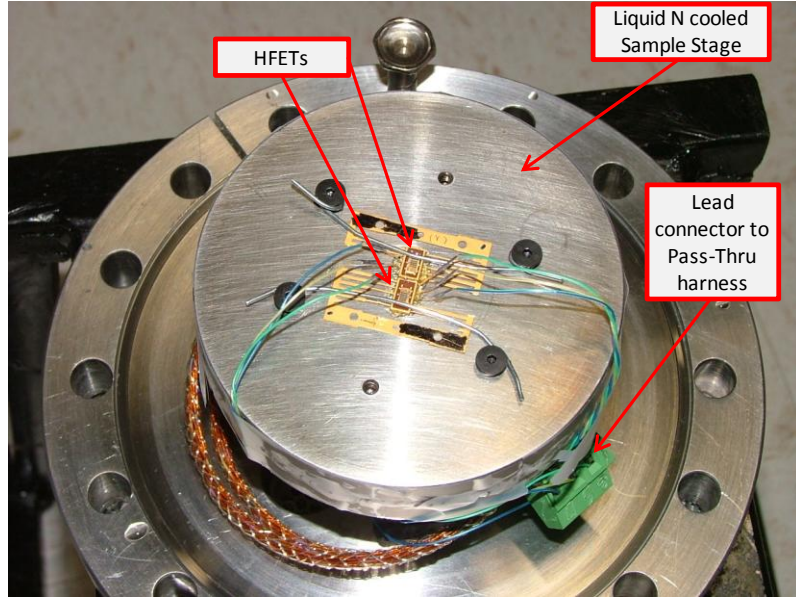


Figure 21. HFET devices mounted on cold-head sample stage. Shown are the electrical connectors and the pass-thru vacuum side wiring harness.

Data collection on the HFETs was accomplished by taking electrical measurements using two Keithley 237 Source Measurement Units (SMU) and a Keithley 590 Capacitance Voltage Analyzer (CVA). Connectivity between these measurement units was achieved using the previously described SCTB, shown in Figure 18. Temperature was monitored using a Lakeshore 331 Temperature Controller with a resistive temperature detector (RTD) inserted in a hole in the sample stage front face or in the cold-finger upper end (pre-characterization and post RT anneal checks) and connected via the pass-thru wiring to the Lakeshore 331 module. Control software included National Instruments' LabView [22], National Instruments Measurement and Automation Explorer [23], and Microsoft Visual Basic [24]. Figure 22 shows the equipment arrangements used for the pre-characterizations/RT anneal checks and the VDG cycles.

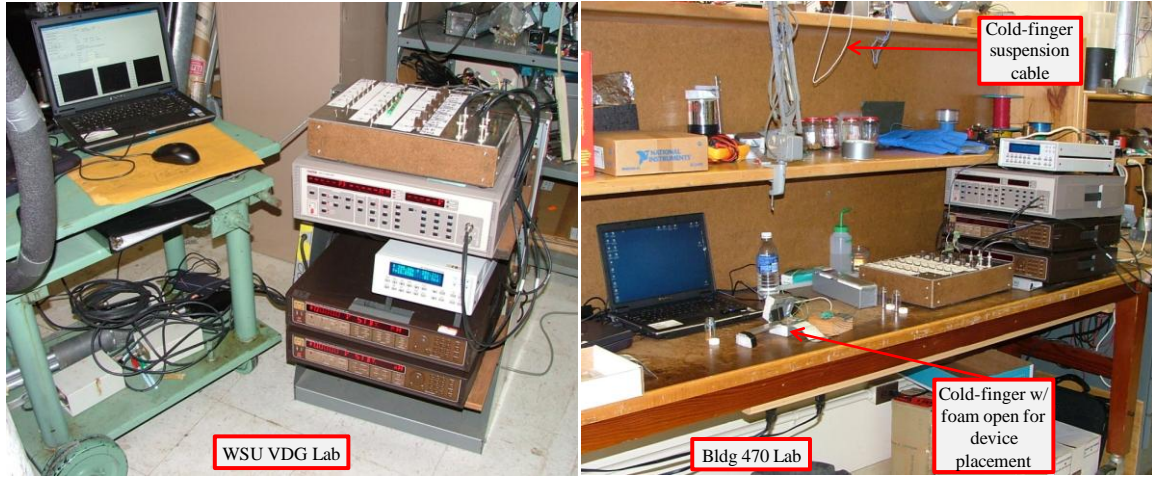


Figure 22. Test and measurement equipment setups: (Left) Wright State VDG lab and (Right) AFIT bldg 470 lab.

Electrical Measurements Taken

A description of the electrical measurements, their significance and explanations of the individual measurement processes are provided in the following paragraphs.

I_{ds} vs. V_{ds}

The transistor current (I_{ds} vs. V_{ds}) was measured as V_{ds} varied from 0 V to 7 V in +0.1 V increments and V_{gs} was varied from -4 V to -2 V in 1 V increments. This data was collected at LNT and RT.

I_{ds} vs. V_{gs} (V_{th} Shift)

Transistor drain currents vs. applied gate voltage, I_{ds} vs. V_{gs} , were measured. The threshold voltage, V_{th} , was determined from these measurements. For these measurements V_{gs} was sourced from -4 V to 0 V, in +0.1 V increments while V_{ds} was sourced at 1.0 V DC and I_{ds} was recorded. This data was collected at LNT and RT.

C_{gs} vs. V_{gs}

Gate to source capacitance, C_{gs} vs. V_{gs} , was measured. A 1MHz, AC, gate voltage was applied while gate bias voltage was varied from -6 V to -1 V in increments of 0.125 V. Drain-to-source voltage was maintained at 0 V. These measurements were taken at LNT and RT and provided another means to observe device threshold voltage shifts post-irradiation and after RT annealing.

I_{gs} vs. V_{gs}

Gate leakage current vs. gate bias voltage, I_{gs} vs. V_{gs} , was measured at 4 K temperature increments from 96 K to 292 K. Gate bias voltage was sourced from -4 V to -0.2 V in 0.2 V increments. During this process, one SMU was dedicated to one HFET with the drain and source leads cross-connected.

Device Grounding Considerations

Throughout this study, special emphasis was placed on insuring the gate, source, and drain leads, of the devices, were maintained grounded to the building's electrical system during all processes that did not require connection to measurement equipment test leads. This was done to prevent damage and device failure. The SCTB design focused heavily on ensuring charge imparted via the electron beam did not build up in or short through the devices mounted on the cold-head sample stage. Additionally, in the lab, the SCTB was always grounded to the electrical system ground through the SMUs and CVA, and the author used a grounding arm strap connected to the SCTB to prevent static discharges from affecting the post-RT anneal checks.

Temperature Control and Monitoring During Data Collection

As mentioned previously, device temperatures were monitored using a Lakeshore 331 Temperature Controller with a resistive temperature detector (RTD). During all measurement regimes, whether pre-characterization, irradiation cycle, or post-RT anneal check, liquid nitrogen was used as the cooling medium. In order to insure continuous, even, and dependable cooling to the devices as well as to ensure a steady, controlled warm-up process to facilitate taking of I_{gs} vs. V_{gs} vs. temperature measurements, a steady flow or supply of liquid nitrogen was required. For cold-head operations on the VDG during irradiation cycles a large, pressurized tank of liquid nitrogen was connected to the cold-head inlet pipe and a simple throttle valve on the outlet pipe controlled the outflow. This allowed precise temperature control and conservation of the nitrogen for multiple, extended irradiation cycles. The nitrogen tank, piping, and cold-head mounted on the VDG beam-pipe chamber can be seen in Figure 23.

Prior to irradiation, the cold-head sample stage (and HFETs) temperature was lowered to around 83-87 K and the throttle valve adjusted until this temperature could be maintained with the minimum flow of liquid nitrogen. Pre-irradiation I_{ds} vs. V_{ds} , I_{ds} vs. V_{gs} , and C_{gs} vs. V_{gs} were taken.

After the irradiation was complete post-irradiation I_{ds} vs. V_{ds} , I_{ds} vs. V_{gs} , and C_{gs} vs. V_{gs} data was taken and the SCTB, laptop, and LabView program were configured to take the I_{gs} vs. V_{gs} measurements as temperature increased from LNT to RT. At this point, the liquid nitrogen supply valve was closed and the throttle valve opened fully, allowing a gradual increase of sample stage temperature from LNT up to about 120 K, which facilitated collecting data.

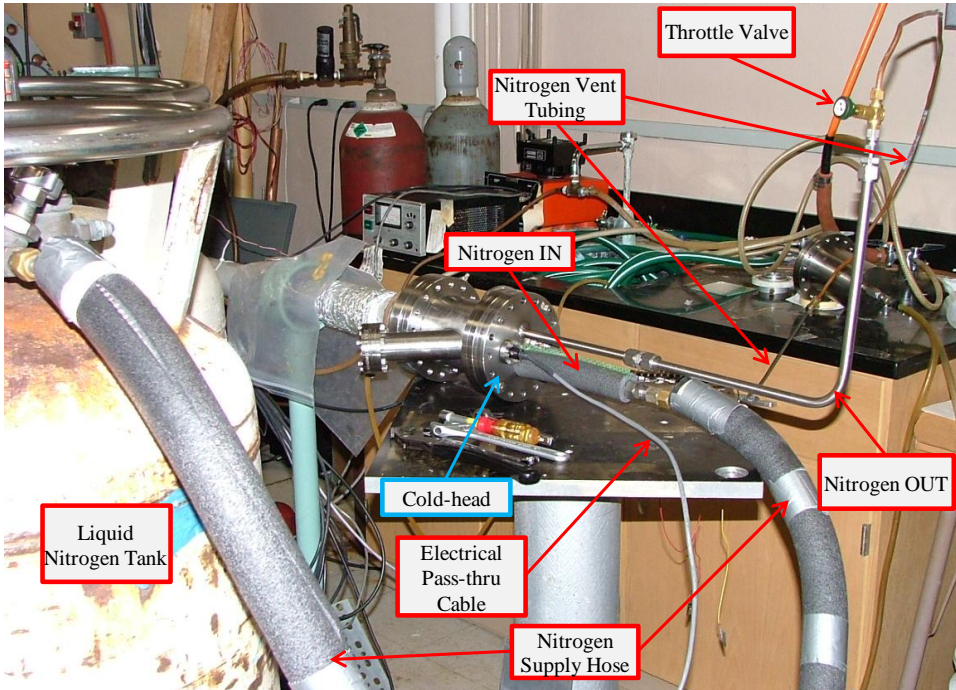


Figure 23. Liquid Nitrogen cooling system for Van de Graaff operations.

Next, the nitrogen supply hose was disconnected from the cold-head inlet pipe and the nitrogen vent piping was removed from the cold-head outlet pipe. This allowed further, gradual warming of the sample stage to around 160 K, as the I_{gs} vs. V_{gs} measurements were taken at every 4 K increase. To maintain a steady temperature increase above the 160 K level, it was necessary to fashion a funnel around the cold-head's inlet pipe connector and apply slow, steady heating to the sample stage using a heat gun. Careful application of the hot air into the cold-head provided steady heating of the sample stage and control over the heating rate.

For the post-irradiation RT anneal measurements a cold-finger was utilized in conjunction with a six-inch inside diameter, large Dewar, maintained half full of liquid

nitrogen, instead of a nitrogen tank and hose. The cold-finger, with two HFETs and the RTD encased in the foam, insulating block at the upper end, was connected to the SCTB via the same cold-head and wiring harness used in the VDG irradiations. This ensured that all electrical connectivity remained the same throughout all measurements. To cool the HFETs the bare, lower portion of the cold-finger was held suspended in the liquid nitrogen volume with the bottom edge of the foam insulation barely touching the surface of the liquid nitrogen. This achieved cooling of the devices on the cold-finger sample stage down to around 83 - 85 K. A detailed view of the cold-finger's construction is shown in Figure 11.

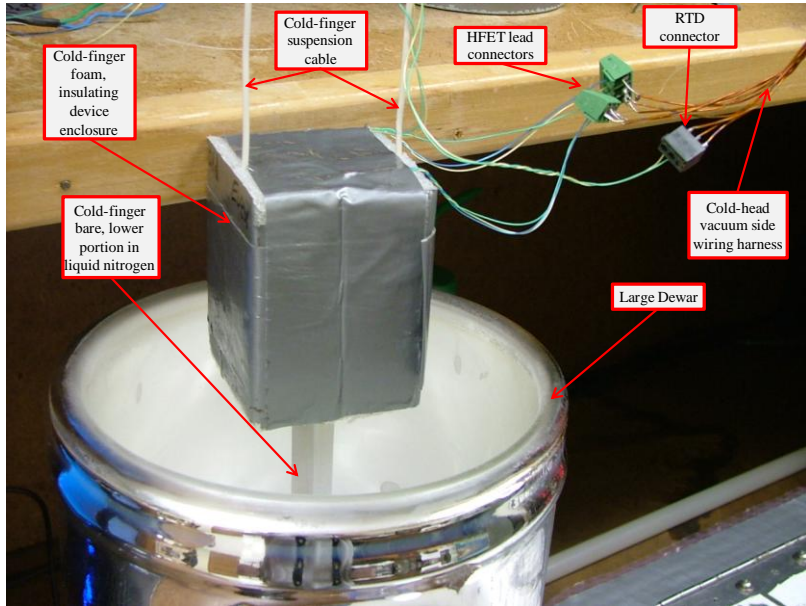


Figure 24. Large Dewar in Bldg 470 lab with cold-finger suspended inside. Connectivity for HFETs and RTD is shown.

V. Experimental Results and Discussion

To present the results for multiple measurements on multiple HFETs not every device will be discussed separately with respect to each measurement. The devices were irradiated in pairs, as shown in Table 9, thus providing verifiable or redundant results. For brevity, where both devices in a pair exhibited very similar behavior throughout this study, only one device or an average of the two devices will be referenced or displayed. The key aspects of these results are the comparison of measurement differences between the unpassivated and passivated devices, the electron energies of 0.5 MeV and 1.0 MeV, the varied electron fluences, and response at LNT vs. RT.

Transistor Drain Current (I_{ds} vs. V_{ds}) and Transistor Current Model Results

HFET drain to source currents increased post-irradiation with near total recovery following post-irradiation RT anneal periods ranging from 24 to 48 days. This overall post-irradiation increase in I_{ds} , at both LNT and RT, is not surprising. The mechanism thought responsible for this increase is the build-up of positive charges in the AlGaN layer during irradiation. The build-up of positive charge is due to the more than three times greater electron mobility of $1000 \text{ cm}^2/\text{V-sec}$, compared to hole mobility of $300 \text{ cm}^2/\text{V-sec}$ [32] in GaN. This study's 27% Al, 73% Ga AlGaN would have similar mobilities for electrons and holes.

Figure 25 shows a plot of the pre- and post-irradiation data for an unpassivated device in the first cycle irradiated by 0.5 MeV electrons at $5 \times 10^{14} \text{ e-/cm}^2$. Note the 75% increase in the drain current saturation level post-irradiation at LNT.

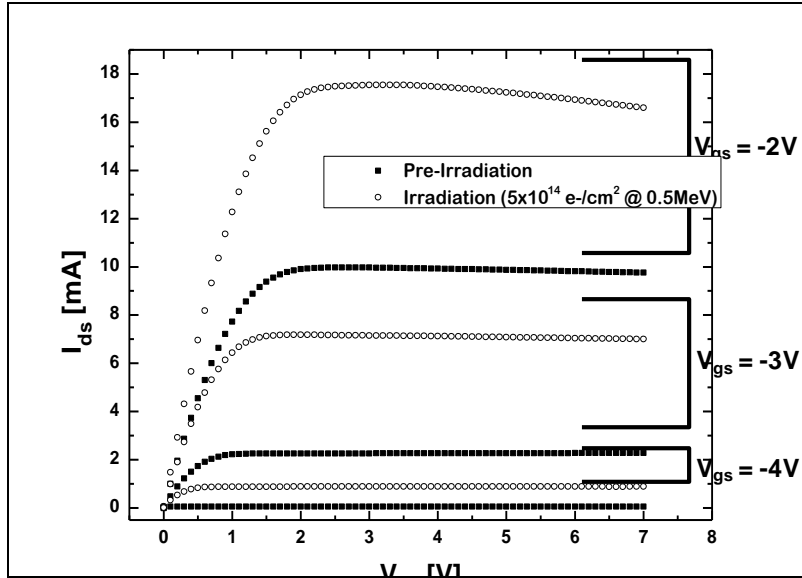


Figure 25. Pre- and Post-Irradiation curves for U01, after 0.5 MeV electron fluence of 5×10^{14} e-/cm², at LNT before any RT anneal periods.

With the more mobile electrons swept out of the AlGaN to the gate by the intrinsic piezoelectric field, the remaining holes provide positive charge resulting in an increased carrier density in the channel and an increased transistor current at the same gate and drain voltages. The positively charged holes immobile in the AlGaN layer increase the field and attract electrons from the n-type GaN to the channel, thereby increasing carrier concentration (n_s) and drain current.

Increasing incident electron energy resulted in an overall lower percent increase in drain current. A 49% increase in drain current occurred in the first two devices irradiated with a fluence of 5×10^{14} e-/cm² 0.5 MeV electrons, with only a 20% increase for those irradiated with 1.0 MeV electrons at the same fluence.

Post-irradiation changes to drain current saturation levels, for $V_{gs} = -2$ V, were less pronounced at RT in the unpassivated HFETs. This difference at LNT vs. RT

resulted from decreased mobility due to increased defect scattering in the 2DEG carriers as temperature increased. The holes created in the AlGaN during the electron irradiation increase in thermal energy as temperature increases toward RT and some migrate toward the AlGaN/GaN interface. Once at the interface, the holes can recombine or transform into interface traps that result in reduced channel mobility. This contributed to the characteristic post-irradiation, lower percentage change in I_{ds} at RT compared with LNT for all devices. This behavior is can be seen in the LNT vs. RT plots in Figure 27 and in comparing Figure 29 to Figure 30. A summary of this study's results including these changes is provided in Table 13.

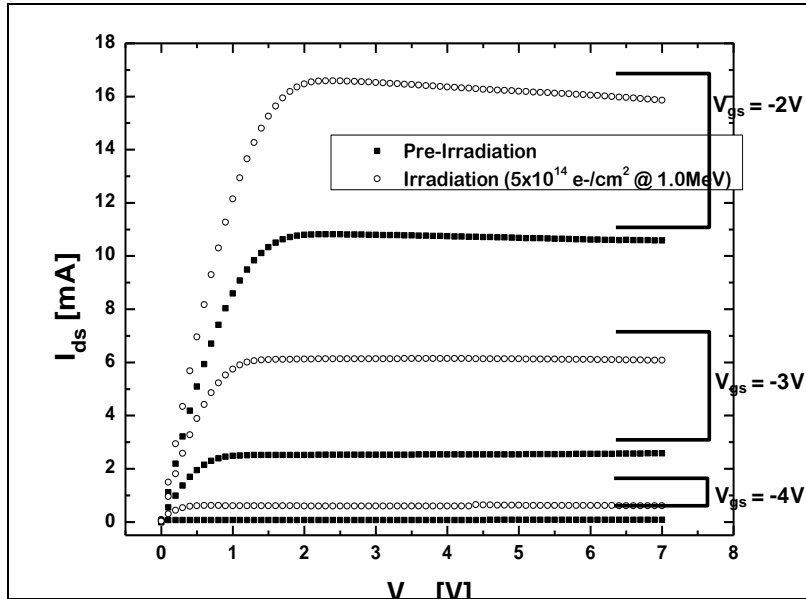


Figure 26. Pre- and Post-Irradiation curves for U03, after a 1.0 MeV electron fluence of 5×10^{14} e-/cm 2 , at LNT before any RT anneal periods.

Figure 26 shows average changes in an unpassivated device in the second cycle irradiated by 1.0 MeV electrons to the same fluence at the first cycle. The increased

incident electron energy resulted in a smaller post-irradiation increase of 53%. This agrees well with the TIGER [4] simulations that suggested that higher energy electrons deposit less of their energy in the shallow AlGaN or thicker underlying GaN layer.

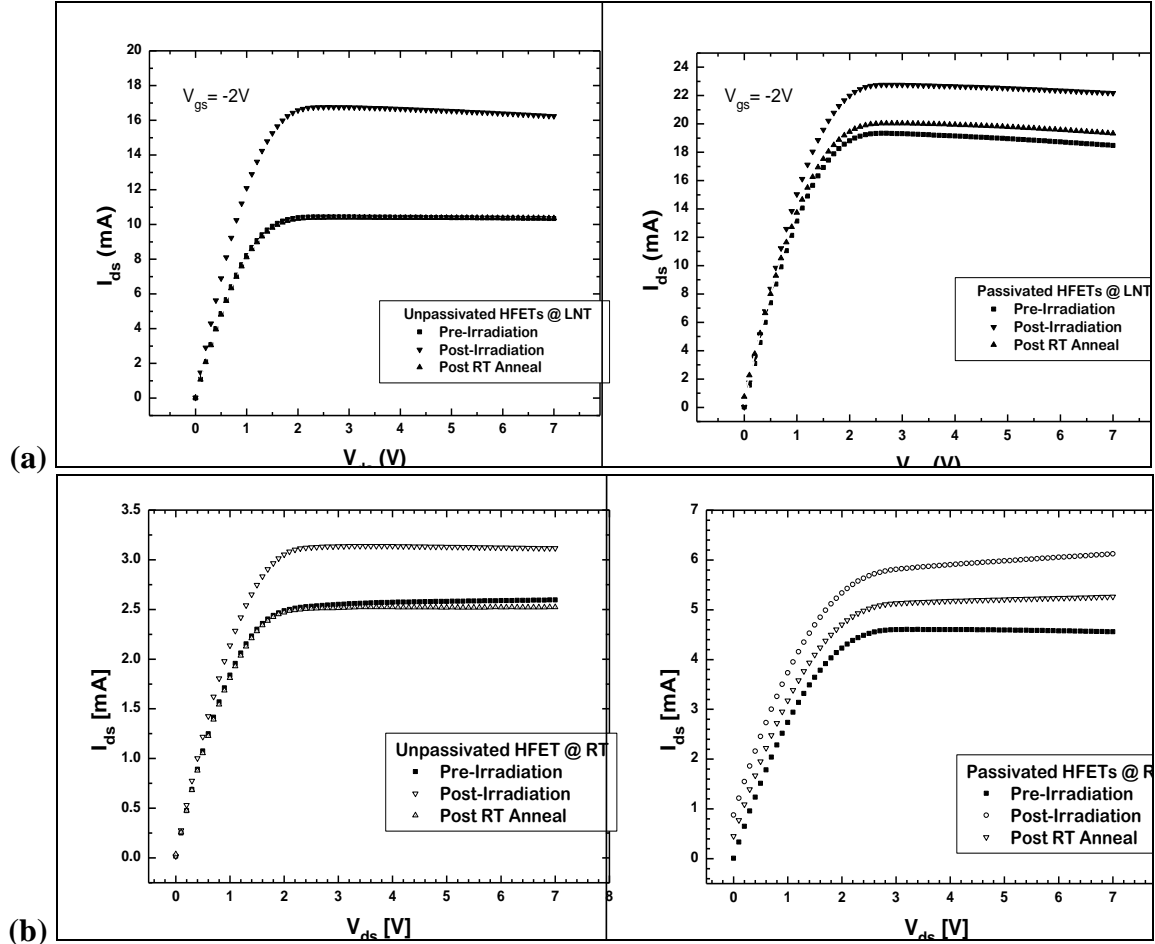


Figure 27. Average drain current values at $V_{gs} = -2$ V; pre-irradiation, post-irradiation, and post RT anneal showing LNT curves in (a) and RT curves in (b) with the average of the unpassivated HFETs on the left and passivated HFETs on the right.

Figure 27 presents pre-irradiation, post-irradiation, and post RT-anneal curves of I_{ds} vs. V_{ds} at LNT and RT. These plots are averages for all unpassivated and for all passivated HFETs. Clearly shown are the higher pre-irradiation drain currents at LNT

compared to RT for all devices and higher pre-irradiation drain currents for passivated compared to unpassivated devices. Also visible in Figure 27 and Table 13 are the lower average post-irradiation changes in drain current saturation levels for passivated HFETs. Further, these averaged curves indicate more rapid recovery for unpassivated than for passivated devices after similar RT anneal periods.

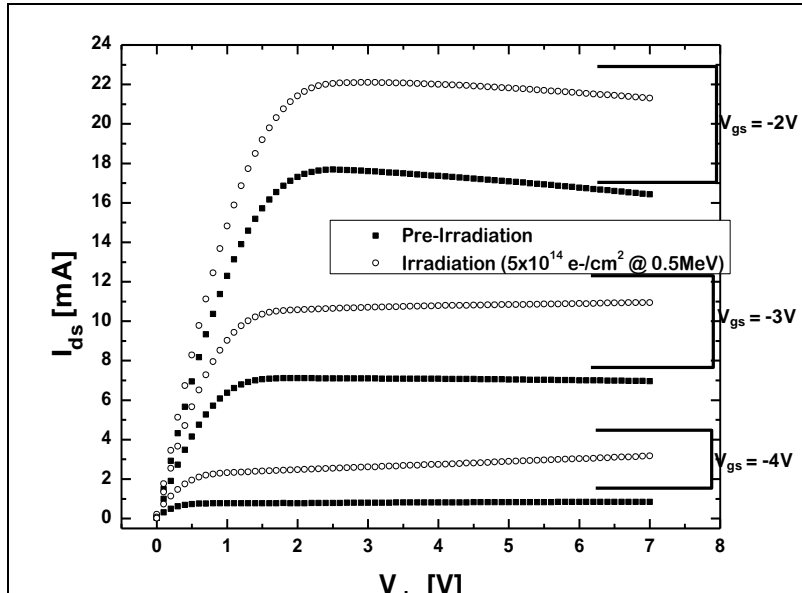


Figure 28. Plot of pre- and post-irradiation data for passivated HFET P01, after a 0.5 MeV electron fluence of 5×10^{14} e-/cm², at LNT before any RT anneal periods.

Detailed post-irradiation I_{ds} saturation level comparisons, for passivated and unpassivated devices, can be seen in comparing Figure 25 and Figure 28. The smaller post-irradiation change, roughly 26% for the first passivated devices irradiated, presented in Figure 28, is evident for the same fluence and electron energy at LNT with $V_{gs} = -2$ V. The passivated devices also showed a similar small, 23%, post-irradiation increase at RT.

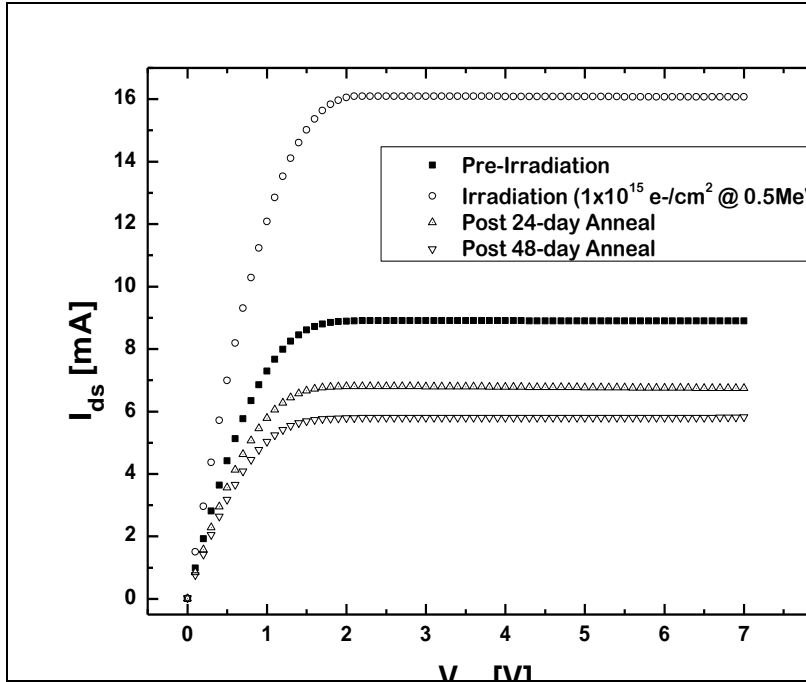


Figure 29. Drain current vs. drain voltage at LNT and $V_{gs} = -2$ V for U10; irradiated to 1×10^{15} e-/cm² @ 0.5 MeV.

Unpassivated devices irradiated to 1×10^{15} e-/cm² and higher, with 0.5 MeV electrons, showed overall increased post-irradiation drain current saturation levels at LNT and RT. The LNT curves for U10, irradiated to 1×10^{15} e-/cm² with 0.5 MeV, can be seen in Figure 29. The RT transistor current curves for U10 are shown in Figure 30. Post-irradiation saturation level increased by 29% at RT, compared to an 80% increase at LNT.

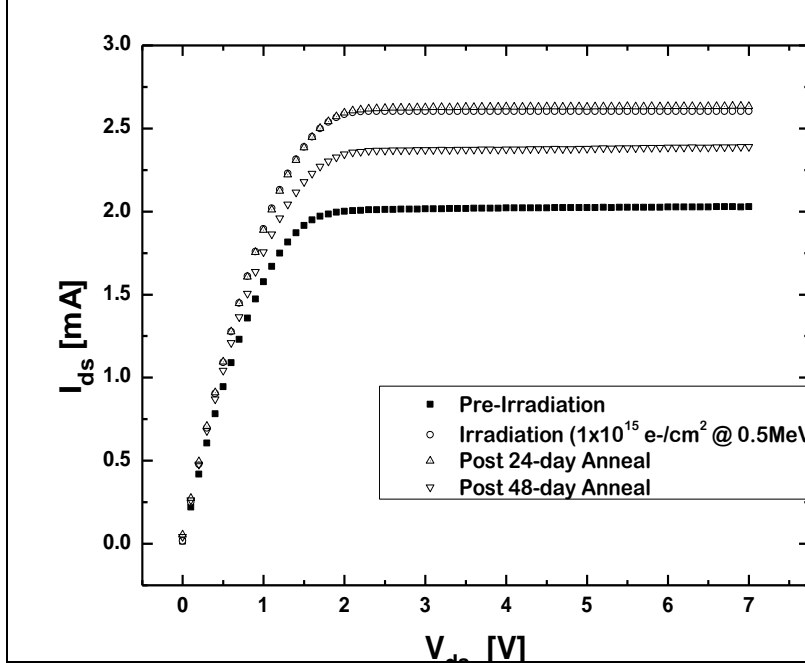


Figure 30. Drain current vs. drain-to-source voltage at RT and $V_{gs} = -2$ V for U10; irradiated to 1×10^{15} e/cm² @ 0.5 MeV.

This study attempted to show a direct relationship between the electron-hole pair formation in the AlGaN, the V_{th} shifts, and the increased I_{ds} . To do this, it was necessary to use Equations(12), (13), Figure 4, and information provided in [7]. Ignoring the small radiative portion of the energy loss for 0.5 MeV electrons in AlGaN; the collisional stopping power for 0.5 MeV electrons is approximately 1.45 MeV-cm²/g. Only about 10 eV-cm²/g of that result in NIEL, therefore effects due to ionizing energy loss (IEL) will only be addressed here. Equation (14) provides the total energy deposited by the electrons in the AlGaN layer using [7].

$$E_T = \frac{dE}{dx} \rho \varphi dA \quad (14)$$

This equation, in conjunction with data provided in [7], indicates that for electron fluence (ϕ) of 5×10^{14} e-/cm², the total energy deposited (E_T) in the AlGaN layer of one of the HFETs tested was in excess of 1.075×10^{12} eV. With AlGaN density, ρ , of 5.33 g/cm³, AlGaN layer thickness, d , of 25 nm, gate area, A , of 5×10^{-5} cm², and considering AlGaN electron-hole production energy is 10 eV, this suggests there may be as many as 1.075×10^{15} cm⁻³ electron-hole pairs produced in the AlGaN layer during irradiation at LNT. If even one percent of the holes are not swept out and do not recombine, then sufficient positive charge may remain in the AlGaN layer to provide for the increase in carrier concentration and ultimately transistor current [5][7].

Results for I_{ds} vs. V_{gs} Measurements

Transistor currents with respect to varying gate voltage with drain to source voltage held constant at +1 V were measured to provide indication of HFET threshold voltage (V_{th}) shifts due to the electron irradiation. The changes in V_{th} were evaluated using the linear extrapolation method as described in chapter 4.

Figure 31 and Figure 32 depict the I_{ds} vs. V_{gs} curves, pre- and post-irradiation and after a RT anneal period for both unpassivated and passivated devices. In Figure 31 the V_{th} increase at LNT shows almost complete recovery after a 48-day RT anneal with RT measurements showing smaller shifts with similar recovery behavior. The observed shifts in V_{th} are attributed to trapped positive charges in the AlGaN layer. These trapped positive charges result from incident IEL (electron-hole pair formation) within the AlGaN layer. The effects of these positive charges decrease after RT anneal.

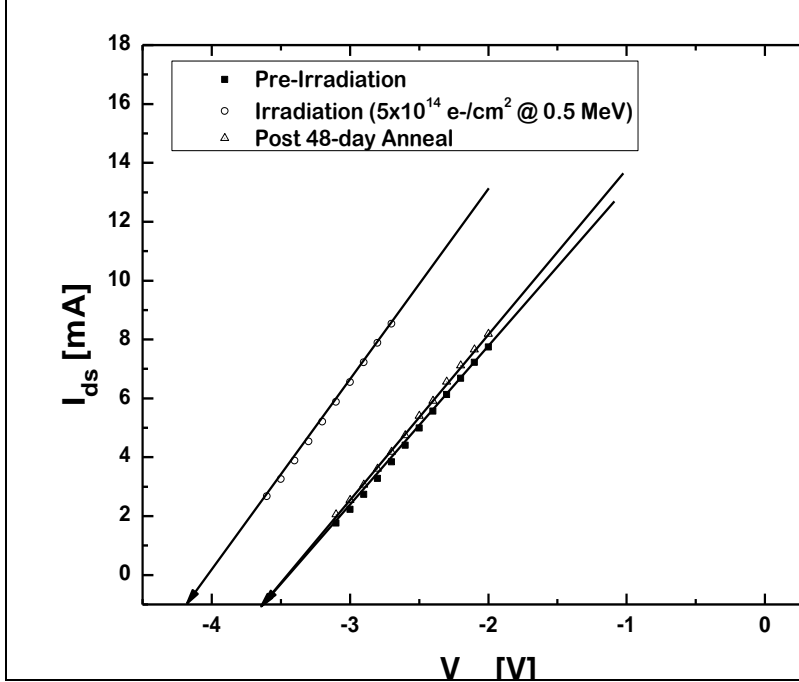


Figure 31. Plot of drain current vs. gate voltage, for U01, highlighting the linear extrapolation method for determining the post-irradiation threshold voltage shift [40]. Note, the complete recovery post 48-day RT anneal.

In Figure 32, the complete recovery included some temporary super recovery. This was slightly greater after 24 days of RT annealing, but drifted back toward pre-irradiation values by day 48. The super recovery may be attributable to the positive charges (that produced the observed V_{th} shifts) migrating to the interface where they are transformed or neutralized. This time and temperature dependent decrease in the IEL-produced positive charge in the AlGaN layer, coupled with some as yet unknown temporary effect(s) that either reduces carrier concentration or decreases channel mobility may be the mechanism causing this temporary super recovery.

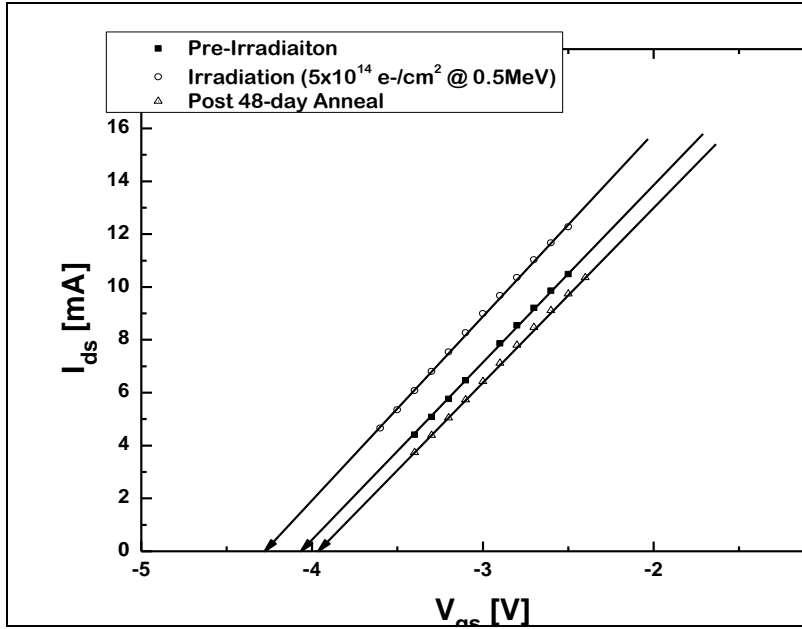


Figure 32. Plot of drain current vs. gate voltage, for passivated HFET P01, highlighting the linear extrapolation method for determining the post-irradiation threshold voltage shift. Note, the slight super recovery post 48-day RT anneal.

Threshold voltage shifts were slightly less pronounced at RT than at LNT. This was attributed to the same mechanisms that produce lower drain currents at RT. In addition, the incident electron energy had little effect on the magnitude of the V_{th} shifts. However, the unpassivated devices irradiated with 1.0 MeV electrons showed a slower recovery; possibly indicating more NIEL defects had occurred.

Comparison of Carrier Concentration Change Indicators

The electron irradiation induced changes in the HFETs' drain to source current further reinforce the post-irradiation -0.4 V to -0.6 V threshold voltage shifts seen in this study. Equation (12) suggests changes in carrier concentration may result in enough carriers being produced to significantly increase I_{ds} post-irradiation and continue until the charged defect centers producing the shift anneal away. Equation (15) is the result of

manipulating Equation (10) to isolate the n_s term and relate changes in it to the only unknown term on the right hand side, I_{ds} . With q known, values for v_{e^-} were calculated using Equation (16)[53] and values of μ_{e^-} from Hall measurements done by [56]. In Equation (16) the electric field in the channel (drain-to-source) was obtained by multiplying W , the gate width or channel length, by the applied drain-to-source voltage of +6 V. I_{ds} and V_{th} were obtained from experimental data. W is known to be 50 μm . Equation (12) is redisplayed below for comparison.

$$\Delta n_s = \frac{\varepsilon(x)}{qd} - \Delta V_{th} \quad (12)$$

$$\Delta n_s = \frac{\Delta I_{ds}}{qWv_{e^-}} \quad (15)$$

$$v_{e^-} = \mu_{e^-} \varepsilon \quad (16)$$

In Table 10, the results of calculating the change in carrier concentration, n_s , based on the observed threshold voltage shifts is compared to the change in carriers calculated from pre- to post-irradiation drain current values. Both I_{ds} at $V_{gs} = -2$ V and V_{th} are measured at LNT.

Table 10. Results of calculating carrier concentration changes by drain current model using threshold voltage shift and by I_{ds} changes pre- to post-irradiation.

	Ids Data @ LN				Vth Data @ LN		Difference	% Difference
	Pre Ids (Sat) [Amp]	Post Ids (Sat) [Amp]	Δ Ids [Amp]	Δn_s (Ids) [e-]	Δ Vth [V]	Δn_s (Δ Vth) [e-]	Δn_s (Ids) - Δn_s (Δ Vth) [e-]	Difference/ Δn_s (Ids) [%]
U01	9.97E-03	1.75E-02	7.53E-03	1.40E+12	-0.6	1.1806E+12	2.18E+11	15.61%
U03	1.08E-02	1.66E-02	5.80E-03	1.08E+12	-0.45	8.8546E+11	1.92E+11	17.83%
U10	8.91E-03	1.61E-02	7.19E-03	1.34E+12	-0.55	1.0822E+12	2.54E+11	18.99%
P01	1.76E-02	2.21E-02	4.50E-03	8.36E+11	-0.1	1.9677E+11	6.39E+11	76.46%
P04	2.04E-02	2.29E-02	2.50E-03	4.64E+11	-0.2	3.9354E+11	7.09E+10	15.27%

In Table 10 the far right column contains the percent difference obtained from dividing the difference in pre- to post-irradiation changes in $n_s(I_{ds})$ (calculated using Equation (15)) and $n_s(V_{th})$ (calculated using Equation(12)), by the $n_s(I_{ds})$. The difference between changes in $n_s(I_{ds})$ and in $n_s(V_{th})$ is less than 20% in all but one of the cycles evaluated. This assumes that carrier drift velocities are similar to those calculated using data from [56] and in [54][55]. These results complement the observed shift in threshold voltage discussed in the following subsections.

Overall, these results, using electrons, differ significantly from some previous AlGaN/GaN research studying transistor currents, in which protons were used. White[14][17] and Luo[15] and others noted decreased post-irradiation I_{ds} saturation levels at RT, after using protons at energies of 1.8 MeV to 40 MeV.

Hu[16] attributed the observed decrease in transistor current at RT to charged defects outside the 2DEG reducing carrier mobility in the 2DEG through Coulombic interactions, while charged defects formed inside the 2DEG are suspected of trapping carriers [16]. As the positively charged holes migrate and recombine or are neutralized at RT, the observed effects of these non-annealing, charged defects become more noticeable. Additionally, this fits with the observation that higher electron energies resulted in a lesser increase in drain current for the same fluence. In [5], using 1 MeV (eq) neutrons, a similar decrease at RT was noted. A more detailed comparison between these results using electrons and results obtained by [5] using reactor spectrum neutrons at 1 MeV (eq) is provided at the end of this chapter.

Results for C_{gs} vs. V_{gs} Measurements

The shifts in the gate to channel capacitance vs. gate voltage curves measured pre-irradiation, post-irradiation, and post RT anneal provide supporting evidence to the shift in threshold voltage obtained in the previous subsection. The slight vertical changes in the actual C_{gs} values from the pre- and post-irradiation measurements to the RT anneal measurements are attributed to the difference in device capacitance in a vacuum vs. exposed to the atmosphere. The pre- and post-irradiation measurements were always taken with the HFETs mounted on the cold-head inside the vacuum chamber on the beam end of the VDG with vacuum levels typically around 2×10^{-6} Torr. For the post-RT anneal checks, both the LNT and RT measurements were taken with the HFETs mounted on the cold-finger and subjected to normal atmosphere and pressure. Exposure of the AlGaN material to the atmosphere may have allowed the exchange of nitrogen, oxygen, hydrogen, or moisture between the AlGaN layer and the atmosphere. Additionally, even with the Si_3N_4 passivation layer, the slight vertical shift of the post RT anneal capacitance curves was apparent. Curves in Figure 33 and Figure 34 have been vertically normalized to simplify comparison of threshold voltage shifts.

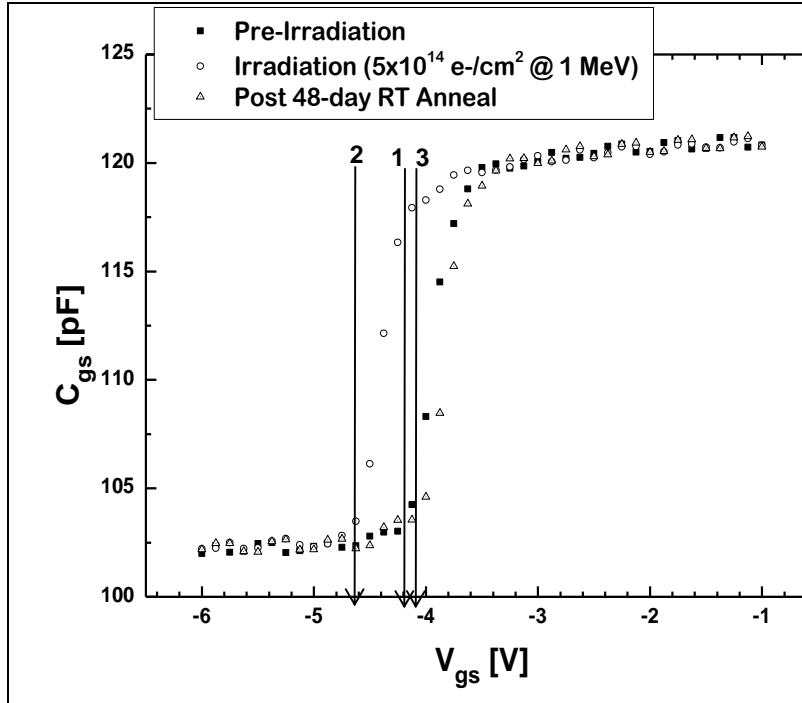


Figure 33. Gate capacitance vs. gate voltage curves for unpassivated HFET at LNT. The post-irradiation V_{th} shift (arrow #2) and the slight super-recovery (arrow #3) toward pre-irradiation values (arrow #1) are clearly visible. Curves are vertically normalized for comparison.

For the unpassivated devices, the negative post-irradiation shift in V_{th} averaged 15% at LNT, roughly -0.5 V, as seen in Figure 33 for the second set of devices. Once the devices had reached RT, the V_{th} shift averaged negative 5%, with some devices displaying slight super-recovery by day 24, and then drifting to nearly pre-irradiation V_{th} values by day 48. The observed threshold voltage shifts in the gate capacitance curves typically matched the threshold voltage shifts linearly extrapolated from the I_{ds} vs. V_{gs} curves to within five percent or less. The I_{ds} vs. V_{gs} and the C_{gs} vs. V_{gs} measurements produced mutually supporting evidence of post-irradiation negative threshold voltage shifts.

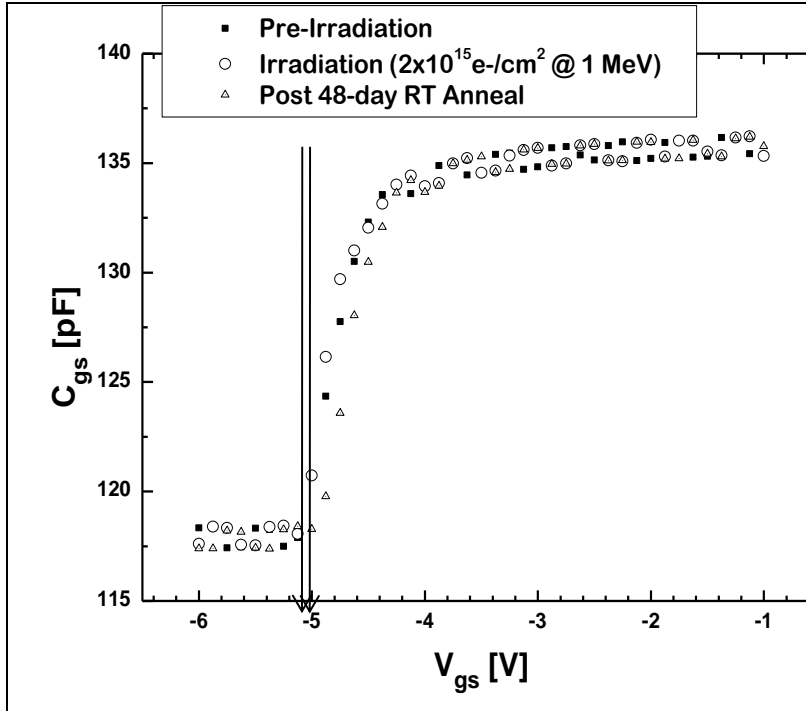


Figure 34. C_{gs} vs. V_{gs} at LNT, for passivated device P04. Note the negligible post-irradiation shift in V_{th} . Curves are vertically normalized for comparison.

In Figure 34, for the passivated devices, there was negligible shift in V_{th} , pre- to post-irradiation at LNT. These curves, as with previous capacitance plots, were normalized for comparison. Measurements on passivated devices at RT showed small shifts in V_{th} that were comparable to shifts indicated by the I_{ds} vs. V_{gs} data.

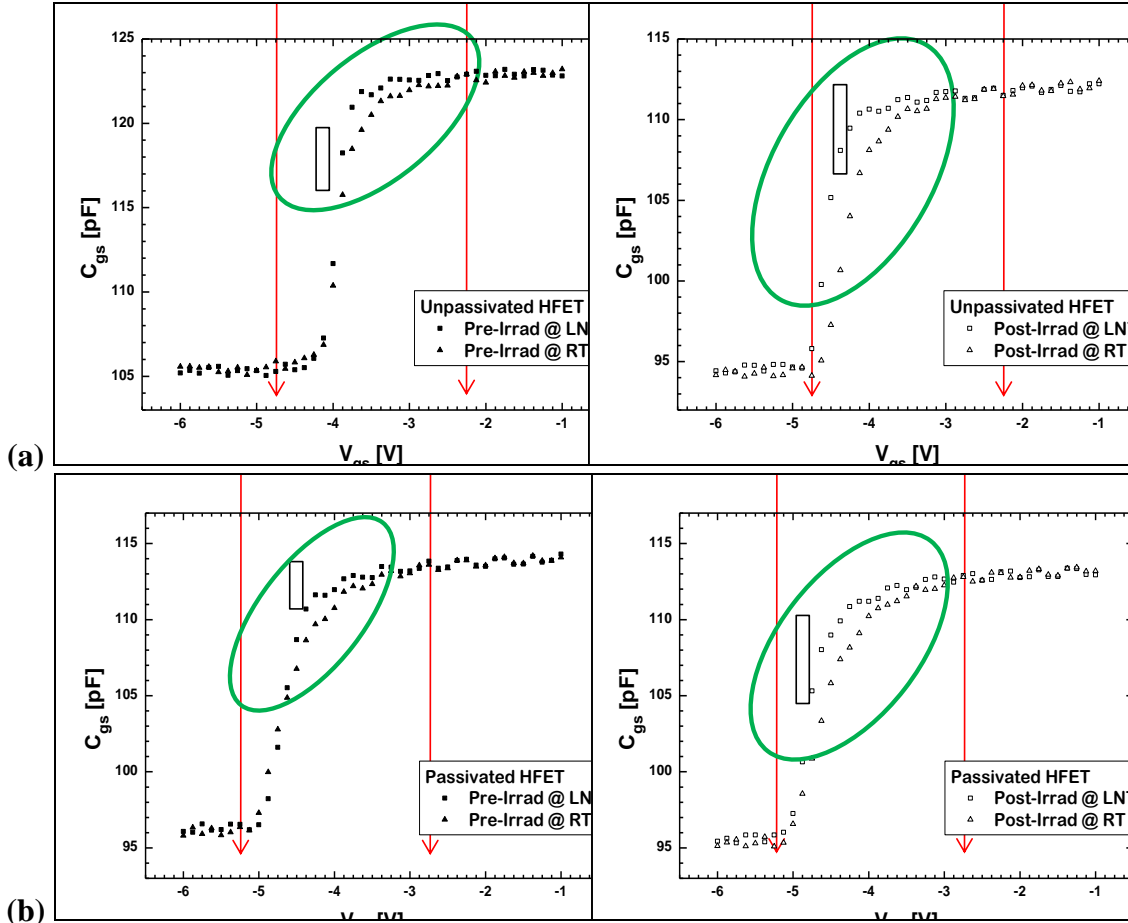


Figure 35. The effects of interface trap formation is seen in the slope-flattening from LNT to RT on the post-irradiation capacitance curves for (a) an unpassivated HFET and (b) a passivated HFET.

The circled regions in the four charts of Figure 35 provide examples of the slope-flattening effect between LNT and RT curves due to the existence of interface traps. These plots indicate these interface trap effects occurred in both passivated and unpassivated devices. This suggests passivation has negligible impact on interface trap manifestation. Further, it was observed that the separation of the LNT and RT curves, indicative of interface trap formation, was slightly greater in devices subjected to higher energy electrons. These interface traps were observed by [49] during their study using

ions. The origin of the increase in observed interface traps is attributed to the transformation of the IEL-formed positive charges that migrates to the AlGaN/GaN interface at increased temperatures. In Table 11, results of a qualitative analysis of interface trap concentrations are presented. The average relative difference (ARD) between the LNT and RT current values for a specific range of V_{gs} values was calculated and used as a comparative number between pre-irradiation and post-irradiation slope-flattening in the HFETs studied. These ARD values are presented in the first and second data rows of Table 11.

Table 11: Qualitative summary of interface trap concentrations.

$\{\sum [(LNT-RT)/RT]\}/N$	Qualitative Comparison of Relative Difference Values for Interface Trap Formation									
	U01	U03	U05	U10	Unpass. Avg	P01	P02	P03	P04	Pass. Avg
Pre-Irrad [F]	7.14E-03	1.26E-02	8.19E-03	8.70E-03	9.16E-03	7.76E-03	5.58E-03	7.78E-03	8.01E-03	7.28E-03
Post-Irrad [F]	1.60E-02	2.07E-02	1.25E-02	2.93E-02	1.97E-02	8.82E-03	1.08E-02	1.32E-02	1.14E-02	1.11E-02
% Increase [%]	124.4%	64.5%	53.2%	237.1%	114.6%	13.7%	92.8%	70.1%	42.5%	51.8%

Referring to Figure 35, the vertical rectangles superimposed on each chart encompass one capacitance measurement ($C_{LNT(i)}$ and $C_{RT(i)}$) from each curve (LNT and RT). These capacitance values correspond to the same V_{gs} value on the x-axis. Using a range of $N = 21$ consecutive V_{gs} values spanning the range in which the slope-flattening behavior is noted, Equation (17)[57] was used to determine the actual pre- and post-irradiation values listed in Table 11.

$$ARD = \frac{\sum_{i=1}^N \frac{Abs(C_{LNT(i)} - C_{RT(i)})}{C_{RT(i)}}}{N} \quad (17)$$

$$\% \text{ Increase} = \frac{(ARD_{pre} - ARD_{post})}{ARD_{post}} \quad (18)$$

The percent increases shown in the bottom row of Table 11 were obtained using Equation (18). This method for creating a numerical parameter defining the visually observable slope-flattening does not address the actual number of interface traps present; it is intended only as a comparison to illustrate the post-irradiation increase in interface trap concentrations.

Results for I_{gs} vs. V_{gs} at Varying Temperatures

To evaluate the temperature dependent nature of the electron irradiation induced effects on HFET gate leakage current, gate current vs. bias voltage measurements (described in chapter 4) were taken every 4 K during a controlled temperature increase from 96 K to 292 K. Figure 36 presents the increase in gate leakage current as the magnitude of the gate bias is increased at 100 K and 212 K.

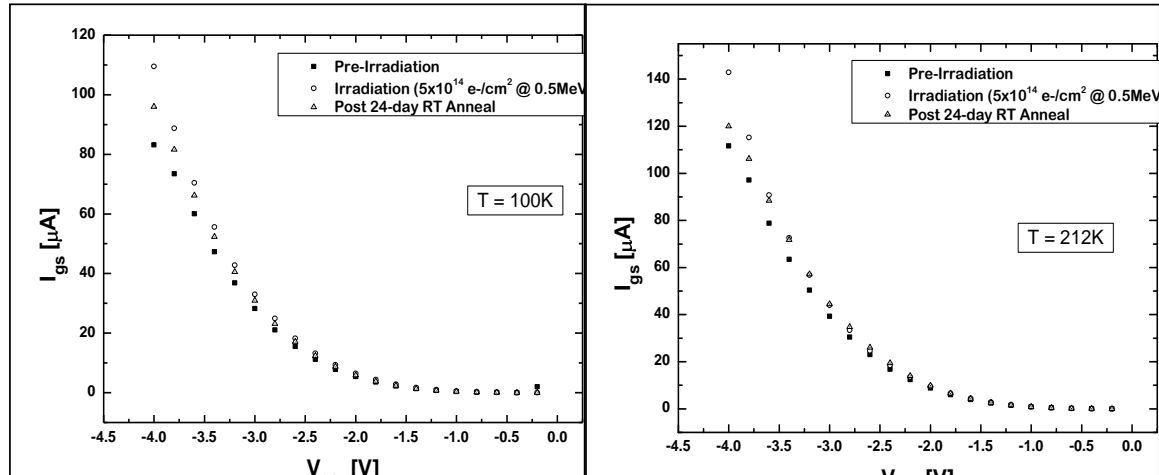


Figure 36. Gate leakage current vs. gate voltage for unpassivated device U01 at 100 K and 212K. Note the higher values at higher temperature.

Figure 37 presents pre-irradiation to post RT anneal gate leakage currents for an unpassivated HFET. All unpassivated devices showed near normal gate leakage currents after varying lengths of post-irradiation RT annealing.

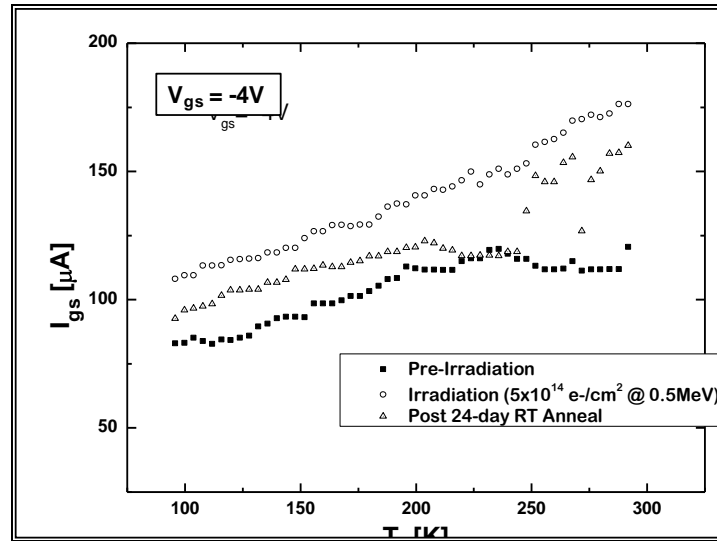


Figure 37. Gate leakage current vs. temperature at $V_{gs} = -4$ V, for an unpassivated HFET.

The electron irradiation induced effects on the passivated HFETs is shown in Figure 38. Note the characteristically higher pre-irradiation gate leakage currents for the passivated devices. Post-irradiation, the passivated HFETs displayed a greater percent increase in gate leakage current than did unpassivated devices irradiated to the same fluence and electron energy, shown by comparing Figure 37 and Figure 38. In addition, there is no substantial recovery post RT anneal even after 48 days for passivated devices unlike for unpassivated devices. The observed recovery of all unpassivated devices compared to the lack of recover for passivated devices is presented in the pre-irradiation, post-irradiation, and post RT anneal curves in the plots in Figure 39.

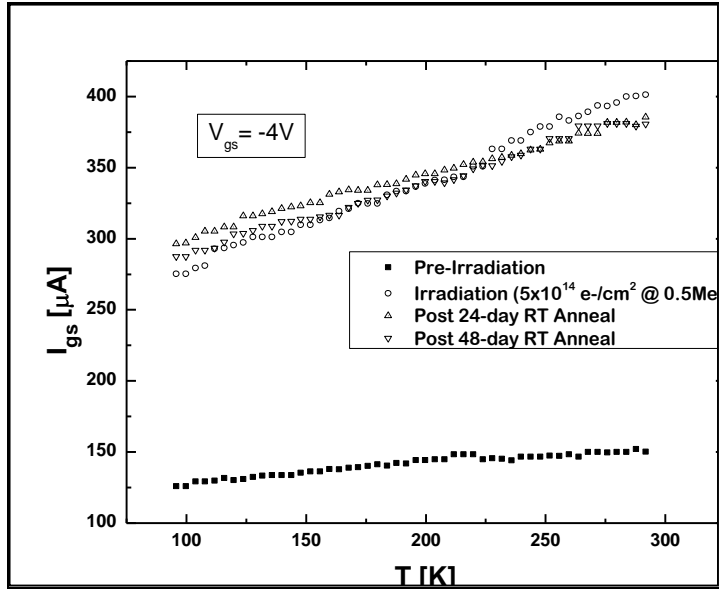


Figure 38. Gate leakage current vs. temperature curves for a passivated HFET at $V_{gs} = -4$ V. Passivated devices showed little recovery after RT anneal.

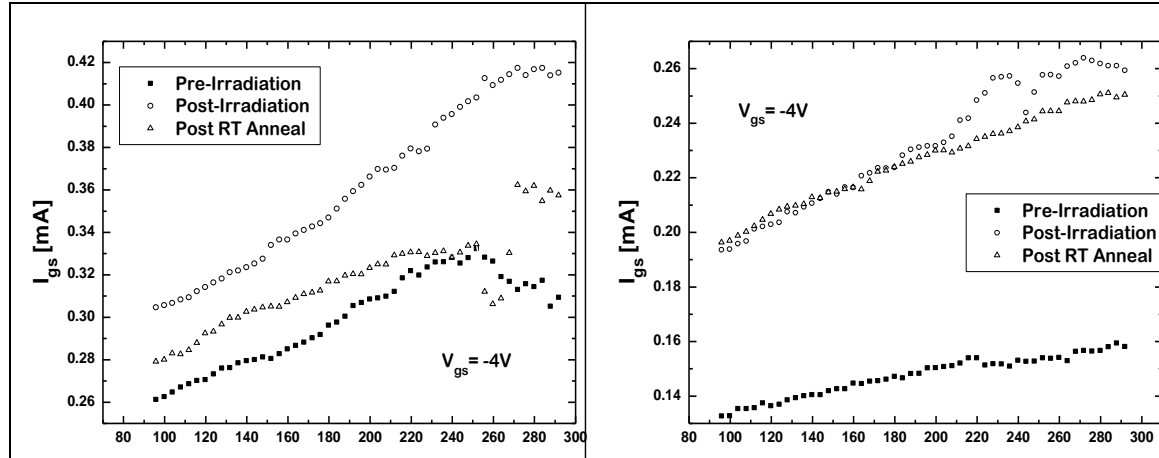


Figure 39. Averaged gate leakage current curves for unpassivated (left) and passivated (right) HFETs. Post RT anneal recovery is apparent for the unpassivated devices while passivated HFETs show no tendency to recover after RT anneal.

The difference in post RT anneal behavior between unpassivated and passivated HFETs, shown in Figure 39, is attributed to the Si_3N_4 passivation layer trapping impurities in the AlGaN layer. The most likely potential impurity is oxygen. The

impurities trapped in the AlGaN by the Si_3N_4 passivation may complex with electron radiation induced defects. This complexing increases the number of traps available for electron tunneling thereby explaining the elevated gate leakage currents observed in the passivated devices.

Further, Si_3N_4 may interact with electron radiation to produce donor-like defects in the passivation layer. If these defects migrate into the AlGaN layer, they may have similar effects on device operation as donor doping of the AlGaN. This could account for the TAT model fitting results (in the next section) that indicate an increase in N_D (donor concentration in the AlGaN layer) as well as N_t (trap density in the AlGaN layer) is responsible for the increased gate leakage currents in the passivated HFETs studied.

Results for Trap Assisted Tunneling (TAT) Model

The results of fitting the Trap-Assisted Tunneling [36] model to experimental data are presented and discussed below. Table 12 shows the consolidated results of the fittings. The upper section in Table 12 shows the values of the four parameters obtained using the fitting algorithm as described in chapter 3. The lower section provides the quantitative changes to parameter fits for pre- to post-irradiation data and the percentage changes after irradiation.

Table 12. Results for Trap Assisted Tunneling Model. Upper section is Pre- and Post-Irradiation values and the lower section is the absolute and percent changes.

Pre- and Post-Irradiation Values for T.A.T. Model Parameters											
	Units	U01		U03		U10		P01		P04	
	Units	Pre	Post								
ND fit	#/cm ³	3.52E+24	3.54E+24	3.28E+24	4.54E+24	3.27E+24	3.24E+24	1.73E+24	3.43E+24	4.40E+24	5.40E+24
Nt fit	#/cm ³	1.34E+21	1.80E+21	1.80E+21	2.38E+21	1.37E+21	2.46E+21	8.90E+21	3.60E+21	8.50E+21	3.50E+21
ϕ(t) fit	eV	0.7414	0.7469	0.7100	0.7503	0.6860	0.7020	0.7787	0.7353	0.9240	0.8227
ϕ(bo) fit	eV	1.1580	1.1617	1.1573	1.0647	0.9963	1.0609	1.0920	1.0980	1.2600	1.3800
R-RMSE	Amps	2.43E-06	3.44E-06	1.68E-05	6.81E-06	8.24E-06	8.66E-06	1.08E-05	9.55E-06	9.96E-06	1.27E-05
I_{gs} (Avg)	Amps	1.01E-04	1.30E-04	1.53E-04	3.35E-04	2.21E-04	3.01E-04	1.39E-04	3.24E-04	1.29E-04	1.69E-04
R-RMSE % of I_{gs} (Avg)		2.41%	2.64%	11.01%	2.03%	3.72%	2.88%	7.77%	2.95%	7.70%	7.47%

Pre- to Post-Irradiation Changes and Percentages for T.A.T Model Parameters											
	Units	Δ ±	%Δ ±	Δ ±	%Δ ±						
ND fit	#/cm ³	2.15E+22	0.61%	1.26E+24	38.46%	-2.5E+22	-0.77%	1.7E+24	97.81%	1E+24	22.73%
Nt fit	#/cm ³	4.6E+20	34.33%	5.8E+20	32.22%	1.09E+21	79.59%	-5.3E+21	-59.55%	-5E+21	-58.82%
ϕ(t) fit	eV	0.00551	0.74%	0.04032	5.68%	0.016	2.33%	-0.04333	-5.56%	-0.10133	-10.97%
ϕ(bo) fit	eV	0.0037	0.32%	-0.09263	-8.00%	0.06466	6.49%	0.00597	0.55%	0.12	9.52%

The model was applied to the HFETs' I_{gs} vs. T at $V_{gs} = -4$ V and I_{gs} vs. V_{gs} at $T = 100$ K data. Twenty data points were used to evaluate each curve to evenly weight the temperature and voltage dependent data. For a detailed description of the TAT model, the process for optimization of the parameter values, and previous fit results using it refer to [5] sections 3.5, 4.4, and 5.3, respectively.

All devices achieved a better than 10% R-RMSE with several devices achieving a better than 4% R-RMSE. The percentages in the last row of the upper section of Table 12 were obtained by taking the Relative Root Mean Square Error (R-RMSE) for the device's best fit to the model and dividing it by the gate leakage current averaged over the entire curve from 96 K to 292 K at -4 V gate bias. The goal was to obtain percentages of less than 5 percent for every fit. However, owing to fluctuations in the data, a fit this close was not always achievable.

These numbers indicate the primary parameter affected by the electron radiation for the unpassivated HFETs was the trap density (N_t). Unpassivated HFETs with R-RMSE values less than 5 percent and receiving 5×10^{14} e-/cm² (at 0.5 MeV), showed an average 56 percent increase in N_t with less than a 1 percent increase in donor concentration, N_d . Percent changes for both the Schottky barrier energy (ϕ_{bo}) and the trap energy level (ϕ_t) were less than 10 percent. Figure 40 shows the TAT model fit to the pre-irradiation data ranging temperature (left) and gate bias voltage (right) for the first unpassivated HFET. The individual parameter fit values for these curves are presented in Table 12.

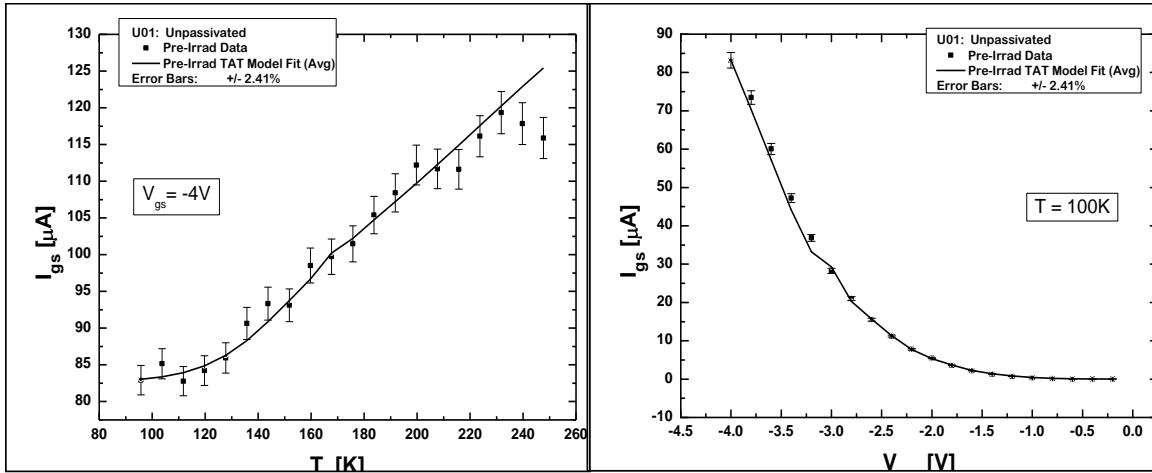


Figure 40. Pre-irradiation, TAT model fit to unpassivated HFET. Using the R-RMSE compared to averaged I_{gs} data resulted in $\pm 2.24\%$ error for fit.

Figure 41 shows the TAT model fit to the post-irradiation data ranging temperature (left) and gate bias voltage (right) for the first unpassivated HFET. The individual parameter fit values for these curves are presented in Table 12.

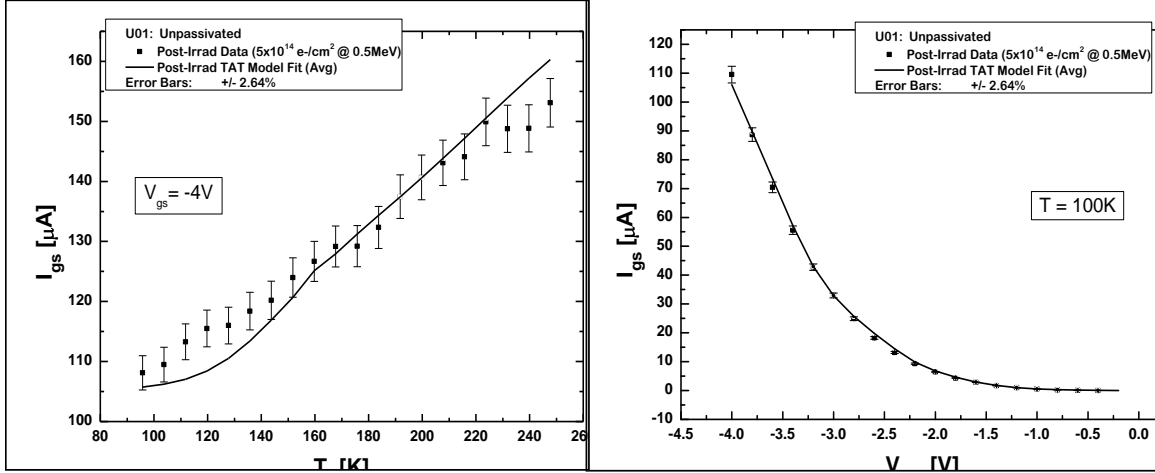


Figure 41. Post-irradiation TAT Model fit to unpassivated HFET. Using the R-RMSE compared to averaged I_{gs} data resulted in $\pm 2.24\%$ error for fit.

For the passivated HFETs, N_t decreased by more than 50 percent while N_d increased by up to 60 percent. Figure 42 and Figure 43 show the pre- and post-irradiation TAT fit curves for a passivated HFET. For the passivated devices ϕ_{bo} increased by 5 percent and ϕ_t decreased by 8.5 percent.

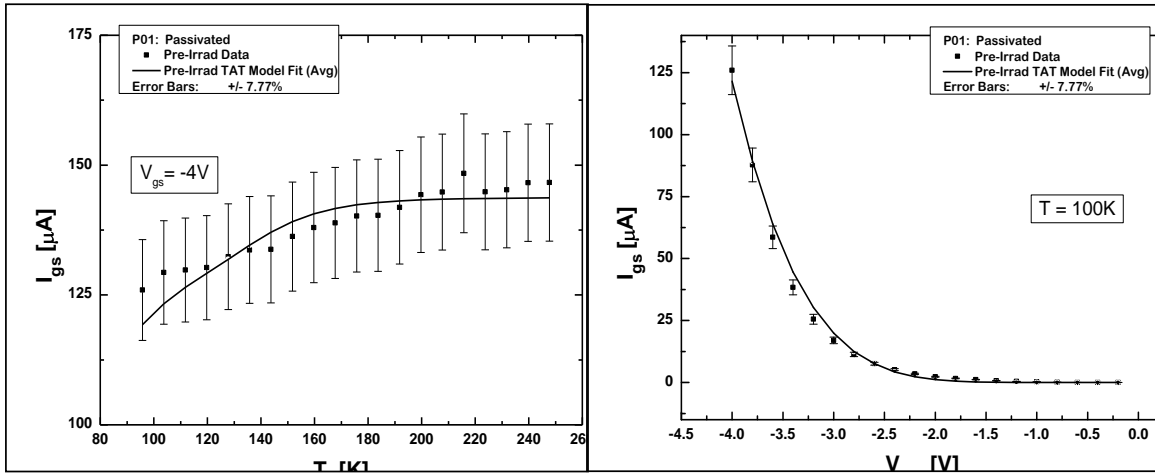


Figure 42. Pre-irradiation TAT model fit to passivated HFET. The typically higher gate leakage current levels for passivated devices is apparent, as well as the 7.77% R-RMSE to averaged current comparison. Error bars on left plot appear larger due to scale of the gate leakage current axis.

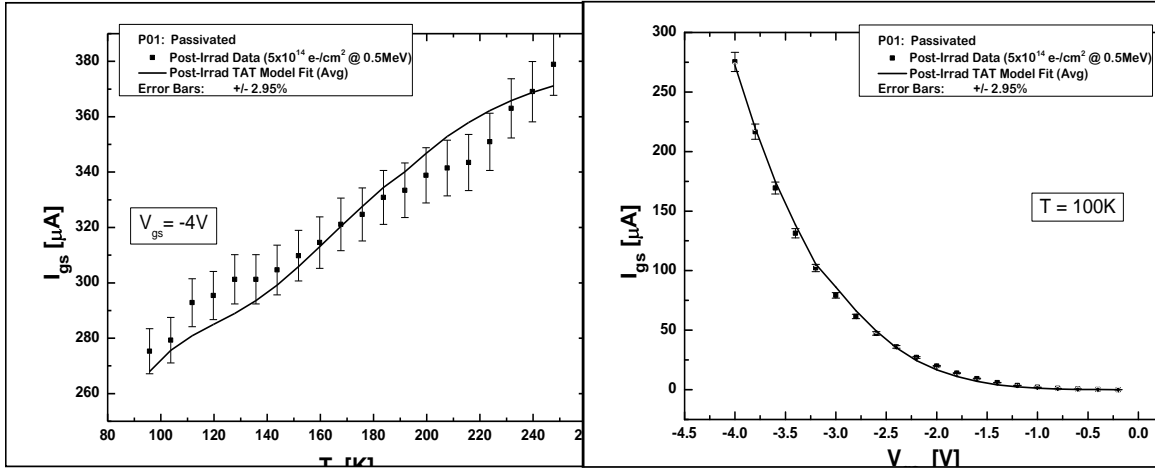


Figure 43. Post-irradiation TAT model fit to passivated HFET.

Figure 44 shows the pre- and post-irradiation I_{gs} vs. Temp curves for an unpassivated HFETs receiving a higher fluence of $1 \times 10^{15} \text{ e-/cm}^2$ (at 0.5 MeV). The best-fit values for the TAT model for these devices are presented in Table 12. The model fit indicates dominant contribution to the pre- to post-irradiation gate leakage current increase was from changes in N_t . This agrees with findings in [5] and [8] and the performance of the unpassivated devices in this study. These traps may be defects in the form of N vacancies created in the AlGaN layer by electron collisions with GaN molecules [48]. The electrons cause Frenkel pairs (vacancy and interstitial) that result in traps in the AlGaN layer thereby increasing the gate leakage current via Trap-Assisted Tunneling [48].

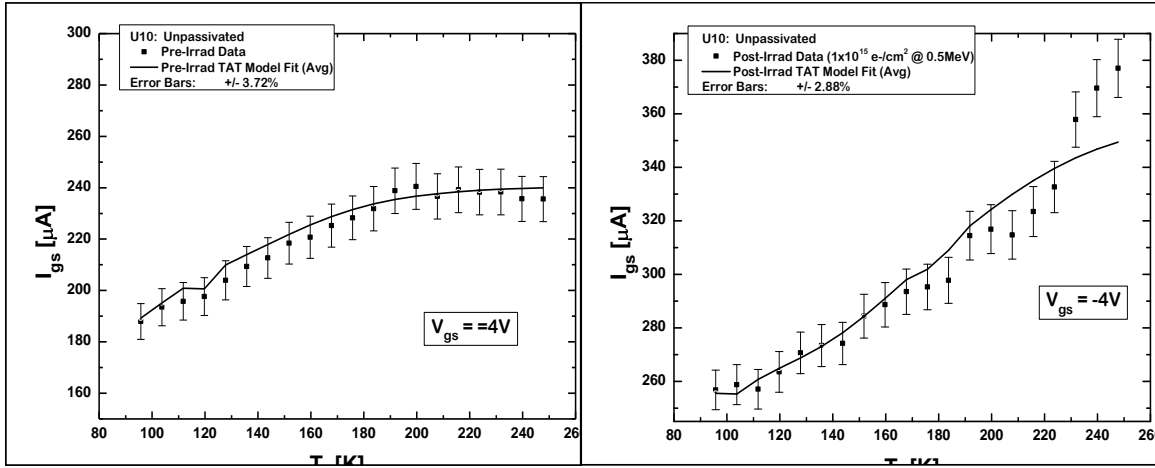


Figure 44. Pre- and post-irradiation (1×10^{15} e-/cm² @ 0.5 MeV) curves for U10. Note the relatively close fit of the TAT model as indicated by the low percent errors.

Table 13 highlights the experimental results for each pair of devices tested in each irradiation cycle. Note that for the third row of unpassivated devices, the LNT post-irradiation data is unavailable. This was a result of the liquid nitrogen supply tank emptying before the irradiation cycle ended. Despite this, the post-RT anneal checks for this cycle were still valid for comparison and analysis.

Table 13. Results from each HFET irradiation cycle. Values are percent change from original pre-irradiation values. In the third column, the ‘ I_{gs} vs. Temp @ V_{gs} ’ percent changes were determined from the $V_{gs} = -4$ V curves by comparing the gate current values at the $T = 200$ K for each curve.

Device / Fluence / Electron Energy	Measurement	Uncertainty LNT/RT (1 Sigma) [%]	Post-Irrad % Change (±) LNT / RT (if app.) Ref. to Pre-Irrad.	24day % Change (±) LNT / RT (if app.) Ref. to Pre-Irrad.	48day % Change (±) LNT / RT (if app.) Ref. to Pre-Irrad.
Unpassivated 5×10^{14} e/cm² $E_e = 0.5$ MeV	I_{ds} vs. V_{ds}	$\pm 2.2 / \pm 4.9$	+75 / +60	+10 / +14	-5 / +9
	I_{ds} vs. V_{gs} [V _{th}]	$\pm 2.2 / \pm 4.9$	-15 / -12	0 / -3	0 / -3
	C_{gs} vs. V_{gs} [V _{th} shift]	$\pm 0.3 / \pm 1.1$	-15 / 0	-2 / 0	-3 / 0
	I_{gs} vs. Temp @ V_{gs}	± 4.9	+38	+13	-8
Unpassivated 5×10^{14} e/cm² $E_e = 1.0$ MeV	I_{ds} vs. V_{ds}	$\pm 2.2 / \pm 4.9$	+53 / +13	-32 / -31	-49 / -15
	I_{ds} vs. V_{gs} [V _{th}]	$\pm 2.2 / \pm 4.9$	-13 / 0	+8 / 0	+8 / 0
	C_{gs} vs. V_{gs} [V _{th} shift]	$\pm 0.3 / \pm 1.1$	-11 / 0	+4 / 0	+28 / 0
	I_{gs} vs. Temp @ V_{gs}	± 4.9	+125	+104	+98
Unpassivated 5×10^{15} e/cm² $E_e = 0.5$ MeV	I_{ds} vs. V_{ds}	$\pm 2.2 / \pm 4.9$	NA / +1	-29 / -9	-6 / -16
	I_{ds} vs. V_{gs} [V _{th}]	$\pm 2.2 / \pm 4.9$	NA / -7	+3 / +5	0 / +4
	C_{gs} vs. V_{gs} [V _{th} shift]	$\pm 0.3 / \pm 1.1$	NA / 0	+8 / 0	0 / 0
	I_{gs} vs. Temp @ V_{gs}	± 4.9	+140	+77	+40
Unpassivated 1×10^{15} e/cm² $E_e = 0.5$ MeV	I_{ds} vs. V_{ds}	$\pm 2.2 / \pm 4.9$	+81 / +30	-24 / +29	-35 / +17
	I_{ds} vs. V_{gs} [V _{th}]	$\pm 2.2 / \pm 4.9$	-16 / -5	+3 / -5	+5 / -3
	C_{gs} vs. V_{gs} [V _{th} shift]	$\pm 0.3 / \pm 1.1$	-14 / -5	+5 / 0	+8 / 0
	I_{gs} vs. Temp @ V_{gs}	± 4.9	+32	+11	+5
Passivated 5×10^{14} e/cm² $E_e = 0.5$ MeV	I_{ds} vs. V_{ds}	$\pm 0.7 / \pm 0.4$	+26 / +23	+3 / +13	+1 / +15
	I_{ds} vs. V_{gs} [V _{th}]	$\pm 0.7 / \pm 0.4$	-4 / 0	0 / 0	+2 / 0
	C_{gs} vs. V_{gs} [V _{th} shift]	$\pm 1.1 / \pm 0.5$	0 / 0	0 / 0	0 / 0
	I_{gs} vs. Temp @ V_{gs}	± 0.7	+136	+136	+136
Passivated 2×10^{15} e/cm² $E_e = 1.0$ MeV	I_{ds} vs. V_{ds}	$\pm 0.7 / \pm 0.4$	+12 / -8	-3 / 0	-4 / 0
	I_{ds} vs. V_{gs} [V _{th}]	$\pm 0.7 / \pm 0.4$	-2 / +1	0 / 0	0 / 0
	C_{gs} vs. V_{gs} [V _{th} shift]	$\pm 1.1 / \pm 0.5$	0 / 0	0 / 0	0 / 0
	I_{gs} vs. Temp @ V_{gs}	± 0.7	+29	+15	+26

Comparison of Electron and Neutron Radiation Effects

The effects of electron radiation on the HFETs in this study were compared to the effects of 1 MeV (eq) reactor spectrum neutrons on identical HFETs in [5]. A correlating factor was not found, however, both similarities and differences in the effects of these radiations were observed. The electron fluences used in this study were on average two orders of magnitude (OOM) greater than the fluences of reactor spectrum neutrons used in [5]. Additionally, electron energies of 0.5 MeV and 1.0 MeV were used but only the 1.0 MeV results were compared to the neutron results. The difference in radiation-

induced effects between electrons and neutrons may be attributable to the differences in their masses and charges. Most notably, the negatively charged electrons result in more ionizing energy loss (IEL), whereas the neutrons without charge and a much greater mass are mostly subject to non-ionizing energy loss (NIEL) in which they create traps, defects, interstitials and ions in the material.

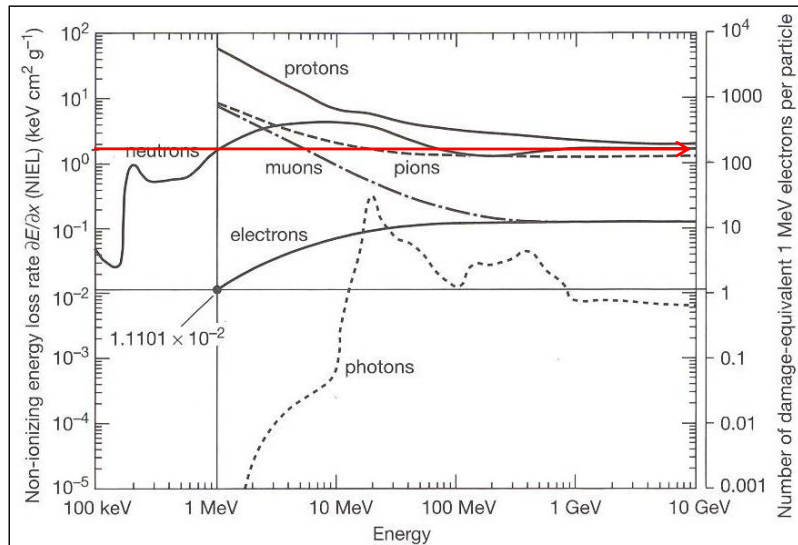


Figure 45. Chart from [12] showing non-ionizing energy loss (NIEL) [$\text{keV}\cdot\text{cm}^{-2}\cdot\text{g}^{-1}$] vs. energy in MeV for various types of radiation. Horizontal, right-pointing arrow (red) highlights equivalence of 1 MeV neutrons to 1 MeV electrons ($\sim 1:170$).

Figure 45 from [12] presents curves developed from calculations of NIEL damage in silicon for various radiations. Comparing NIEL for neutrons and electrons, this figure equates damage by a 1 MeV neutron in silicon to damage by 170x 1 MeV electrons. Comparing average neutron fluences from [5] of around $5 \times 10^{12} \text{ n/cm}^2$ to electron

$$\text{fluences in this study of around } 10^{15} \text{ e-}/\text{cm}^2 \text{ results in } 10^{15} \left[\frac{e^-}{\text{cm}^2} \right] \div 170 \cong 6 \times 10^{12} \left[\frac{n}{\text{cm}^2} \right].$$

This indicates the two OOM difference between neutron and electron fluences in these

studies result in similar magnitudes of NIEL effects in silicon. This comparison assumes similar relative behavior would occur in AlGaN.

The averaged post-irradiation increase in gate leakage current, for this study's unpassivated HFETs in Figure 39, indicate an increase of 18% compared to a 13% increase observed in [5]. The passivated devices in this study showed a 55% increase compared to less than half that at 22% in [5]. The similar increases in gate leakage currents for the unpassivated HFETs in both studies may be attributable to the NIEL interactions of the neutrons and electrons in the AlGaN layer; further indicating equivalent NIEL at the fluences studied.

Ionizing energy loss (IEL) for this study and [5] were compared using Figure 46 from [12]. Using the curves for neutrons and electrons at energies of 1 MeV and fluences of 5×10^{12} n/cm² and 10^{15} e-/cm² respectively provides equivalent IEL damage in silicon of 150 rad(Si) for the neutrons vs. 24.5 Mrad(Si) for the electrons. This indicates IEL occurs at a much higher rate for electron irradiation. Even considering an identical electron fluence of 5×10^{12} e-/cm² yields much higher silicon dose of 123 krad(Si), well above the calculated IEL for the neutrons in [5].

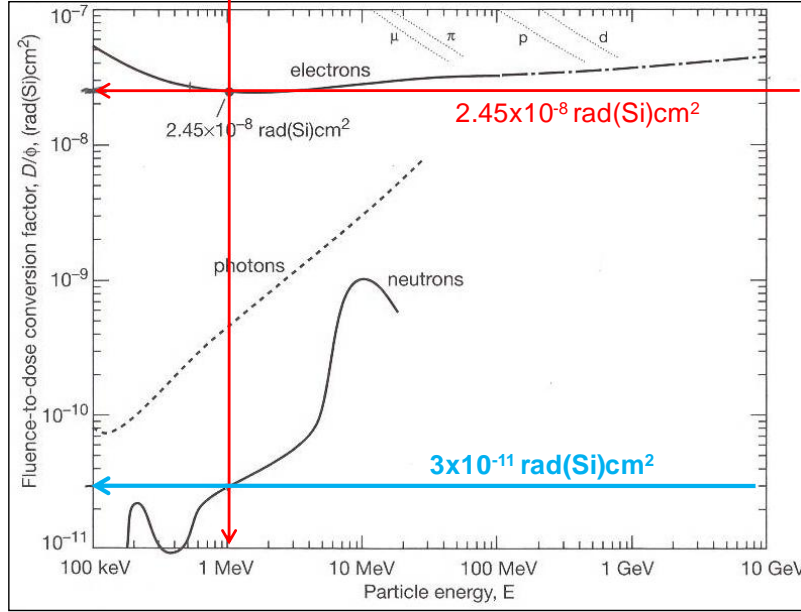


Figure 46: Ionizing energy loss and fluence-to-dose conversion factors in silicon for various radiations from [12].

In this study, transistor drain currents always showed a post-irradiation increase at LNT and RT. In [5] using neutrons, there was a post-irradiation increase at LNT, but it was followed by a decrease at RT. Other researchers using protons and ions as discussed in chapter 2 observed this post-irradiation decrease in I_{ds} at RT. Further, the percent increases at LNT were greater for both passivated and unpassivated devices exposed to the electron radiation than for those using neutrons.

The increased I_{ds} at RT for electron-irradiated HFETs is attributed to positive charge formed in the AlGaN via IEL that migrate to the AlGaN/GaN interface as their thermal energies increase with increasing temperature. Once at the interface, these positive charges may transform into traps, defects, or complexes that ionize at RT resulting in positive charges in the AlGaN along the interface that act to increase the carrier concentration in the 2DEG and therefore increases I_{ds} .

HFETs irradiated with neutrons showed increased I_{ds} at LNT that may be attributed to electron-hole pair formation owing to the movements of neutron-created ions through the material. These e-hole pairs result in positive charge in the AlGaN layer and increased I_{ds} in the same manner as for electron-irradiated HFETs. As temperature approaches RT, these positive charges migrate under influence of the AlGaN's piezoelectric field and increase the interface trap concentration as seen in Figure 35 and Table 11. The neutron irradiation also results in significant numbers of defects, traps, or complexes (NIEL) in and near the 2DEG region. These NIEL mechanisms appear to reduce carrier mobility in the 2DEG, as temperatures approach RT, via Coulombic scattering and trapping of carriers. In addition, at RT the number of radiation induced positive charges remaining in the AlGaN have likely decreased thereby decreasing the charge available in the AlGaN to enhance carrier concentration in the 2DEG and I_{ds} .

The I_{gs} vs. T measurements presented in Table 13 show significant recovery in the unpassivated devices irradiated with 0.5 MeV electrons compared with unpassivated devices exposed to 1.0 MeV electrons in this study or neutrons in [5]. This may be attributable to the type or location of defects created in the AlGaN. The higher energy electrons and the larger charge-less neutrons may create a higher percentage of non-annealing or non-migrating traps and defects, thereby resulting in long-term, slow-annealing, radiation-induced increases in gate current. Additionally, passivated devices irradiated with electrons showed little or no recovery after RT annealing, similar to passivated devices exposed to neutrons which showed little recovery post-RT anneal.

Results from the TAT model fitting to the I_{gs} vs. T curves for neutron-irradiated HFETs in [5] and electron-irradiated HFETs in this study indicate a higher average

percent increase in N_t (trap density) in the neutron-irradiated HFETs. This conflicts with the observed higher percent increase in the averaged gate leakage currents for the electron-irradiated HFETs in this study than for the neutron-irradiated HFETs in [5].

VI. Conclusions and Recommendations

Conclusions

All HFETs irradiated in this study, survived fluence levels ranging from 5×10^{14} to 5×10^{15} [e-/cm²] at electron energies of 0.5 MeV or 1.0 MeV. Each device was subjected to full pre- and post-irradiation measurement regimens, detailed in chapter 4, and to at least three (in some cases five) post-RT anneal measurements. Experimental results indicate the electron radiation produced effects in the AlGaN and GaN layers in the HFETs that affected the electrical properties of the devices. Some effects demonstrated temperature dependence; i.e. occurring only at LNT or to a lesser extent at RT, while other observed effects showed little variation LNT to RT.

The primary means for evaluating the performance of the HFETs studied were changes to their drain (I_{ds}) and their gate leakage (I_{gs}) currents, shifts in device threshold voltages (V_{th}), and temperature dependence (or the lack) for these parameters.

The following summarizes the effects of electron radiation and temperature on AlGaN/GaN HFET electrical properties observed in this study:

- Changes to Drain-to-Source Currents
 - Pre-irradiation drain current (I_{ds}) levels were averaged 75 % higher for passivated HFETs than for unpassivated devices.
 - Drain currents increased post-irradiation at LNT and to a lesser extent at RT for all HFETs with on average smaller percent increases for passivated devices.

- Post-irradiation increases in I_{ds} showed annealing for all HFETs following RT anneal periods of varying lengths (most recovery was noted within 24 to 48 days).
- Changes to Threshold Voltages
 - Carrier concentration (n_s) changes evaluated using the charge control model [46] and observed threshold voltage shifts matched n_s changes calculated using pre- and post-irradiation I_{ds} values to less than 19% difference.
 - Negative shifts in device threshold voltages typically -0.4 to -0.6 V for unpassivated and -0.2 to -0.4 V for passivated HFETs were observed with quick succession measurements taken at LNT and RT and negligible temperature dependence.
 - Threshold voltage shifts annealed to nearly pre-irradiation values after 12 - 48 day RT anneal periods.
- Changes to Capacitance Curves
 - Negative, full-curve shifts in entire gate capacitance (C_{gs}) vs. gate bias (V_{gs}) curves post-irradiation showed almost total recovery after RT anneal.
 - Slope flattening in RT C_{gs} vs. V_{gs} curves, indicating the presence of interface traps, increased post-irradiation in all HFETs studied.
- Changes to Gate Leakage Currents
 - Post-irradiation increases in gate leakage currents (I_{gs}) occurred in all devices with almost total recovery observed in the unpassivated devices.

- Post-irradiation increases in I_{gs} for passivated HFETs showed little tendency toward recovery after 48-day or longer RT anneal periods.
- TAT Model[36][8] fit to unpassivated HFET data indicated increased N_t to be dominant parameter affecting gate leakage currents, while model fit to passivated HFET data indicated increased N_d to be the dominant parameter.
- Comparison of Electron to Neutron Irradiation Effects
 - Comparison of electrons in this study to neutrons in [5] indicate similar NIEL for the lower 1 MeV neutron fluences vs. two OOM higher 1 MeV electron fluences.
 - Comparison of electrons and neutrons further indicated much greater IEL effects for electrons than neutrons, even when comparing same fluence levels.
 - TAT model results (changes in N_t) conflict with averaged percent changes in gate leakage currents for electrons vs. neutrons; higher % change in N_t with neutrons, but higher average percent increase in gate leakage currents with electrons.

The mechanisms by which I_{ds} and I_{gs} are affected vary. Drain current seems primarily affected by changes to the 2DEG; i.e. changes to the channel dimensions relating to effective bias acting in the channel region of the GaN, or to mobility of carriers within the channel through coulombic scattering. The increases in I_{ds} noted post-irradiation at LNT and RT appear to result from trapped positive charges in the AlGaN layer, owing to ionizations (electron-hole pair creation) by the incident electrons. Increases in I_{gs} , while affected by the trapped charges, mentioned above, appear primarily

enhanced by radiation-induced deep and shallow traps in the band-gap near the conduction band, in the AlGaN, but below the barrier height, that provide the traps for the trap-assisted tunneling in [35] and [36].

Mechanisms within the AlGaN and GaN contributing to the concentration of defects, traps, and charges include; electron-hole pairs, displacements of Al, N, and Ga atoms, and for passivated devices the unknown by-products of electrons breaking the Si and N bonds in the Si_3N_4 passivation layer. Additionally, hole mobility is greatly affected by temperature. Higher temperatures result in higher hole mobility, thereby allowing the holes to migrate or recombine, ultimately reducing their impact on device operation at higher temperatures.

The Si_3N_4 passivation layer appeared to enhance post-irradiation performance in the passivated devices owing to overall lower percent changes in their post-irradiation drain currents and threshold voltage shifts. However, passivated devices showed significantly higher percent increases in post-irradiation gate leakage currents with almost no tendency to recover after RT anneal periods, unlike unpassivated HFETs.

The AlGaN/GaN HFETs studied showed good radiation hardness in that they maintained their transistor-like operation after all fluences used. In most cases, the effects appeared to be temporary, annealing out at RT in some cases while in others annealing out after 12 to 48 day RT periods. In the opinion of the author, further research to expand the knowledge bounds on these devices is definitely warranted.

Recommended Future Efforts in AlGaN/GaN Research

A useful study would be to maintain study samples of these devices at LNT from post-irradiation to some length of LNT anneal period; i.e. 48, 60, 180 days. One hindrance to the current study was the inability to maintain sample HFETs at LNT for lengthy post-irradiation periods. This would allow researchers to see if observed effects would eventually anneal at LNT, or if they became permanent defects at or after prolonged LNT periods. Further, taking frequent measurements at LNT and then incrementally allowing a representative sample of the test population to reach RT at predetermined intervals, could provide minimum or maximum times at LNT at which the defects becomes permanent or it may show that annealing will occur even after extended periods at LNT.

Continued work on a correlating factor to relate electron radiation damage to neutron radiation damage in this material or these types of devices could be undertaken. The importance of a means to rapidly convert observed effects, induced by a particular type of radiation, to a predicted response to other types of radiation, could reduce testing time and costs in future space systems development.

An in-depth computer model comparison of the data obtained during this research, to accepted material and device physics processes, could enable development of better radiation effects simulation software. This effort could be tailored to a specific type of AlGaN/GaN device or to AlGaN and GaN materials individually.

Another worthy study would be to obtain the exact AFRL SNDD architectural drawings and specifications, to which these HFET reticles were produced, and using that

information to compare performance and radiation hardness of the various FET designs on the reticles. This would allow dimensional comparisons as well as radiation type/fluence/energy comparisons. Further, this might allow for more efficient utilization of the, till now, unused FETs on each reticle.

Additionally, a study designed to study the time dependence of interface trap build-up in these HFETs after varying types, energies, and fluences of radiation would be useful. This study could provide data to determine the rate at which these traps manifest post-irradiation and if and at what rate they decrease after varying lengths of time post-irradiation. Difficulties would lie in being able to take the capacitance measurements immediately after cessation of electron irradiation owing to VDG safety concerns. These concerns may be mitigated with remote monitoring and modified measurement control software.

Finally, *in situ* measurements taken while varying gate bias with the devices subjected to gamma and neutron fluxes would provide data on transient effects not necessarily observable in measurements taken post-irradiation. In addition, a comparison of the effects due to these two very different types of radiation could be done. This research could be conducted at the Ohio State Research Reactor facility with their Co-60 facility and reactor. Equipment, HFETs, and other unique equipment is already on-hand for this type of study.

Bibliography

- [1] U. Mishra, P. Parikh, and Y.-F. Wu, "AlGaN/GaN HEMTs – An Overview of Device Operation and Applications," *Proceedings of the IEEE*, vol. 90, no. 6, pp. 1022-1031, June 2002.
- [2] Hadis Morkoc, et al. "Review: GaN-based modulation doped FETs and UV Detectors," *Solid-State Electronics*, 46: 157-202 (2002).
- [3] O. Ambacher, et al., "Two-dimensional electron gases induced by spontaneous and piezoelectric polarization charges in N- and Ga-face AlGaN/GaN heterostructures," *Journal of Applied Physics*, vol. 85, no. 6, pp. 3222-3333, 1999.
- [4] J. M. Sattler, *An Analysis of the Effects of Low Energy Electron Radiation on AlGaN/GaN Modulation-Doped Field-Effect Transistors*, Air Force Institute of Technology (AU), Wright-Patterson AFB OH, March 2004.
- [5] J. W. McClory, *The Effect of Radiation on the Electrical Properties of Aluminum Gallium Nitride/Gallium Nitride Heterostructures*, Air Force Institute of Technology (AU), WPAFB, OH, June 2008.
- [6] J. W. McClory, et al., "Temperature Dependent Electrical Characteristics of Neutron Irradiated AlGaN/GaN HFETs," *IEEE Transactions on Nuclear Science*, vol. 54, no. 6, pp. 1969-1974, Dec. 2007.
- [7] J. W. McClory, et al., "An Analysis of the Effects of Low-Energy Electron Irradiation of AlGaN/GaN HFETs," *IEEE Transactions on Nuclear Science*, vol. 54, no. 6, pp. 1946-1952, Dec. 2007.
- [8] J. C. Petrosky, J.W. McClory, et al., "Trap Assisted tunneling Induced Currents in Neutron Irradiated AlGaN/GaN HFETs," *IEEE Transactions on Nuclear Science*, IEEE TNS-00479-2008.R1, Copy for Review, Submitted July 2008.
- [9] R. Gaska, J. W. Yang, A. Osinsky, Q. Chen, M. A. Khan, A. O. Orlov, G. L. Snider, M. S. Shur, "Electron transport in AlGaN-GaN heterostructures grown on 6H-SiC substrates", *Applied Physics Letters*, vol. 72, no. 6, pp. 707-709, 1998.
- [10] T. E. Gray, *Investigation of Gate Current in Neutron Irradiated AlGaN/GaN Heterostructure Field Effect Transistors Using Voltage and Temperature Dependence*, Air Force Institute of Technology (AU), WPAFB, OH, March 2007.

- [11] M.R. Hogsed, et al., “Radiation-induced Electron Traps in Al0.14Ga0.86N by 1 MeV Electron Radiation,” *Applied Physics Letters*, vol. 86, 261906, 2005.
- [12] L. Adams, A. Holmes-Siedle, *Handbook of Radiation Effects*, 2nd Edition, Oxford University Press, Oxford, 2002.
- [13] T. A. Jarzen, *Capacitance-Voltage Study on the Effects of Low Energy Electron Radiation on Al_{0.24}Ga_{0.76}N/GaN High Electron Mobility Transistors*, Air Force Institute of Technology (AU), Wright-Patterson AFB OH, March 2005.
- [14] B. D. White, et al., “Characterization of 1.8 MeV proton irradiated AlGaN/GaN field-effect transistor structures by nanoscale depth-resolved luminescence spectroscopy,” *IEEE Transactions on Nuclear Science*, vol. 49, no. 6, pp. 2695-2701, Dec. 2002.
- [15] B. Luo, et al., “High-energy proton irradiation effects on AlGaN/GaN high-electron mobility transistors”, *Journal of Electronic Materials*, vol. 31, no. 5, pp. 437-441, 2002.
- [16] X. Hu, et al., “Proton-irradiation effects on AlGaN/AlN/GaN high electron mobility transistors,” *IEEE Transactions on Nuclear Science*, vol. 50, no. 6, pp. 1791-1796, Dec. 2003.
- [17] B. D. White, et al., “Electrical, spectral, and chemical properties of 1.8 MeV proton irradiated AlGaN/GaN HEMT structures as a function of proton fluence,” *IEEE Transactions on Nuclear Science*, vol. 50, no. 6, pp. 1934-1941, Dec. 2003.
- [18] P. Karmarkar, et al., “Proton irradiation effects on GaN-Based high electron-mobility transistors with Si-doped Al_xGa_{1-x}N and thick GaN cap layers,” *IEEE Transactions on Nuclear Science*, vol. 51, no. 6, pp. 3801-3806, Dec. 2004.
- [19] X. Hu, et al., “The energy dependence of proton-induced degradation in AlGaN/GaN high electron mobility transistors,” *IEEE Transactions on Nuclear Science*, vol. 51, no. 2, pp. 293-297, Apr. 2004.
- [20] O. Aktas, et al., “60Co gamma radiation effects on DC, RF, and pulsed I-V characteristics of AlGaN/GaN HEMTs,” *Solid State Electronics*, vol. 48, pp. 471-475, 2004.
- [21] G. Sonia, et al., “Proton and Heavy Ion Irradiation Effects on AlGaN/GaN HFET Devices,” *IEEE Transactions on Nuclear Science*, vol. 53, no. 6, pp. 3661-3666, Dec. 2006.
- [22] NI Labview Professional Development System, Version 8.2, National Instruments Inc., 2006.

- [23] NI Measurement and Automation Explorer, Version 4.1.0.3001, National Instruments Inc., 2006.
- [24] Microsoft Visual Basic 6.0 SP5, Version 8988, Microsoft Corporation, 2000.
- [25] H. Markoc. "Potential applications on III-V nitride semiconductors," *Materials Science and Engineering*, B43: 137-146 (1997).
- [26] M. Henini. "III-V nitrides for electronic and UV applications," *III-Vs Review*, Vol. 12, No. 5: 28-32 (1999).
- [27] M. Stutzmann, et al. "GaN-based heterostructures for sensor applications," *Diamond and Related Materials*, 11: 886-891 (2002).
- [28] G. Sonia, et al. "2 MeV ion irradiation effects on AlGaN/GaN HFET devices," *Solid-State Electronics*, vol. 52, pp. 1011-1017, Apr. 2008.
- [29] D. Donoval, et al., "High-temperature performance of AlGaN/GaN HFETs and MOSHFETs", *Microelectronics Reliability*, (2008), doi:10.1016/j.microrel.2008.04.017.
- [30] S. A. Vitusevich, et al., Improvement of interface properties of AlGaN/GaN heterostructures under gamma-radiation, *Applied Surface Science*, (2008), doi:10.1016/j.apsusc.2008.07.029.
- [31] J.C. Petrosky. Air Force Institute of Technology (AU), Wright-Patterson AFB OH. Face to Face Conversation. 25 August 2008.
- [32] K. D. Greene, *Electron Paramagnetic Resonance Spectroscopy and Hall Effect Studies of the Effects of Low Energy Electron Irradiation on Gallium Nitride (GaN)*. Air Force Institute of Technology (AU), Wright-Patterson AFB OH, September 2003.
- [33] D.C. Look, et al., "Defect Donor and Acceptor in GaN," *Physical Review Letters*, vol. 79, no. 12, pp. 2273-2276, 1997.
- [34] MIL-STD-1809, USAF, 15 February 1991.
- [35] S. Karmalkar, D.M. Sathaiya, "Mechanism of the reverse gate leakage in AlGaN/GaN high electron mobility transistors," *Applied Physics Letters*, vol. 82, no. 22, pp. 3976-78, 2 June 2003.

- [36] D. M. Sathaiya, et al. "Thermionic trap-assisted tunneling model and its application to leakage current in nitrided oxides and AlGaN/GaN high electron mobility transistors," *Journal of Applied Physics*, 11 May 2006.
- [37] D.M. Sathaiya, S. Karmalkar, "Edge Effects on Gate Tunneling Current in HEMTs," *IEEE Transactions on Nuclear Science*, Vol. 54. No. 10, Oct. 2007.
- [38] A.L. Barry, et al., "Energy Dependence of Electron Damage and Displacement Threshold Energy in 6H Silicon Carbide," *IEEE Transactions on Nuclear Science*, Vol. 38. No. 6, Dec. 1991.
- [39] R. L. Chaplin, et al., "Energy Dependence of the Stage-I Recovery of Aluminum," *Physical Review*, Vol. 163, No. 3, 15 Nov. 1967.
- [40] D. K. Schroder, *Semiconductor Material and Device Characterization*, 2nd Edition, John Wiley and Sons, New York, 1998.
- [41] T. A. Uhlman, *Temperature Dependent Current-Voltage Measurements of Neutron Irradiated AlGaN/GaN Modulation Doped Field Effect Transistors*. Air Force Institute of Technology (AU), Wright-Patterson AFB OH, March 2005.
- [42] J. F. Kucko, *Insulator Charging in RF MEMS Capacitive Switches*, Air Force Institute of Technology (AU), Wright-Patterson AFB, OH, June 2005 (ADA441556).
- [43] Y. Takahashi, K. Ohnishi, Fujimaki, and M. Yoshikawa. "Radiation-Induced Trapped Charge in Metal-Nitride-Oxide-Semiconductor Structure", *IEEE Transactions on Nuclear Science*, 46: 1578-1585 (December 1999).
- [44] A. Rashmi, A. Agrawal, et al., "Analytical model for DC characteristics and small signal parameters of AlGaN/GaN modulation doped field effect transistors for microwave circuit applications," *Microwave and Optical Technology Letters*, 27: 413-418, 2000.
- [45] A. Rashmi, S. Haldar, et al., "2-D analytical model for current voltage characteristics and output conductance of AlGaN/GaN MODFET," *Microwave and Optical Technology Letters*, 29: 117-123, 2001.
- [46] A. Rashmi, Kranti, et al., "An accurate charge control model for spontaneous and piezoelectric polarization dependent two-dimensional electron gas (2-DEG) sheet charge density of lattice mismatched AlGaN/GaN HEMTs," *Solid-State Electronics*, 46(5): 621-630, 2002.
- [47] C. Svensson, I. Lundstrom, "Trap-assisted charge injection in NMOS structures," *Journal of Applied Physics*, 44(10): 4657-4662, 1973.

- [48] D.C. Look, et al., “On the Nitrogen Vacancy in GaN,” *Applied Physics Letters*, Vol. 83, No. 17, pp. 3525-3527, 2003.
- [49] P. Pisechny, et al., “Determination of Interface Trap Density in Unipolar Structures Using Quasistatic C-V Method,” *Journal of Electrical Engineering*, Vol. 55, No. 3-4: 95-99 (2004).
- [50] T.P. Ma, P.V. Dressendorfer, *Ionizing Radiation Effects in MOS Devices and Circuits*, John Wiley and Sons, 1989.
- [51] B. Van Zeghbroeck, *Principles of Semiconductor Devices*, available at <http://ece-www.colorado.edu/~bart/book/>, University of Colorado, 2007.
- [52] International Commission on Radiation Units and Measurements, *Stopping Power for Electrons and Positrons*, ICRU Report 37, Bethesda, MD. 1984.
- [53] S.M. Sze, *Semiconductor Devices*, 1st Edition, John Wiley and Sons, New York, 1985.
- [54] J.D. Albrecht, R.P. Wang, P.P. Ruden, M. Farahmand, K.F. Brennan, Electron Transport Characteristics of GaN for High Temperature Device Modeling, *Journal of Applied Physics*, 83(9), 4777-4781, 1998.
- [55] U.V. Bhapkar, M.S. Shur, Monte Carlo Calculation of Velocity-field Characteristics of Wurtzite GaN, *Journal of Applied Physics*, 82(4), 1649-1655, 1997.
- [56] R. Gaska, J.W. Yang, et al., Electron Transport in AlGaN/GaN Heterostructures Grown on 6H-SiC Substrates, *Applied Physics Letters*, Vol. 72, No. 6, 09Feb98.
- [57] O’day, B.E., collegial discussion of comparative mathematical methods with the author, 24 Feb 09.

REPORT DOCUMENTATION PAGE				Form Approved OMB No. 074-0188	
<p>The public reporting burden for this collection of information is estimated to average 1 hour per response, including the time for reviewing instructions, searching existing data sources, gathering and maintaining the data needed, and completing and reviewing the collection of information. Send comments regarding this burden estimate or any other aspect of the collection of information, including suggestions for reducing this burden to Department of Defense, Washington Headquarters Services, Directorate for Information Operations and Reports (0704-0188), 1215 Jefferson Davis Highway, Suite 1204, Arlington, VA 22202-4302. Respondents should be aware that notwithstanding any other provision of law, no person shall be subject to an penalty for failing to comply with a collection of information if it does not display a currently valid OMB control number.</p> <p>PLEASE DO NOT RETURN YOUR FORM TO THE ABOVE ADDRESS.</p>					
1. REPORT DATE (DD-MM-YYYY)	2. REPORT TYPE				3. DATES COVERED (From – To)
27-03-2009	Masters Thesis				Sep 2007 - Mar 2009
TITLE AND SUBTITLE The Effects of Temperature and Electron Radiation on the Electrical Properties of AlGaN/GaN Heterostructure Field Effect Transistors				5a. CONTRACT NUMBER	
				5b. GRANT NUMBER	
				5c. PROGRAM ELEMENT NUMBER	
AUTHOR(S) Moran, Jeffrey T., Major, USA				5d. PROJECT NUMBER	
				5e. TASK NUMBER	
				5f. WORK UNIT NUMBER	
7. PERFORMING ORGANIZATION NAMES(S) AND ADDRESS(S) Air Force Institute of Technology Graduate School of Engineering and Management (AFIT/EN) 2950 Hobson Way WPAFB OH 45433-7765				8. PERFORMING ORGANIZATION REPORT NUMBER AFIT/GNE/ENP/09-M04	
9. SPONSORING/MONITORING AGENCY NAME(S) AND ADDRESS(ES) DTRA/CSU COL Mark Mattox 1900 Wyoming Blvd SE Kirtland AFB, NM 87117-5669				10. SPONSOR/MONITOR'S ACRONYM(S) 11. SPONSOR/MONITOR'S REPORT NUMBER(S)	
12. DISTRIBUTION/AVAILABILITY STATEMENT APPROVED FOR PUBLIC RELEASE; DISTRIBUTION UNLIMITED					
13. SUPPLEMENTARY NOTES					
4. ABSTRACT AlGaN/GaN Heterostructure Field Effect Transistors (HFETs) have come under increased study, in recent years, owing to their highly desirable material and electrical properties, ruggedness, and survivability even during and after exposure to extreme temperature and radiation environments. These devices or similar devices constructed of AlGaN and/or GaN materials are being researched for their potential applications in many military and space based systems. In this study, unpassivated and SiN passivated $\text{Al}_{0.27}\text{Ga}_{0.73}\text{N}/\text{GaN}$ HFETs were subjected to electron radiation at incident energies of 0.5MeV and 1.0MeV and fluences from 5×10^{14} to 5×10^{15} [e-/cm ²] while maintained in a 10^{-6} Torr or higher vacuum at liquid nitrogen temperature (LN). The primary focus of the research was the effects of electron radiation and temperature on drain current, threshold voltage shift, and gate-channel capacitance. Measurements were taken of transistor current, gate-channel capacitance, and gate leakage current vs. gate bias at 4K temperature intervals beginning at LN through room temperature (RT). The resulting gate leakage currents were fitted to a Trap-Assisted Tunneling model and transistor currents were compared to a Charge Control model to evaluate post-irradiation change mechanisms to the parameters of these models. Post-irradiation drain currents increased for all devices, with a consistently lesser increase observed for passivated devices. Most post-irradiation increases returned to nearly pre-irradiation levels after an RT anneal period. Threshold voltage shifts averaged -0.5V for unpassivated and -0.2V for passivated HFETs, showed negligible temperature dependence, and returned to near pre-irradiation values, after RT anneal periods. Gate leakage currents showed post-irradiation increases for all devices. Fitting experimental data to the trap-assisted tunneling model indicated the dominant mechanism supporting the post-irradiation increase in gate leakage current was increased trap density for unpassivated devices and donor concentration for passivated devices. Post-irradiation changes in carrier concentration, obtained from observed drain current increases and calculated with the charge control model using observed threshold voltage shifts, were attributed to trapped, positive charges in the AlGaN layer. This trapped positive charge resulted from electron-hole pairs created by electron radiation-induced ionizations.					
15. SUBJECT TERMS AlGaN, Aluminum Gallium Nitride, HFET, 2DEG, Trap-Assisted Tunneling, TAT, Heterostructure Field Effect Transistors					
16. SECURITY CLASSIFICATION OF: UNCLASSIFIED		17. LIMITATION OF ABSTRACT UU	18. NUMBER OF PAGES 120	19a. NAME OF RESPONSIBLE PERSON John W. McClory (ENP)	
REPORT	ABSTRACT			C. THIS PAGE	19b. TELEPHONE NUMBER (Include area code)
U	U	U		937-255-3636 x7308	John.McClory@afit.edu

Standard Form 298 (Rev: 8-98)

Prescribed by ANSI Std. Z39-18